ABSTRACT

DYNAMICS OF 1D GRANULAR COLUMN

by

Luo Zuo

This dissertation is focused on a discrete element study of the dynamics of a one-dimensional column of inelastic spheres that it subjected to taps by prescribing a half sine wave pulse to supporting floor. Contact interactions obey the Walton-Braun soft-sphere model in which the loading (unloading) path is governing by linear springs of stiffness K_1, thereby producing collisional energy loss through a constant restitution coefficient e. Over a 'short time scale', computations are done to examine the floor pulse wave as it propagates through the column contact network. Comparisons of the simulated findings are made with experimental measurements in the literature where possible. Principal emphasis is placed on computing various measures of the evolution of the system that occurs over a long time scale, i.e., the time interval over which the system undergoes a dilation and contraction to a quiescent state after the application of the tap. Here the goal is to chart the column behavior as a function of the amplitude and frequency of the tap, as well as the number of particles in the system and energy dissipation as characterized by. While at the outset, it may appear that this is a simple system, the dynamics in fact are enormously complex as computed Poincaré maps of the mass center trajectories reveal periodic, period doubling and chaotic regimes.

DYNAMICS OF 1D GRANULAR COLUMN

by
Luo Zuo

A Dissertation
Submitted to the Faculty of
New Jersey Institute of Technology
in Partial Fulfillment of the Requirements for the Degree of
Doctor of Philosophy in Mechanical Engineering

Department of Mechanical and Industrial Engineering

May 2014

.

APPROVAL PAGE

DYNAMICS OF 1D GRANULAR COLUMN

Luo Zuo

Dr. Anthony D Rosato, Dissertation Advisor Professor of Mechanical and Industrial Engineering, NJIT	Date
Dr. Pushpendra Singh, Committee Member Professor of Mechanical and Industrial Engineering, NJIT	Date
Dr. I J Rao, Committee Member Professor of Mechanical and Industrial Engineering, NJIT	Date
Dr. Ian S Fischer, Committee Member Professor of Mechanical and Industrial Engineering, NJIT	Date
Dr. David J Horntrop, Committee Member Associate Professor of Mathematics, NJIT	Date
Dr. Denis L Blackmore, Committee Member Professor of Mathematics, NJIT	Date

BIOGRAPHICAL SKETCH

Author: **Luo Zuo**

Degree: Doctor of Philosophy

Date: January 2014

Undergraduate and Graduate Education:

- Doctor of Philosophy in Mechanical Engineering,
  New Jersey Institute of Technology, Newark, NJ, 2014
- Master of Science in Mechanical Engineering,
  New Jersey Institute of Technology, Newark, NJ, 2009
- Bachelor of Science in Electrical Engineering,
  Southeast University, Nanjing, P. R. China, 2008

Major: Mechanical Engineering

Presentations and Publications:

A. D. Rosato, D. Blackmore, X. M. Tricoche, K. Urban and L. Zuo, "Dynamical Systems Model and Discrete Element Simulations of a Tapped Granular Column." AIP Conf. Proc. 1542, 317 (2013).

A. D. Rosato, Luo Zuo, and D. Blackmore. "Cooling of a Tapped Granular Column." Bulletin of the American Physical Society 58 (2013).

V. Ratnaswamy, A.D. Rosato, D. Blackmore, X. Tricoche, N. Ching, L. Zuo "Evolution of Solids Fraction Surfaces in Tapping: Simulation and Dynamical Systems Analysis." Granular Matter 14.2 (2012): 163-168.

D. Blackmore, A.D. Rosato, X. Tricoche, K. Urban, and L. Zuo, "Analysis, Simulation and Visualization of 1D Tapping Via Reduced Dynamical Systems Models." Physica D, (2013), under revision.

This dissertation is dedicated to
my beloved parents and girlfriend

ACKNOWLEDGMENT

I would like to express sincere gratitude to my advisor, Dr Anthony D. Rosato, for his guidance, friendship and moral support through the research.

Special thanks to Drs. Pushpendra Singh, I. J. Rao, Ian S. Fischer, David J. Horntrop, Denis L. Blackmore for serving as member of the committee.

My final acknowledgement would like to go to my parents and girlfriend. Their support always encourages me to move forward.

TABLE OF CONTENTS

TABLE OF CONTENTS
(Continued)

Chapter **Page**

TABLE OF CONTENTS
(Continued)

Chapter **Page**

LIST OF TABLES

LIST OF FIGURES

CHAPTER 1

INTRODUCTION

1.1 Overview

Granular materials exist all over our world. Soil, sand and snow, fracture of stones may be viewed as complex granular systems. In industry, tons of raw materials are handled and processed daily to produce goods in everyday use. Industrial processes developed to work with bulk solids generally require various systems that are used to transport and manipulate the material (for example [1-3]). The design of these systems requires some knowledge of how the materials behavior under various loading scenarios[4]. And one of the most important of these is vibration (e.g., [5-11]), which is often used to induce motion and enhance mobility.

Over the course of the last 60 years since the pioneering work of R. Bagnold[12, 13], research efforts to understand the behavior of granular systems have been intensifying as evidenced by collaborative efforts between various communities (i.e., mathematics, engineering and physics). And while substantial process has been made, a model capable of describing the behavior of granular systems over the full gamut of observed phenomena remains tenuous. Indeed, in comparison to the well-understood behavior of fluids, gases and solids, for which there are predictive models, the science of granular materials is really still in its infancy[4].

Early laboratory experiments carried out on granular materials generally focused on measuring flow properties that were easily observed as acquiring data within the material was extremely difficult. The development of very sophisticated, non-invasive

methods (e.g., magnetic resonance imaging[14-18], X-ray tomography[19-21], positron-emission tracking[22, 23]) has opened up the field so that it is now feasible to collect data on physical processes within the material – albeit at high cost. What's more, experiments of this nature have enhanced our understanding of the behavior of granular solids within restricted flow regimes. And while it is expected that continued advances in non-invasive technologies will enlarge the archive of experimentally-gathered data to realistic (industrial) flows, broader discoveries and insights can be achieved via an approach that couples experimental findings and particle-level computer simulations under an umbrella of emerging theoretical models. It is within this philosophical framework that the investigation reported in this dissertation was done.

Perhaps one of the most interesting loading scenarios for a granular system are vibrations or discrete taps[24, 25], as, by carefully controlling the input, it is possible to observe a full gamut of behavioral regimes, from quasi-static [26-29]to rapid energetic flows[30-35]. The fact that many industrial handling processes make use of some form of mechanical vibrations[10, 11] to either enhance or induce motion provides a strong motivation to pursue research focused on unraveling governing physics that dictates observed behavior. It is well-know that particle masses can be fluidized through the application of energetic vibrations, or its bulk density (or solids fraction[1]) can evolve to a rather ordered structure with dislocations [5, 36-44]. In fact, the degree to which the density grows and characterization of the microstructure has been the subject of extensive studies over many hundreds of years – starting with crystal structures. In between these two disparate states, other behaviors engendered through continuous vibrations have been

1 The ratio of the volume of solids to the volume occupied.

observed and studied, such as period doubling instabilities, arching, and surface effects [45-57].

An important and possibly critical mechanism is related to the coupling of energy into a particle assembly from a boundary – typically a supporting floor - via taps or continuous vibrations. In particular, one is interested in the propagation of momentum through particle contacts, the effect of collisional losses and relaxation to a rest state when the input is discontinued. This dissertation focuses on these issues for a seemingly simple one-dimensional column of inelastic, uniform spheres that are subjected to taps via a prescribed pulse applied to the supporting floor. The investigative approach involves discrete element simulations, in which the Walton-Braun linear loading-unloading model[58, 59] is used to approximate collisional interactions. A concise description of the methodology and the physical simulation model appears in Chapter 2.

The transmission of a pulse or wave through a granular chain is a well-studied phenomenon that continues to be of interest due to its relevance among other things to designing granular structures capable of mitigating impact loads. In 1984, V.F. Nesterenko[60] developed a continuum model to study the propagation of waves in compressed one-dimensional chains. His elastic, non-dissipative theory featuring Hertzian contacts predicted a solitary wave(or a soliton) propagating through the assembly. And although there is no energy dissipation in the model[2], the nonlinearity of the contact interactions isan important feature. The soliton has been experimentally validated by several groups ([61],[62-64]and [65]). More recently, a continuum model

---

2 Because energy loss is an inherent attribute of real particles, contact models necessarily must incorporate dissipation so that one is able to study behavior beyond the short-time scale over which waves propagate.

was derived[66], based on a locally averaged limit as the number of particles goes to infinity, which incorporates collisional dissipation via simplified linear loading-unloading contacts. Most significantly, it has been shown through rigorous analysis that this model admits soliton-like solutions in the perfectly elastic case.[67].

The literature survey that follows is organized from the perspective of the time scale relevant to the phenomenon under scrutiny: (1) motion of the column from the onset of the tap through its collapse to a rest state –expressed as 'long time scale'; and (2) dynamics in accord with the propagation of the wave disturbance through the column – designated as 'short time scale'. By far, there has been a great deal more written on (2) involving theory, experiments and simulations, while papers related to (1) are comparatively few. Consequently, this dissertation is primarily focused on the long time scale behavior of the tapped column.

1.2 Literature Review – Long Time Scale

In 1990, Bernu and Mazighi[68]considered the problem of N inelastic spheres (restitution coefficient e) striking a wall (moving at constant velocity) in the absence of gravity. They reported the condensing of the spheres onto the wall below a critical restitution coefficient $e_c = tan^2\left(\pi\frac{N-1}{4N}\right) \cong 1-(\pi/N)$for $N \gg 1$. Several years later[68], they communicated their results on the steady states of a vibrated column of inelastic beads, where three identified phases (labeled as gas, partially-condensed and collapsed) could be characterized by $(1-e)N$.In 1993, Clement et al. [69]reported experimental and simulation findings on a continuously vibrated column of inelastic spheres, for which the principal breakthrough was that transitions between 'solid' to a fluidized state took place

with an increase in the external acceleration $\Gamma := a\omega^2/g$(a is the tap amplitude and ω is the frequency). They also examined the column's mean dilation as a function of N, as well as the dependence of profiles of density and kinetic energy on Γ. A discrete element study by Luding et al. [70]considered the same problem, in which one of the primary parameters was a normalized expansion (or dilatation) defined as$\lambda := \langle y_N - y_1 \rangle / a\Gamma$. For large $\Gamma > 10$, their data suggested that $\lambda \sim a\Gamma$ so that in the fluidized regime, the dimensionless energy $a\Gamma$ was the proper scaling parameter.The relative height of the mass center was found to represent the average behavior of the entire column, which scaled with $N(1-e)$.

In 1999, Goldshtein et al. [71]reported on both hard and soft-sphere simulations in which a column of slightly inelastic particles within a closed-end tube of length $L$was energized via periodic motion of a piston in the absence of gravity. Periodic oscillations of the column (equal to the vibration period of the piston) in the tube were found for sufficiently large amplitudes that featured constant velocity shock waves propagating across the tube (to the closed end) and back. Computations of the average kinetic energy per particle suggested a square dependency on tap frequency ω, such that its maximum scaled with $(\omega L)^2$. In 2001, the same authors presented results [72] on resonance oscillations in the tube. It was reported that the material move back and forth periodically with frequency f/n, where n is a positive integer such that the oscillation pattern was governed by the shock wave transmitted through the column. Then, in 2001, Alexeev et al. [73]extended their earlier work to investigate (via a discrete element simulations) liquid-state / solid state regimes of vertical, sinusoidal vibrations (amplitude a and frequency ω) applied to a column of inelastic spheres under gravity. Dissipation was

incorporated into the contact model via a non-linear (displacement-weighted) dashpot with coefficient depending on particle material parameters. They were able to classify the liquid state via the dependence of the kinetic energy of the relative motion of the particles $E_{rel} := \frac{1}{N}\sum_{k=1}^{N}(\dot{y}_{k-1} - \dot{y}_k)^2$and the mean-free-path $\lambda_{mp} := \frac{1}{N-1}\big(y_n(t) - y_1(t) - d(N-1)\big)$on the system dissipation parameter$\varepsilon_{dis} := N(1-e)$.As a measure of the intensity of the relative motion between particles, E_{rel} was perceived to be independent of ε_{dis} for the liquid state when $\varepsilon_{dis} > 3$, representing highly dissipative particles. Moreover, an upper bound for the maximum value of the relative kinetic energy was identified as$E_{rel} < 0.16(a\omega)^2/N^{\frac{2}{3}} = 0.16\Gamma ag/N^{\frac{2}{3}}$, valid for $\Gamma > 4.75$ and $4.2 \leq \varepsilon_{dis} \leq 70$.The authors thereby delineate a highly dissipative column to be one in which the maximum relative kinetic energy is bounded as described above. Graphs of λ_{mp}versus tap acceleration Γ indicated that for dissipative particles ($\varepsilon_{dis} > 3$), the mean free path $\lambda_{mp} \cong 0$ for narrow ranges of Γ, which the authors reference as 'repacking regions'. And thus, as Γis increased, the system undergoes a sequence of transitions from a fluidized state to a solid-like (repacked) state. Upon renormalizingλ_{mp} by $gN^{5/3}/\varepsilon_{dis}(a\omega)^2$so that $\hat{\lambda} := \frac{\lambda_{mp} gN^{5/3}}{\varepsilon_{dis}(a\omega)^2}$ over a range of ε_{dis} values the, there was a collapse of the data, from which $\lambda_{mp} \lesssim 0.4\frac{\varepsilon_{dis}(a\omega)^2}{gN^{5/3}}$ for $\Gamma \geq 4.75$. The latter bound suggests the non-intuitive behavior that in the fluidized state, there is more dilation as dissipation increases. Further, all systems with large dissipation that are vibrated with sufficient energy undergo transitions from an expanded ('liquid') to the compacted ('solid') state.

1.3 Short Time Scale

This section focuses on papers that are concerned with phenomena that take place over a time duration needed for a disturbance wave to propagate through the column. Although the subject matter of this dissertation is on the long-time dynamics of the column, this brief survey is included with the intention of presenting a larger picture of the complexity of the system. Because the scale of the literature is quite extensive, in what follows, only a small, representative subset of the important theoretical, experimental and simulation findings is discussed.

1.3.1 Theoretical Approaches

Perhaps one of the most significant papers is that of Nesterenko[60], who in 1984 developed a theoretical model that predicted the existence of a soliton (wave) propagating through a compressed chain of inelastic spherical beads governed by Hertzian contacts. Subsequently, various aspects of the phenomenon were explored, notably S. Sen and colleagues, and others. (See for example [74-88]).

In 1985, Nesterenko and Lazaridi[89]numerically solved the model reported in [60] for a granular chain against a rigid wall that was impacted by a piston on the free end. The disturbance decayed into a train of solitary waves, which were reflected by the rigid wall. The soliton phase velocity was found to be in agreement with the original model. In 1994, Nesterenko[90]described the soliton solutions and a sonic vacuum type which comes from the rapid decomposition of an initial disturbance with steep fronts into the sequence of pulses. Experimentally measured forces transmitted from initial taps were observed to agree well with numerical calculations. The influence of gravity and nonlinear nature of the contacts on the propagation of a signal down long chains

(typically 1000 to 5000 particles) under weak to strong impulses was examined by Hong and Xu[91]. The weak impulse spawned as weakly nonlinear, oscillatory signal in the chain, while the strong impulse generated a solitary signal. For both type of pulses, power-law behavior of the signal as a function of the depth was observed. The effect of gravity for the strong impulse was negligible so that the system could be viewed simply as a horizontal chain. The literature on uniform chains is quite extensive (for example, see [65, 83, 88, 92-101]) so that a complete survey is beyond the scope of this survey.

There has been great interest in 'decorated' chains as these one-dimensional structures have been shown to generate fascinating behavior, such as band gaps [80, 102, 103] and impulse mitigation [104, 105]. For example, Harbola et al. [106]analytically studied decorated chains for various arrangements of smaller spheres placed between larger spheres. The mapping of decorated chains into 'effective' undecorated chains allowed the authors to develop analytical results via the binary collision approximation for pulse propagation in the original decorated chains. The authors continued this work in a follow-up paper [107] that included variation in the particle radius as well.

1.3.2 Experiments

Experimental validation of the predictions of Nesterenko's theory was reported by Falcon[61], Job[62-64], Santibanez et al. [65], and others. In 1997, Coste et al. [78] conducted experiments in which a force was applied to one end of a horizontal chain of beads, resulting in very good agreement with predictions from Nesterenko's theory [89] for the velocity and shape of the solitary waves. For zero static pre-compression, the wave velocity was found to be proportional to the $1/6$ power of the maximum amplitude of the wave. And with a static pre-compression, the wave velocity was inversely

proportional to the ratio of the maximum force and static pre-compression. In 1998, the same group [61] conducted another experiment in which the position and net force on each sphere was measured for a column dropped down an enclosing glass tube to the floor. They reached the follow conclusions from the data.

1. The largest force experienced by the floor is independent of the number of particles N in the column.

2. The duration of impact of the column with the floor varies linearly with N.

3. The velocity of the deformation wave transmitted through the column was measured, consisting (first) of a compression wave propagating up to the top sphere, followed by an expansion wave moving downwards.

4. The measured 'effective restitution coefficient ε_{eff} was found to be in reasonably good agreement with Luding et al.'s hard-sphere simulation results, i.e., ε_{eff} is reduced as N increases.

Moreover, they were able to explain the first three findings above via Nesterenko's theory for Hertzian contacts between the particles of the column. In 2005, Job et al. [62] measured the solitary wave propagation of a granular chain bounded by a rigid wall without static pre-compression. Dynamic impulses measured through force sensors were in good agreement with Nesterenko's theory. It was observed that the reflected wave depended on the material properties of the wall. In 2006, the same group reported experimental results on tapered chains [108] to demonstrate its shock attenuation capability. The radii of the spheres r_i chosen in accordance to the rule $r_{i+1} = (1-q)r_i$, where $q = 0.056$ or 0.0827, resulted in a reduction of the wave amplitude coupled with an increase in its speed. The speed ratio of the solitary wave $\frac{v_{n+1}}{v_n} = [\frac{2e}{1+(1-q)^3}]^{1/5}$ was agreed very well with numerical predictions of Sen et al.[109].The authors published their experimental findings [63] on solitary waves and solitary wave trains in 2007 for mono-disperse and stepped chains. An explanation of the mechanism responsible for the

formation of either a solitary wave or solitary wave train was offered that involved the magnitude of the striker force and material properties of the chain.

If the striker force is larger and force duration on the chain is shorter, then a single solitary wave is generated. If striker force is smaller (like the stepped chain from large balls to small balls) and force duration time is longer, then a solitary wave train will emerge. The authors also concluded that the force at the interface will be an exponential decay function of the duration time.

In 2009, this group presented their experimental results [64] on energy localization of a granular chain. They pointed out that the wave propagating inside the chain will cause a local strain gradient that will excite localized oscillations. And the amplitude of these oscillations will be enhanced by the presence of a spatial gap near the tap. The nonlinear localization traps some energy and this will play an important role in wave mitigation. In 2011 [65], they reported experimental results on the interactions of two solitary waves. When the two counter-acting waves collide, they cross each other with a small phase shift due to nonlinear interaction. This has been predicted previously from simulations by Sen et al. Also, this collision effect is independent of viscoelastic dissipation. More importantly, a secondary wave was observed when two equal amplitude and synchronized waves collide, thereby corroborating the numerical prediction of secondary waves. Also, as observed in simulation results, the secondary wave is stronger when collisions occur among an even number of particles and the amplitude of the secondary wave is proportional to the amplitude of the initial wave. However, experimentally measured wave amplitude were slightly larger than numerical

predictions – a discrepancy attributed to the rolling effect at the bead contact during the wave propagation.

1.3.3 Simulation Studies

In 1995, Sen and Sinkovits[110]examined the sound speed in a granular column subjected to weak and strong perturbations (i.e., a downward velocity was applied to the top particle) via simulations. The interaction potential was given by

$$V(\alpha_{ij}) = \begin{cases} C(\alpha_{ij})^n, & \|\boldsymbol{r}_i - \boldsymbol{r}_j\| \le \alpha_c \\ 0, & \|\boldsymbol{r}_i - \boldsymbol{r}_j\| > \alpha_c \end{cases},$$

where $\boldsymbol{r}_k$ is the position of particle k, is the cut-off distance for V beyond which there is no force between the particles, and C is a constant.For weak disturbances, the speed was found to vary with depth according to$z^{0.5(1-(n-1)^{-1})}$ in agreement with elasticity theory. They extended their work to investigations [111] on two-dimensional systems (disks) with voids and randomly distributed mass defects.

In 2000, Sen et al. reported [112] that the crossing of identical solitary waves in a granular chain with Hertzian contacts spawned a secondary wave having an energy of approximately 0.5% of the original solitary waves. The authors argued that secondary waves were a fundamental property of discrete systems.

In 2007, Sen et al. published an extended review summarizing principal results and discoveries related to disturbance propagation and solitons in chains, focusing on nonlinear effects, the shape and speed of the wave, the formation of secondary waves and solitary waves in tapered and decorated chains. In the same year, Rosas et al. [113] reported findings concerning a two-wave structure in strongly nonlinear dissipative chains.

The influence of dissipation in the contact model has also been investigated, notably in the work of Liu et al. [114-116] and [88, 117, 118]. Results from simulations compared favorably with experiments findings of Sen et al. with regarding to the formation of secondary waves.

1.4 Objective

The objective of the research is to use DEM simulation to analyze the dynamics of a granular column for both long and short time scales. Long time scale problems are mainly focused on the column expansion and cooling process; trying to explain how tap parameters and material parameters affect the dynamics of the system and how energy evolves inside the system. For the short time scale part, the problem is to explain how the shock wave propagates through the column. During this process, it is also of interest to determine how the dissipative elements in the column affect the wave and furthermore make some comparison with other researcher's work.

1.5 Outline of Dissertation

The remainder of this dissertation is organized as follows. Chapter 2 describes the discrete element simulation model and arrangement of physical problem. Chapter 3 presents the results for short time scales with a focus on the propagation of waves in the column and some comparisons with previous work by Falcon et al. Chapter 4 presents and discusses results of cooling dynamics of the system, while Chapter 5 discusses expansion dynamics of the column. Chapter 6proceeds with a discussion of results

regarding Poincaré maps computed from the data in the 1D dynamical granular system. Finally, Chapter 7 contains the conclusions and recommendations for further work.

CHAPTER 2

SIMULATION METHOLODY AND DESCRIPTION OF THE PROBLEM

2.1 Introduction to the Discrete Element Method

The development of the discrete element method (DEM) is attributed to Peter Cundall [119] in the 1970's independently as an outgrowth of molecular dynamics simulations used in the statistical physics community [120, 121]. The code that was used in this dissertation was developed by O. Walton [58, 59, 122, 123] in the early 1980's to investigate uniform shear flows of inelastic, frictional spheres. The basic idea is the numerical solution of the equations of motion of a system of particles that interact via known or approximate collisions models. Essentially, there are two classes of models. Hard sphere interactions [124, 125] feature instantaneous collisions in which post-collisional velocities are determined via a collision operator that is a function of the pre-collisional velocities and three material properties, i.e., a normal coefficient of restitution, a tangential restitution coefficient and a friction coefficient. Soft sphere model feature finite duration interactions in which the contact forces are functions of an allowed, physically realistic overlap between particles.

There are significant scientific and technical challenges associated with extracting and processing meaningful data from particle-based simulations, not the least of which is the modeling of physical problems involving transitions to chaotic behavior accompanied by sensitivity to initial conditions and convergence of results. Moreover, despite improvements in computing infrastructure that allows one to examine relatively large systems of the order of hundreds of thousands to millions of spherical particles

interacting with relatively simplistic (yet realistic) contact models, this is still a small sample as compared real granular solids. Consequently, the extraction of physically meaningful results for comparison with experimental measurements often requires

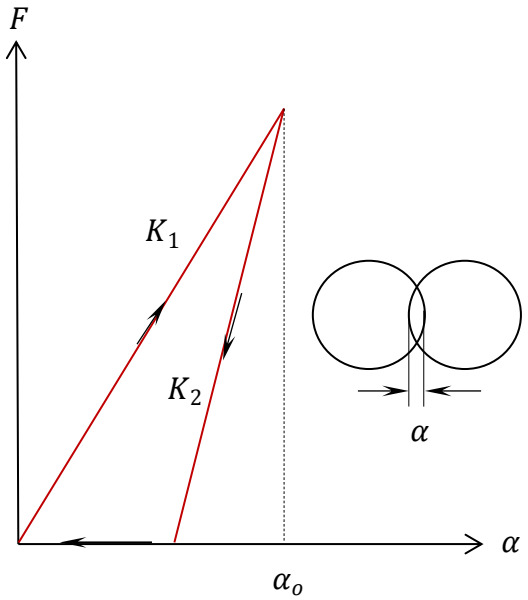

Figure 2.1 Illustration of the linear loading – unloading normal force model.

ensemble averaging. Lastly, particles used in the bulk solids industries may vary greatly in size and shape, which adds enormous complexity due to the need to incorporate realistic interaction models and efficient contact detection strategies.

In the work presented in this dissertation, the Walton-Braun model is used [123], in which particle load on a linear spring of stiffness K_1 and unload on another linear spring of stiffness K_2 such that $K_2 > K_1$. In simplified form, the normal force (along the line of centers) between two contacting spheres can be written as,

$$F = \begin{cases} K_1\alpha, & loading \\ K_2(\alpha - \alpha_o), & unloading \end{cases} \tag{2.1}$$

where α is the overlap and α_o is the overlap when the unloading force goes to zero. At

this point, the two spheres separate from each other at constant velocity. Figure 2.1 depicts the model. It can be shown [126] that the model produces a constant coefficient of restitution given by,

$$\mathrm{e} = \sqrt{\frac{\mathrm{K}_1}{\mathrm{K}_2}} \tag{2.2}$$

which is valid for spheres whose relative normal impact velocity is of the order of 1 m/s or less [127]. The equations of motion are explicitly integrated via a Verlet leap-frog method [128] in which the time step is based on the loading period partitioned into n sub-steps. Thus, the time step given by,

$$dt = \pi \frac{e}{n} \sqrt{\frac{m}{2K_1}} \tag{2.3}$$

For the value of the loading stiffness used in this dissertation ($K_1 = 2.80 \times 10^5\ N/m$), particle density ($\rho = 1{,}200\ kg/m^3$ which corresponds to acrylic), $dt \sim 10^{-6}\ s$. This value was sufficient to ensure overlap of less than approximately a percent of the diameter in accordance the behavior of real colliding spheres. However, simulations conducted to examine the wave speed (Chapter 3) required that the time step be reduced by two orders of magnitude. Details on the actual structure of the code can be found in several other sources (e.g., [129, 130]) and so they are not included in this work.

2.2 Description of the Physical Problem

The problem of interest in this dissertation involved a column of uniform, inelastic spheres that are supported by an rigid (infinite mass) floor, to which is prescribed a half-

since pulse having displacement amplitude a/d and frequency f. The period of the pulse is given by $\tau = 1/2f$. Each pulse is followed by a relaxation interval denoted by t_r. Figure 2.2 depicts the motion applied to the floor as well as a graphic showing the column of spheres. In order to ensure that the particles remained stacked along their lines of centers, no motion was permitted in the lateral directions by commenting out the

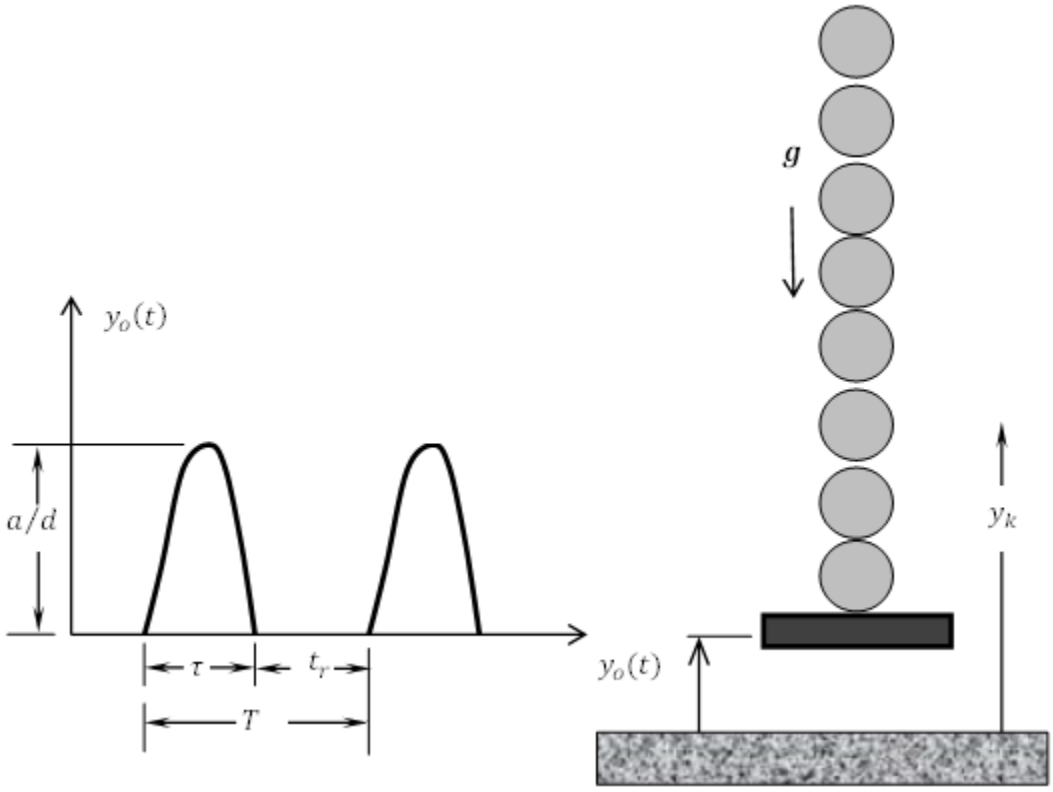

Figure 2.2 Graphic of the physical problem, showing the form of the floor's motion.

integration equations in those directions. The coordinate system is such that gravity acts in the $-y$ direction.

2.3 Parameter Space and Diagnostic Quantities

The space of parameters for the simulations in this dissertation consists of variables that affect the behavior of the system. Table 2.1 lists these parameters (number of spheres N, restitution coefficient e, tap amplitude a/d, frequency f, and relaxation time t_r) and their range of values.

Table 2.1 Parameter Space of the Simulations

N	e	a/d	f (Hz)	t_r (s)
$1 \leq N \leq 100$	$0.04 \leq e \leq 0.99$	$a/d \leq 1.5$	$1 \leq f \leq 30$	$0 \leq t_r \leq 0.4$

Various diagnostic quantities are computed in order to understand the physical behavior of the column. Each of these quantities is introduced and explicitly defined in the chapter in which they are first used.

CHAPTER 3

WAVE DYNAMICS OF GRANULAR COLUMN

This Chapter will discuss the dynamics of the disturbance wave transfer through the column as a result of the tap from the floor. In an attempt to compare the computed wave speed with experimental measurement [61], all results described in this Chapter are for a column of $N = 40$ stainless spheres such that $d = 0.008\,m$, $\rho = \rho_{s-steel}$ ($m = 0.002\ kg$) , and $e = 0.95$.

3.1 Formation of the Wave

The displacement of the floor causes it to interact at the outset with the first particle through a transfer of momentum that propagates upwards to the top. Depending on the energetics of the tap, the column will undergo some level of dilation. However, if the frequency of the tap is not large enough (regardless of the amplitude), the column will simply move in tact with the floor and there will be no dilation. (see Chapter 5, Section 5.5 for details).

The time scale over which the disturbance imparted by the floor propagates to the top of the column is termed the *short time scale*. The relationship between dynamics over this scale (which is intimately connected with the contact model), and what occurs over the duration over which the column dilates and returns to a rest configuration remains a topic requiring further research. However, the short time scale dynamics will have a significant role in distributing the kinetic energy to the particles, which in turn affects the ensuring behavior of the column.

Upon imposition of the tap, contact forces (via the $K_1 - K_2$model) between particles are activated as a result of an increase of the overlap beyond pre-tapped values (due to gravitational overburden). As the explicit integration scheme marches forward,

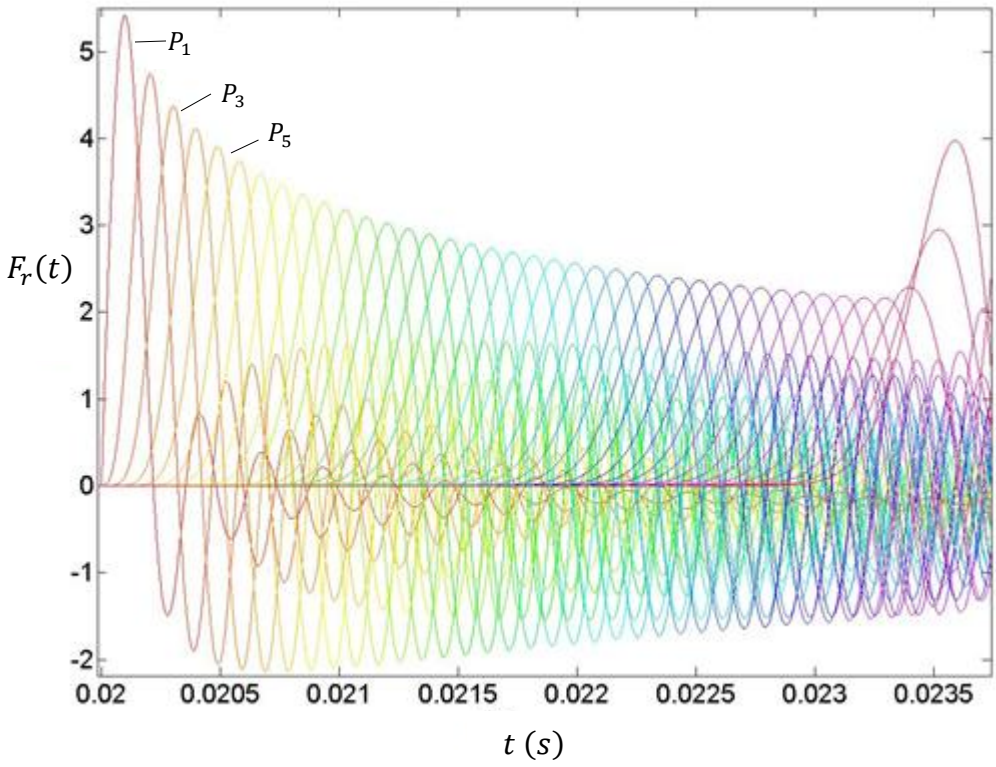

Figure 3.1 Evolution of the resultant force (designated by the different line colors) in a 40 particle column subjected to a single tap such that $a/d = 0.50$, $f = 10\ Hz$, $e = 0.95$. The labels P_1, P_2, P_3 designate particles 1, 3 and 5, respectively.

the first particle (nearest to the floor) undergoes a displacement that alters the overlap between it and the second particle. The process continues in this fashion until the top of the column is reached – constituting a compression wave. Effectively, the tap causes a small change in the density profile (due to the overlaps between particles) that is reflected by each particle undergoing a net (or resultant) force that evolves to produce this compression wave. From a broader perspective (and in accord with the experimentally

determined delineation of [1]), the tap first causes a compression wave that propagates from the bottom through the column to the top sphere, followed by a downward moving expansion wave.

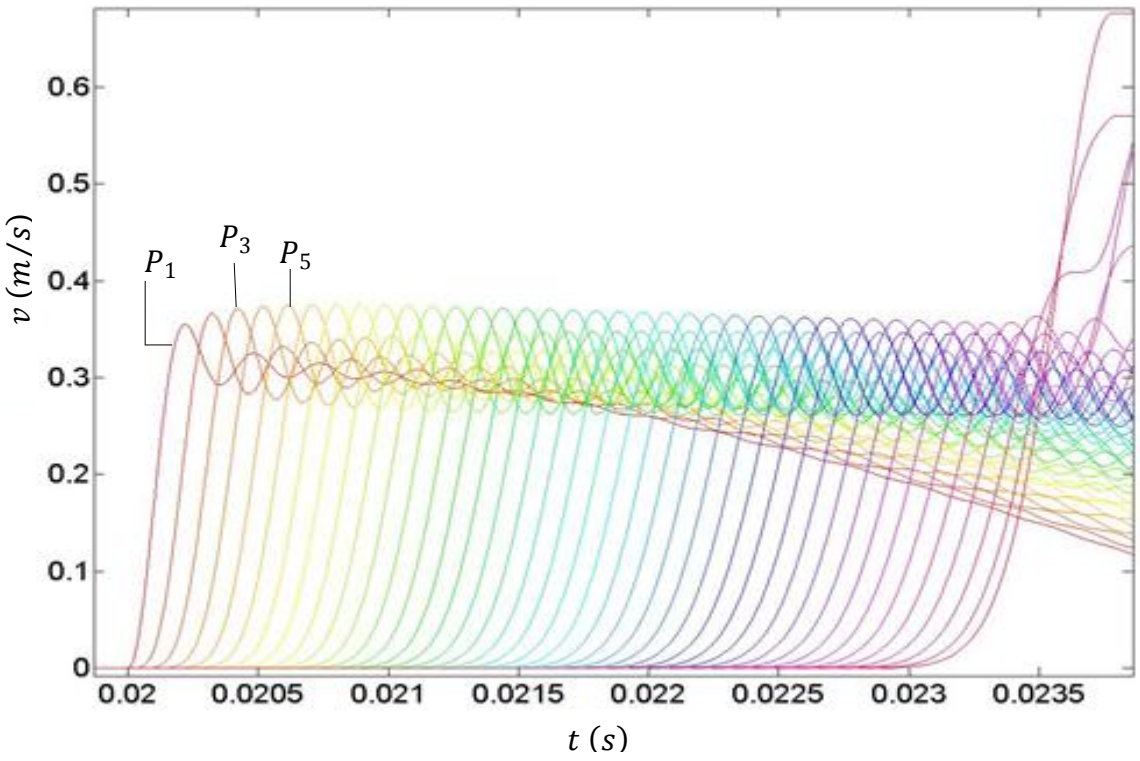

Figure 3.2 Evolution of the particles velocities $v\ (m/s)$ (different colors) in a 40 particle column subjected to a single tap such that $a/d = 0.50$, $f = 10\ Hz$, $e = 0.95$. The labels P_1, P_2, P_3 designate particles 1, 3 and 5, respectively.

3.2 Wave Speed

The objective here is to measure the speed of the compression wave, gravity is set to zero and particles are stacked on top of each other. Consequently, when the tap is initiated, all inter-particle contact forces are zero. The speed of transmission of the wave is measured

carefully monitoring the evolution of resultant forces (acting at particle centers). For any particular sphere, this resultant is due to the contacts forces from the two adjacent particles. Alternatively, it is possible to quantify the wave speed from cross-correlations

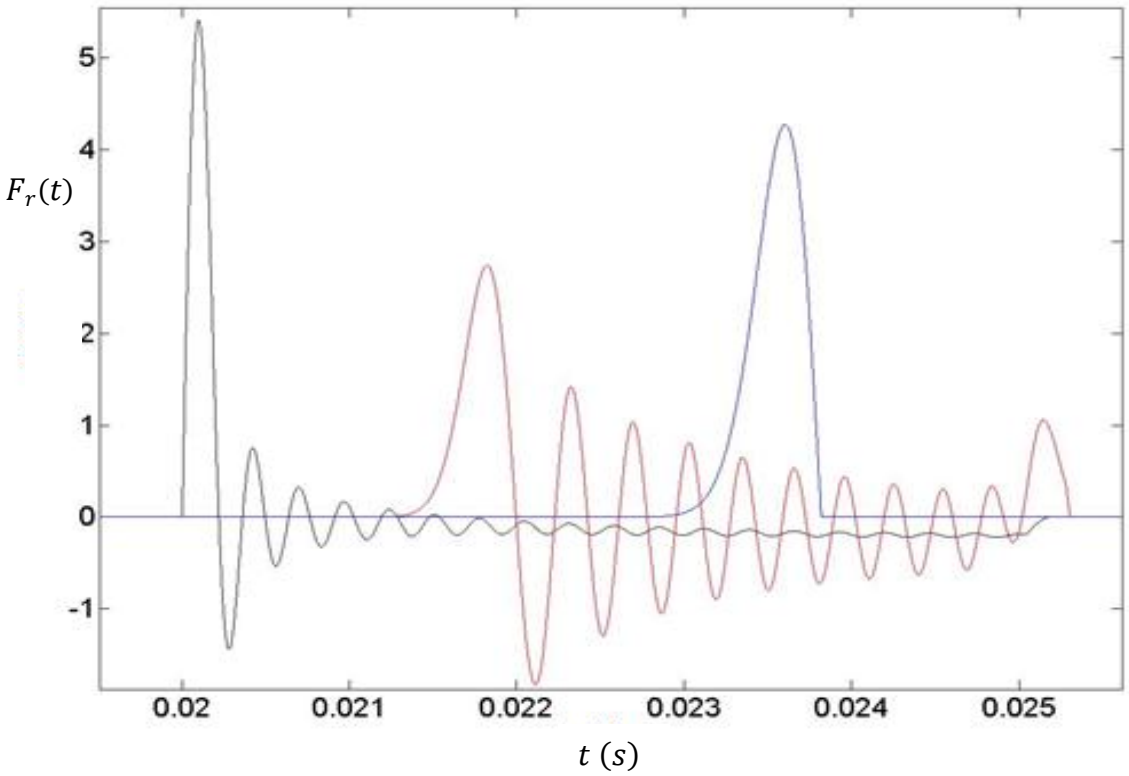

Figure 3.3 Resulting force versus time for particle 1 (black line), particle 20 (red line) and particle 40 (blue) in a column of 40 stainless steel spheres tapped at $a/d = 0.50$, $f =\ 10\ Hz$, $e = 0.95$.

of particle velocities. Figure 3.1 shows the resultant force $F_r(t)$ acting at the center of each sphere (different line colors) in a 40-particle column that is subjected to a single tap for which $a/d =$, $f =\ \ Hz$, and $e = 0.92$. The tap is initiated at $t = 0.02\ s$. Note that $T = t_r + (1/2f) = 0.45\ s$ so that time scale $0 \le t \le 0.24\ s$ in the figure is $0.488T$, or roughly half of a period. Particle velocities in the column are presented in Figure 3.2 where the labels $P_1, P_3 \text{and} P_5$ designate particles 1, 3 and 5, respectively. The wave is

transmitted through the entire column over a time interval $\Delta t_{sh} \sim (0.0235 - 0.02) = 0.0035\ s = 0.0078T = 0.07\tau$. Figure 3.3 shows the resultant force on particles 1, 20 and 40 as the black, red and blue lines, respectively. Positive values correspond to the

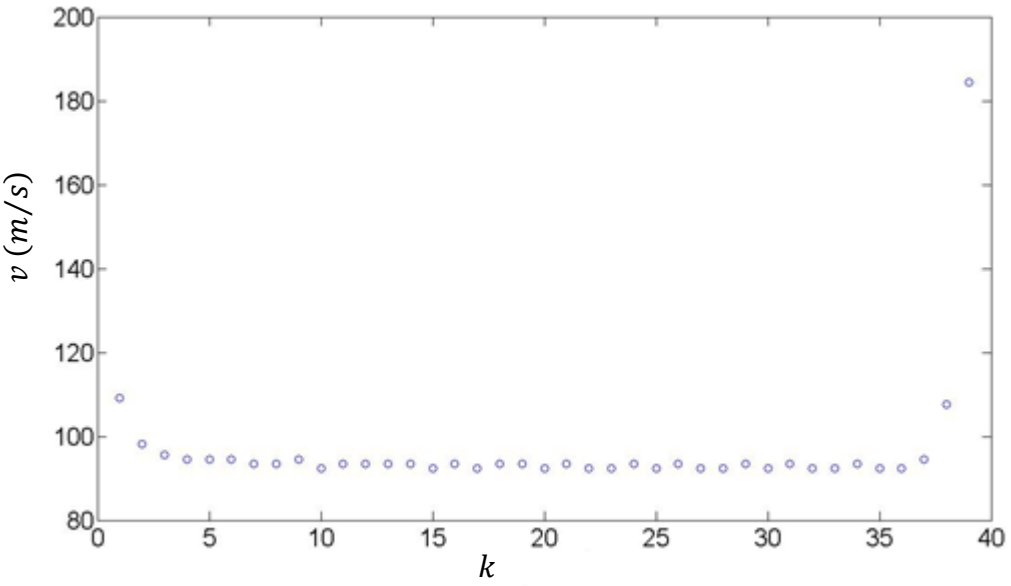

Figure 3.4 Velocity v_k^{k+1} as per (3.1) along the chain of particles, which is tapped at $a/d = 0.5$, $f = 10\ Hz$, $e = 0.92$ and $N = 40$.

direction opposite gravity (upwards). The first particle experiences the largest peak in the resultant force accompanied by a drastic reduction after a very short time interval. The other particles also attain a maximum value which decreases and oscillates. The reduction in force amplitudes is due to dissipation inherent in the contact model, while the oscillations are characteristics of time variations in forces from the adjacent (touching) particles. The time delay between signals can be used to estimate the speed of the compression wave. The threshold value used to decide when a sphere undergoes a force is selected to be $10^{-6}\ N$. That is, for each particle $(1 \leq k \leq 40)$, the time $\hat{t}_k$ when $F_r^k \geq 10^{-6}\ N$ is when the compression wave arrives. For each pair of particles, a velocity v_k^{k+1} is computed as

$$v_k^{k+1} = \frac{d}{\hat{t}_{k+1} - \hat{t}_k} \tag{3.1}$$

Figure 3.4 shows v_k^{k+1} versus particle number k. The estimated wave speed is given by $v_1^{40} = \frac{39d}{\hat{t}_{40} - \hat{t}_1} = 93.35\ m/s$. By dropping a column of 40 spheres onto a plate, Falcon et al. [61] measured compression wave speeds between $557\ m/s$ to $628\ m/s$, which were found to be in good agreement with theoretical arguments based on Hertzian contacts. Several possible reasons for the discrepancy with the simulations are conjectured: (a). value of K_1 used in the simulations; (b) strength of the tap as compared to the impulse exerted by the floor in Falcon et al.'s experiments; (c) difference between applying a tap (as in the simulation) and dropping the column; (d) nonlinear effect of Hertzian contacts as opposed to bilinear springs.

Consider the following simple paradigm. Let the displacements from equilibrium of three adjacent particles be denoted by u_{i-1}, u_i, u_{i+1}. Also suppose that the equilibrium spacing between particles is Δx, which in the case of the simulation corresponds to the particle diameter d. As depicted in Figure 3.5, the force on the i^{th} particle is

$$F_i = K(u_{i-1} - u_i) - K(u_i - u_{i+1}), \tag{3.2}$$

where a spring of stiffness K is assumed to act. Application of Newton's second law yields,

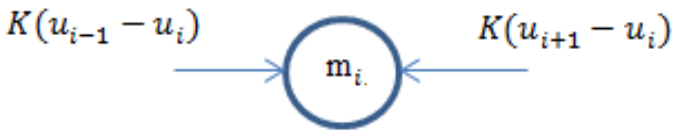

Figure 3.5 Force balance on the i^{th} particle.

$$m\frac{d^2u_i}{dt^2} = K(u_{i-1} - 2u_i + u_{i+1})$$
$$\Rightarrow \quad m\frac{d^2u_i}{dt^2} = K\Delta x^2\left[\frac{u_{i-1} - 2u_i + u_{i+1}}{\Delta x^2}\right] \tag{3.3}$$

And thus, (3.3) suggests a wave speed $c \sim \Delta x\sqrt{K/m}$. Upon substitution of $\Delta x = d$, $K := K_1 = 280{,}000\ N/m$, and $m = 0.002\ kg$ into the latter expression, one finds that $c = 94.66\ m/s$, which is consistent with the simulation result, but again very different from the findings of Falcon et al. [61]. Hertzian theory maintains that the normal force between two contacting spheres is $f_H = K_h\alpha^{3/2}$, where α is the overlap between the spheres and $K_H = \frac{\sqrt{d}}{3}\frac{E}{1-\nu^2}$, where E is the elastic modulus and ν is Poisson's ratio of the material. Suppose that the average overlap between interacting spheres in the column $\alpha_{max} = 0.001d$, and the linear loading stiffness K_1 is approximated as the slope

$$\widehat{K}_1 = \frac{K_H(0.001d)^{3/2}}{0.001d} = K_H\sqrt{0.001d} \tag{3.4}$$

For steel spheres of diameter $d = 0.008\ m$, $K_H = 6.9716\ \times 10^9\ \frac{N}{m^{3/2}}$ so that by (3.4), $\widehat{K}_1 = 1.972\ \times 10^7\ \frac{N}{m}$. A substitution of $\widehat{K}_1$ into $c \sim \Delta x\sqrt{K/m}$ yields $c \cong 794\ m/s$, which is in better agreement with the experiments. Consequently, for the bi-linear model in the simulation code, the value of the stiffness is an extremely important factor in obtaining quantitative agreement with physical experiments.

The final observation to be made regarding the velocities shown in Figure 3.2 is that although there are some oscillations, the peak speed acquired by each particle does not change. This is a characteristic of the linear nature of the loading /unloading contact law, that is, the compression wave speed (for a fixed tap input) in this model is dictated by the loading stiffness. This would not be the case for Hertzian contacts in which the

stiffness is a function of the deformation (or overlap) and is given by the slope of the loading curve, $df_H/d\alpha = \frac{3}{2}K_H\sqrt{\alpha}$.

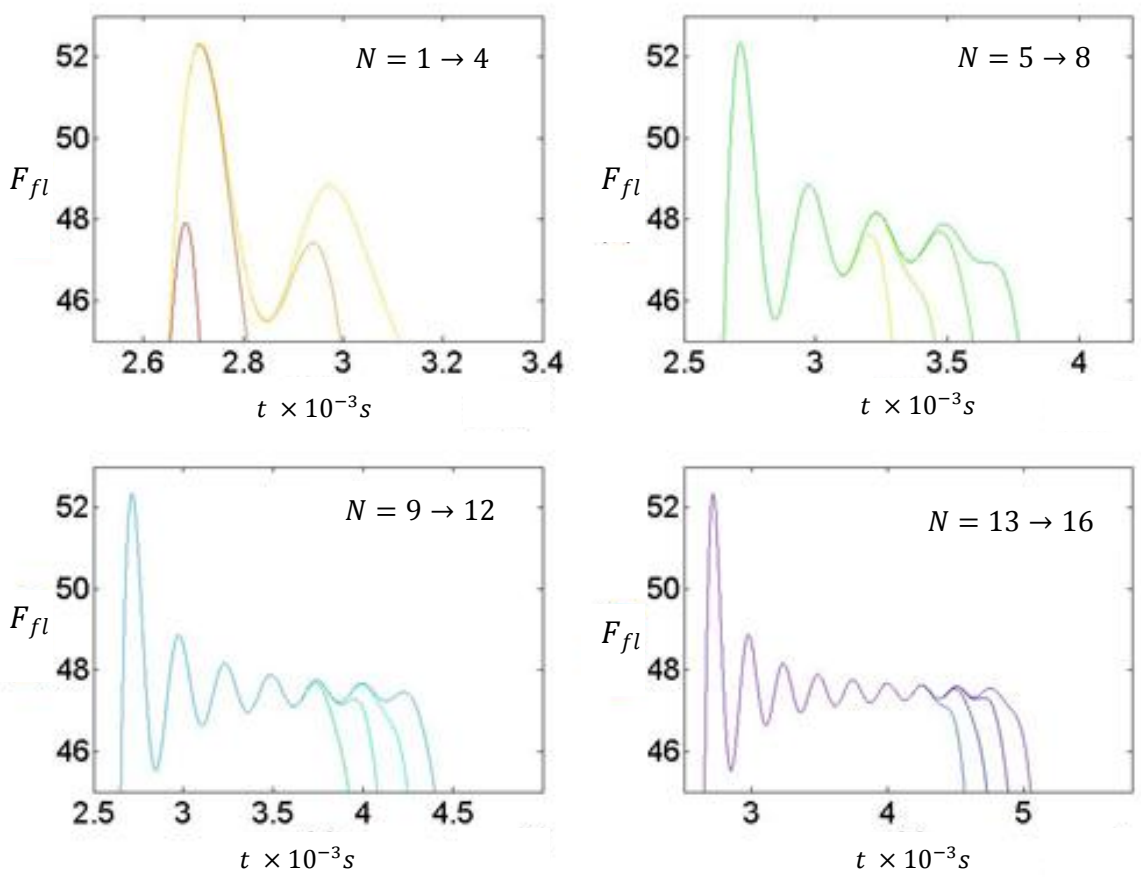

Figure 3.6 Evolution of the floor force (in Newtons) experienced by the floor as it is hit by the column of stainless steel spheres ($d = 0.008\,m, e = 0.95$).

3.3 Comparisons with Drop Test Experiments

Falcon et al. [61] conducted detailed experiments in which columns stainless steel beads were dropped collectively onto a floor. They reported on a number of important aspects of the physical problem, including: (1) evolution of the force experienced by the floor as a function of the number of spheres N in the column; (2) duration of the contact time of

the dropped column with the floor as a function of N; (3) compression wave propagation

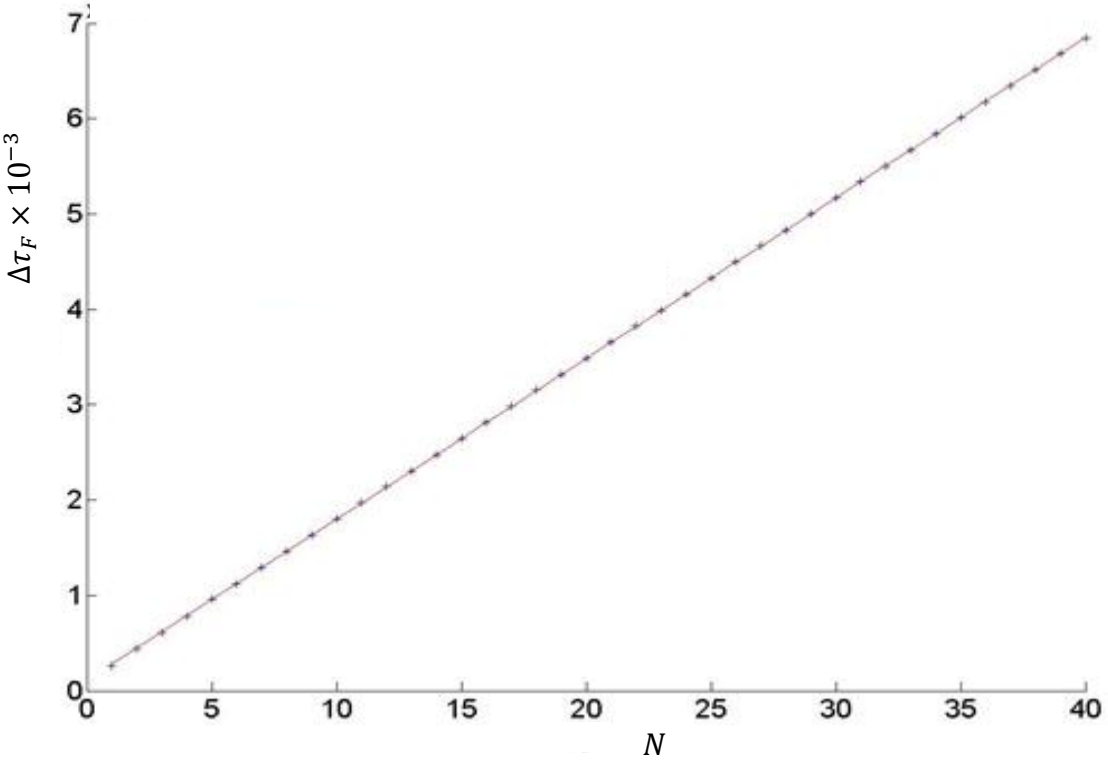

Figure 3.7 Contact duration $\Delta\tau_F$ of columns of stainless steel spheres with the floor as a function of N.

velocity; and (4) effective restitution coefficient of the column. With regard to (1), experiments showed that the floor force was independent of N – which is surprising as it contradicts one's physical intuition. Item (3) has already been discussed in the previous sections.

Simulations were carried out with the intention of making qualitative comparisons with the experimental findings – items (1), (2) and (4) above. It should be noted here as well that the relatively soft particles used in these simulations (as reflected in the loading stiffness $K_1 = 2.8 \times 10^5$) will have a significant effect on quantitative values that are computed.

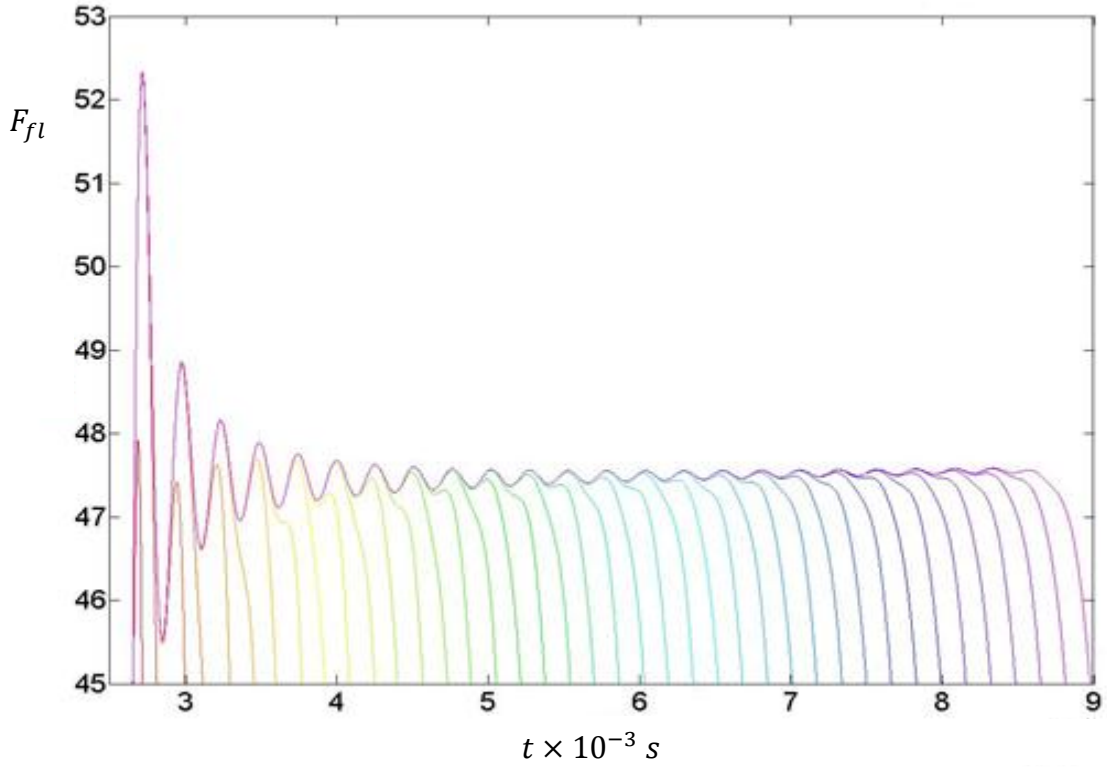

Figure 3.8 Evolution of the floor force (in Newtons) experienced by the floor as it is hit by the columns of stainless steel spheres ($d = 0.008\,m, e = 0.95$). Each color represents the result for a column of different number of spheres, $1 \leq N \leq 40$.

The time evolution of the force experienced by the floor as a function of the number of particles in the column measured in the experiments involved dropping each column from various heights above the floor. For $h = 5.1mm(h/d = 0.6375)$, the impact velocity $v_{imp} = \sqrt{2gh} = 0.316\ m/s$. In lieu of placing the column at distance h above the floor and then allowing gravity to pull it down, particles were assigned initial velocities $v_k = -v_{imp},\ k = 1, 2, \ldots, N$ so that the column struck the floor with velocity magnitude v_{imp}. The evolution of the force on the floor was then computed and results are plotted in Figure 3.6 for columns of size $N = 1, 2, 3, \ldots 16$. Results for the other columns ($N = 17, 18, \ldots 40$) were similar. Each sub-plot of the figure contains the evolution curves corresponding to the number of particle as labeled. With the exception

of $N = 1$ and 2, the forces evolve in the same manner with no discernible disparity in magnitudes. Moreover, for all column sizes, $F_{fl}^{max} \cong 52\,N$, and the time when this occurs is approximately the same for all column sizes, that is $t_{max}^{fl} \cong 2.7 \times 10^{-3}\,s$. The significant difference between them is the time instant at which the force goes to zero, which is essentially the duration of contact of the column with the floor. Very similar trends to Figure 3.6 were reported from the experiments (See Figure 4 in [61]). The fact that the floor force is found to be independent of N is counterintuitive, but this is probably related to the discrete nature of the column as a granular system. Indeed, one would expect that the maximum floor force would increase with the mass of a single body. The physical explanation given by Falcon et al. is related to the propagating compression wave from the impact and the rigidity of the floor.

The duration of impact of the column with the floor, denoted by $\Delta\tau_F$, is presented in Figure 3.7 for which a linear regression gives that $\Delta\tau_F = (1.685N + 1.137) \times 10^{-3}s$ (shown as the red line through the data points). The evolution of F_{fl} is shown in Figure 3.8 for all 40 columns. The linear behavior of $\Delta\tau_F$ versus N is also in excellent qualitative agreement with the physical experiments (See Figure 7 in [61]).

As a final comparison with the experiments, simulations were carried out in the absence of gravity ($g = 0$) to compute an effective restitution coefficient e_{eff}, defined as,

$$e_{eff} = \sqrt{\frac{\sum_{i=1}^{N}(v_i')^2}{\sum_{i=1}^{N}(v_i^o)^2}} = \frac{1}{N v_{imp}} \sqrt{\sum_{i=1}^{N}(v_i')^2} \tag{3.5}$$

The simulation procedure consisted of assigning $v_{imp} = -0.316\,m/s$ to all

particles so that the column descends to the floor uniformly until contact is made. For $i = 1, 2, \ldots N$, ,$v_i^o = -v_{imp}$ in equation (3.5). The primed velocities were determined by finding the time when the momentum of the system reaches its maximum positive value. This occurred when the bottom ball just leaves the floor. The results of this study are summarized in Figure 3.9. The decreasing trend of e_{eff} versus N agrees with the experiments (Figure 11 of [61]), although a much more extensive investigation is needed to match the data.

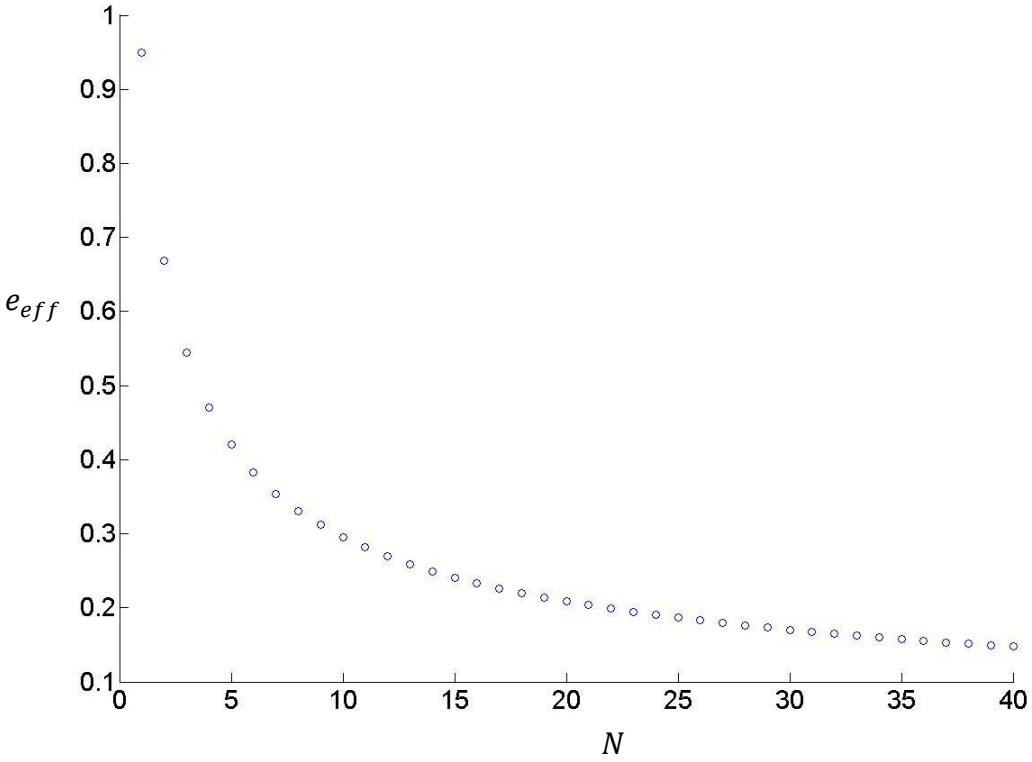

Figure 3.9 Effective restitution coefficient as per (3.5) versus N.

CHAPTER 4

COOLING DYNAMICS OF THE TAPPED COLUMN

This chapter presents the results of the findings on the dynamics of the tapped column as it evolves towards a state of zero kinetic energy. This evolution is typically given the name "cooling dynamics". Physically, one imagines that the application of a tap applied to the column causes it to dilate, the degree of which depends on the energy of the tap. Of course, this admits the possibility that the energy of the tap may not sufficient to cause dilation so that the phenomenon is simply the transmission of the impulse through the contacts. On the presumption that the system expands so that particle contacts are broken, there will then be a period of collapse characterized by dissipative collisions between the particles. Consequently, the question that will be addressed here concerns the time scale over which the collapse takes place.

4.1 Description of the Simulated System

As detailed in Chapter 2, the particle contact model employed for these simulations is the Walton-Braun linear loading/unloading soft sphere interaction. Here, the force between particles (along the line of centers) is a function of an allowed overlap between contacting spheres - typically of the order of $0.01d$. Loading via a spring of stiffness K_1 to a maximum overlap is following by unloading through a spring of stiffness K_2, such that $K_2 < K_1$. This model admits a constant coefficient of restitution given by $e = \sqrt{K_1/K_2}$. A tap is applied to the column through the motion of the floor in the form

of a half-sine wave of the form, $y(t) = \begin{cases} a\sin(\omega t), & 0 \le t \le \tau \\ 0, & \tau \le t \le T \end{cases}$, where $\tau = 1/2f$, a is the displacement amplitude and $\omega = 2\pi f$.

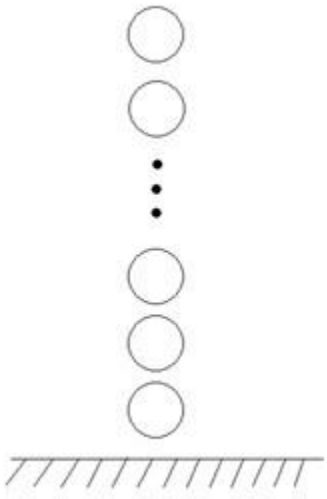

Figure 4.1 A column of N uniform spheres is depicted in an expanded state after the application of a tap.

4.2 Problem Description

It is intuitively clear that the dynamics of the system as it cools down must depend on the tap parameters, namely the dimensionless amplitude a/d and frequency ω, the number of spheres N, and the energy loss in a single tap as quantified by the restitution coefficient e. The reason is that these parameters in a sense control whether or not individual particles separate from one another as a result of the transmission of forces through the contact network (as depicted in Figure 4.1). It is possible that very low energetic taps may simply spawn the propagation of a wave through the column that merely kicks off the very top particle slightly. Alternatively, the column will simply follow the motion of the floor

when $a\omega^2/g < 1$. This behavior was shown in Chapter 3. Other parameters that may affect the dynamics include the loading stiffness K_1, material density ρ, and sphere diameter d. As pointed out in Chapter 2 (Section 2.3), an explicit integration time step of the order of $10^{-7}s$ is used instead of that dictated by the loading period $\Delta t = \frac{e}{n}\sqrt{\frac{m}{2K_1}} \sim 10^{-5}$ so that the influence of K_1 and ρ on the dynamics is not expected to be significant. Moreover, earlier simulation studies on vibration-induced densification [Zhang][3] indicated only small sensitivity to K_1 to within an order of magnitude of its value. For the results that follow, $d = 0.02m$, $K_1 = 2.8 \times 10^5\ N/m$, and $\rho = 1{,}200\ kg/m^3$.

4.3 Stopping Time of a Single Sphere

It is instructive to compare the theoretical 'stopping time' of a single sphere, denoted as t_s, with simulation results as a benchmark of the validity of the computational model. This will be done by determining the time required for the sphere, dropped from a distance h above the floor, to come to rest. To begin, suppose that the mass center of the sphere has an initial upward velocity equal to $a\omega$ after it interacts with the floor. In this simplistic analysis, detailed interaction dynamics of the impulsive motion of the floor on the sphere is ignored as this takes place over a time scale that is orders of magnitude smaller than the scale of interest in this analysis. The time required for the sphere is attain its maximum height above the floor is $a\omega/g$ so that it reaches the floor again at $t_1 = 2\,a\omega/g$. It then bounces back up at a reduced velocity based on energy loss

3 N. Zhang, "Vibration-Induced Densification of Granular Materials", Ph.D Dissertation, New Jersey Institute of Technology, January 2004.

characterized by the restitution coefficient e and returns to the floor in a time duration of $t_2 = e(2\,a\omega/g)$. The process is repeated so that time required for the third bounce is $t_3 = e^2(2\,a\omega/g)$, and in general, the time required for bounce k is given by $t_k = e^{k-1}(2\,a\omega/g)$. Thus, time required for n bounces is given by

$$t_s^n(1) = \sum_{k=1}^{n} t_k = \frac{2a\omega}{g}\sum_{k=1}^{n} e^{k-1} = \left(\frac{2a\omega}{g}\right)\frac{1-e^{n+1}}{1-e}\,, \tag{4.1}$$

where "(1)" denotes the stopping time for a single ball. Since $0 < e < 1$, one obtains,

$$t_s(1) := \lim_{n\to\infty} t_s^n(1) = \frac{2a\omega}{g}\frac{1}{(1-e)}\,. \tag{4.2}$$

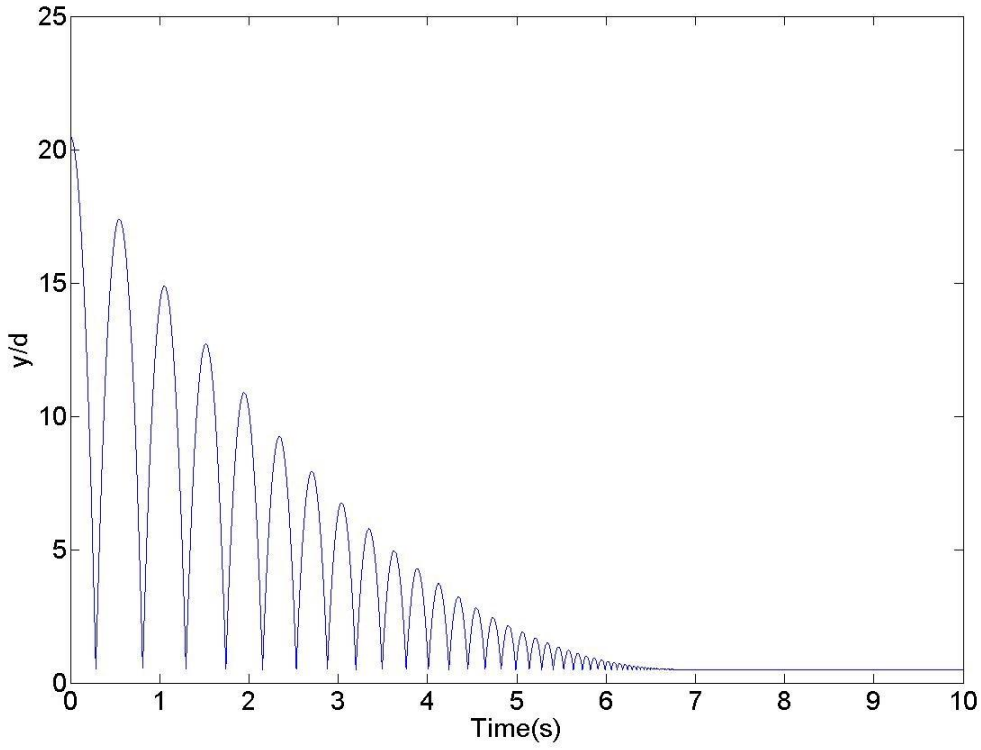

Figure 4.2 Trajectory y/d of a single sphere released from $h/d = 20$ above the floor.

Now suppose that the sphere is simply dropped from a distance h above a stationary a

floor so that the time to reach the floor $\sqrt{2h/g}$. This term replaces the $2a\omega$ in (4.2) so that the stopping time, denoted by t_{dr} is given by

$$t_{dr} = \frac{2\sqrt{2h/g}}{1-e} - \sqrt{\frac{2h}{g}} = \frac{1+e}{1-e}\sqrt{\frac{2h}{g}}. \tag{4.3}$$

A simulation is conducted in which a single sphere having a restitution coefficient $e = 0.92$ is dropped from $h = 0.4m = 20$ above a stationary floor, after which it executes a sequence of impacts with the floor (each of which causes a reduction in its velocity). The sphere trajectory is depicted in Figure 4.2. After many bounces, sufficient energy is lost through collisions so that the spring force is insufficient for the sphere to separate from the floor, at which point it undergoes very minute oscillations. The stopping time $(t_{dr})_{sim}$ is recorded at the instant that the oscillations are such that the system kinetic energy is less than or equal to $10^{-5}(KE_{max})$, where KE_{max} denotes the maximum value of the energy. The simulated stopping time $(t_{dr})_{sim} = 6.8450s$ is in very good agreement with $t_{dr} = 6.8536s$ as the predicted by equation (4.3). Section 4.5 includes a discussion of the stopping time criterion.

4.4 General Dynamical Features of the *N*-ball System

A portrait of the dynamics in the cooling process can be seen in the evolution of column mass center, kinetic energy, total energy (= kinetic + potential) and granular temperature as parameterized by the number of spheres N in the system. All of these quantities show an eventual decay as the spheres transition to their initial condition.

Figure 4.3 presents the normalized mass center trajectories y/d for $1 \leq N \leq 20$ as indicated by different colors, where the black line is the result for a single sphere. One

observes that as N increases, the time duration for the collapse is reduced as a result of greater collisional energy loss. Comparable behavior can be seen from the kinetic energy (normalized by $(a\omega)^2$) results of Figure 4.4 in that the time scale over which the system collapses is reduced as the number of particles increases. The system is at its peak dilation when the kinetic energy is a minimum. The evolution of the kinetic energy to a maximum value near $t \cong 0$ is visible in the inset. For each N, the energy reaches a minimum (which is zero for $N = 1$) as the system expands, followed by a rise to a second peak and subsequent smaller peaks towards a final value of nearly zero (not shown in the figure) as the system collapses back to its pre-tapped state. One also observes a shift in the location of the 2nd peak towards smaller times as N increases.

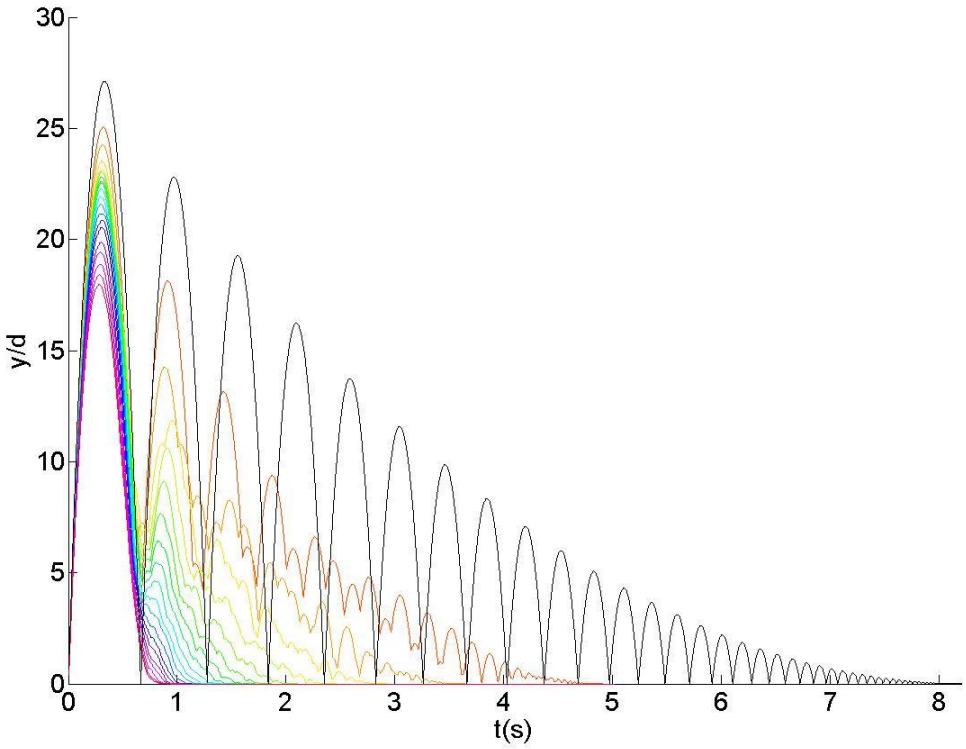

Figure 4.3 Evolution of mass center y/d. Colors signify different values of $N = 1, 2, 3, \ldots 20$. The black line is the result for a single sphere ($N = 1$).

Figure 4.5 shows the normalized total system energy ($TE/a^2\omega^2$), which is the sum of the kinetic ($\sim\sum_{i=1}^{N} v_i^2/2$) and potential energy ($\sum_{i=1}^{N} gy_i$). For each N, this quantity eventually asymptotes proportionally to $\sum_{i=1}^{N} gy_i(0)$ as the kinetic energy goes to zero.

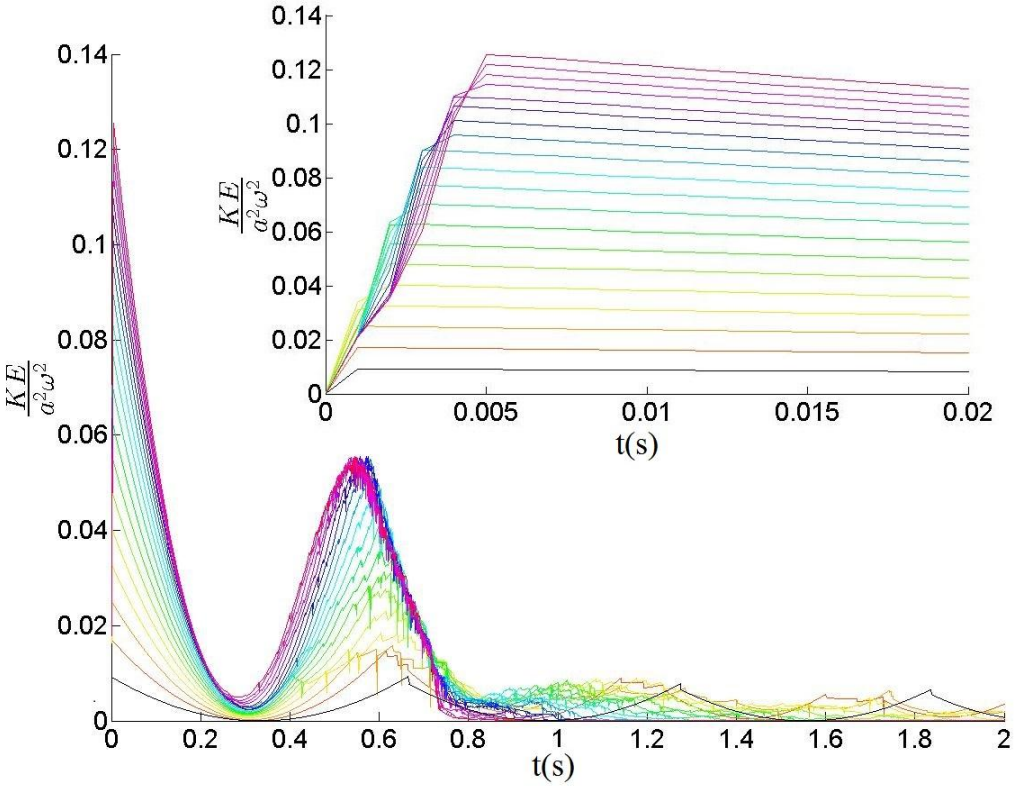

Figure 4.4 Normalized kinetic energy of the system. Line colors signify different values of N, while the black line is the result for a single sphere. The inset shows the evolution of the system kinetic energy near $t \cong 0$ at the initiation of the tap.

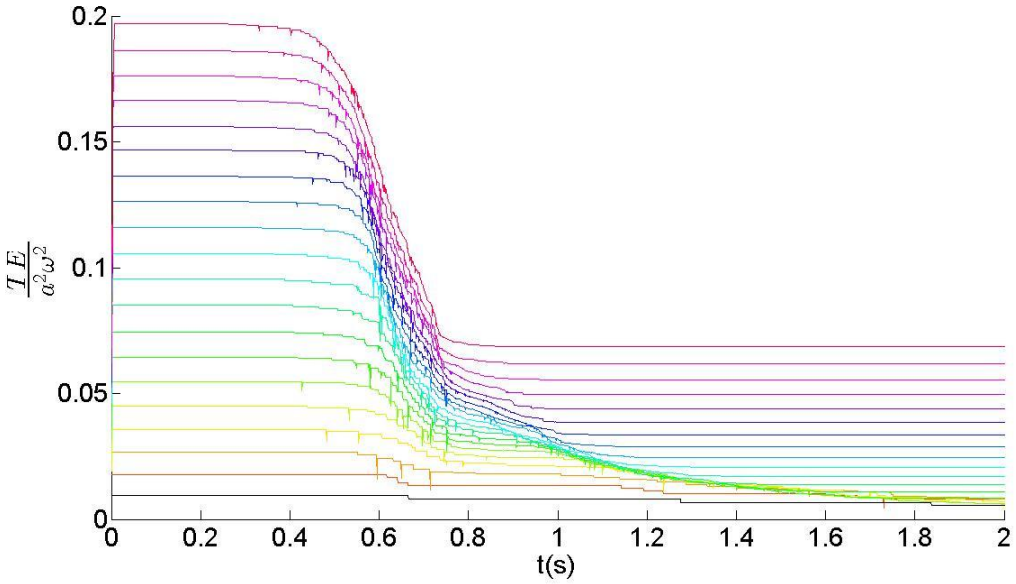

Figure 4.5 Normalized total energy (= kinetic + potential) evolution for $1 \leq N \leq 20$.

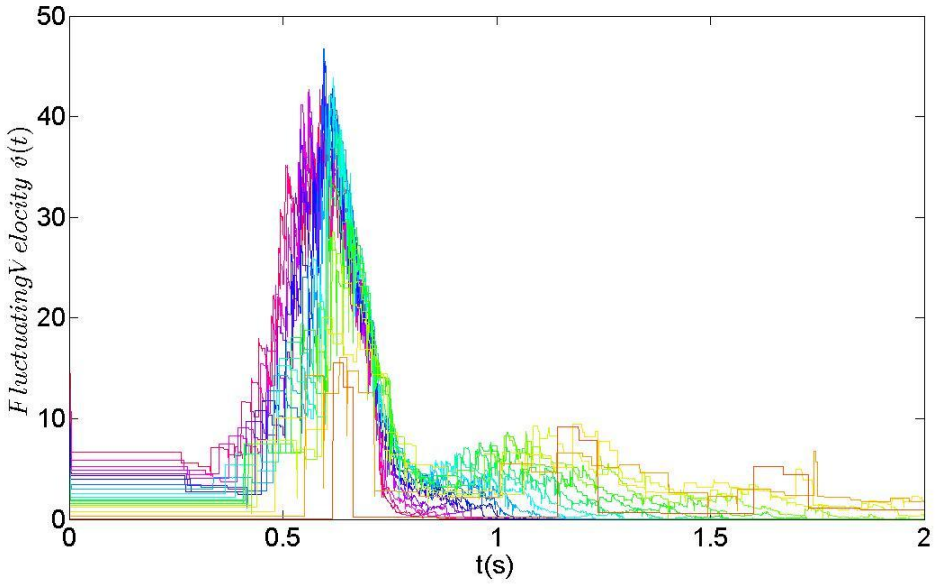

Figure 4.6 Evolution of fluctuating velocity given by (4.4)

Lastly, the evolution of fluctuating velocity as a function of the number of particles in the system is measured by computing the square of the deviation of the

velocities from the spatial mean $\bar{v}(t) := \frac{1}{N}\sum_{i=1}^{N} v_i^2(t)$. The fluctuating velocity evolution over the time interval of a tap and computed as

$$\acute{v}(t) = \sqrt{\frac{1}{N}\sum_{i=1}^{N}\left(v_i - \bar{v}(t)\right)^2} \qquad (4.4)$$

is shown in Figure 4.6 for $1 \leq N \leq 20$.

4.5 Stopping Time and Collision Frequency of the N-Ball System

The simulated findings Figures. 4.3 – 4.6 reflect that the stopping time t_s depends on the number of particles N in the system. The aim of this section is to determine a relationship between $t_s(N)$, with the expectation that it also varies with other important physical parameters, such as e, a/d and $f = \omega/2\pi$. So that unambiguous values of the stopping time can be extracted from the simulation data, an energy criterion is used. Accordingly, the value of $t_s(N)$ is defined as that time when the system kinetic energy first reaches $10^{-5}(KE_{max})$, and all subsequent values of the energy lie below this value. For example, Figure 4.7 is the kinetic energy evolution of a sphere released under gravity from $h/d = 20$, where the red horizontal line denotes where $KE/KE_{max} \leq 10^{-5}$.

The use of this criterion was assessed by extracting $t_s(1)$ at different KE/KE_{max} ratios in the drop test (i.e., single sphere released from $h/d = 20$). Results from this test recorded in Table 4.1 suggest that 10^{-5} is optimal. A further validation was conducted by determining the ratio KE/KE_{max} $(= 3.7 \times 10^{-6})$ via linear interpolation of the kinetic energy evolution data at $t_s(1) = t_{dr} = 6.8535\ s$. Then this ratio was used to extract the stopping time (denoted as $\hat{t}_s$) from the simulation data for system sizes $1 \leq N \leq 50$. The root-mean-square value of the difference $(\Delta t_s)_{rms} := \sqrt{\frac{1}{N}\sum_{k=1}^{N}[\hat{t}_s(k) - t_s(k)]^2} = 4.918 \times 10^{-7}$ along with the comparison of $\hat{t}_s$ and t_s displayed in Figure 4.8 indicates no

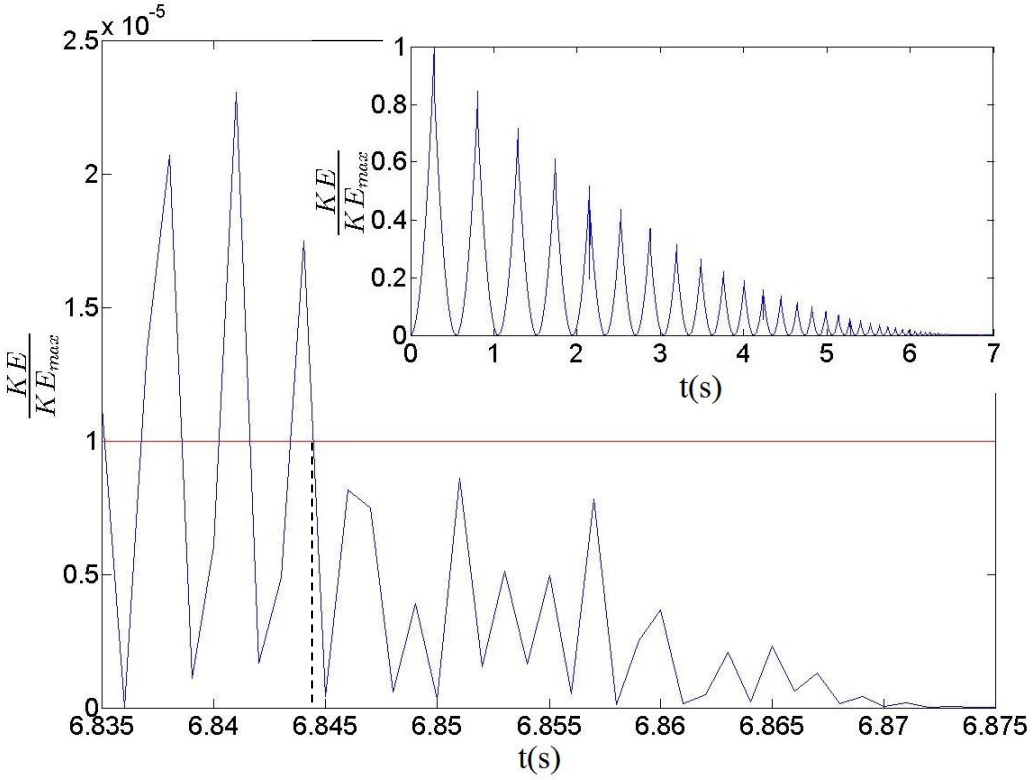

Figure 4.7 Kinetic energy evolution of a single sphere dropped from $h/d = 20$. The intersection of the horizontal red line and the dashed vertical line shows the time $t_s(1)$ when KE/KE_{max} remains $\leq 10^{-5}$. The inset shows the first 6 seconds of the process.

significant difference in the stopping time values. All subsequent reported results are for $(KE/KE_{max}) = 10^{-5}$.

Table 4.1 Single Sphere Stopping Time from Drop Test at Different Values of KE/KE_{max}

KE/KE_{max}	$t_s(1)$	$[t_s(1) - t_{dr}]/t_{dr}$
10^{-4}	6.7935	0.0088
10^{-5}	6.844	0.0014
10^{-6}	6.868	0.0021
10^{-7}	6.872	0.0027

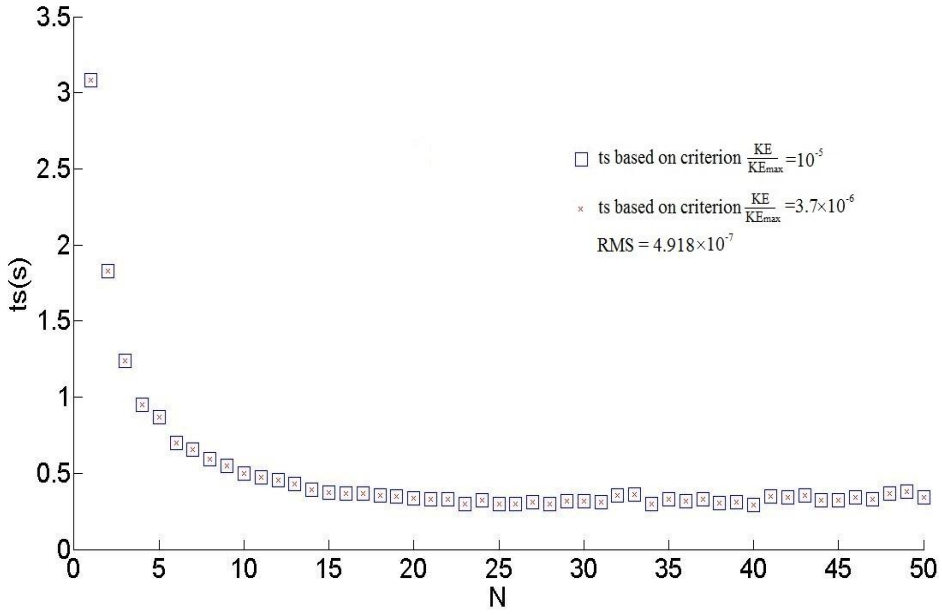

Figure 4.8 Absolute stopping time t_s for $(KE/KE_{max}) = 10^{-5}$ in seconds compared with $\hat{t}_s$ for $(KE/KE_{max}) = 3.7 \times 10^{-6}$ versus N.

Consistent with physical intuition, $t_s/t_s(1)$ decays with N, as shown in Figure 4.9 for the case $e = 0.92$, $f = 10\,Hz$, and $a/d = 0.5$, a behavior that was found to be typical for other values of e and a/d (See Figure 4.16 and 4.19). An increase in the number of particles is accompanied by a rise in the collision frequency, denoted as f_c and defined as the number of collisions per second. Larger collision frequencies result in a

faster rate of decrease of the system kinetic energy as reflected in a reduced stopping time.

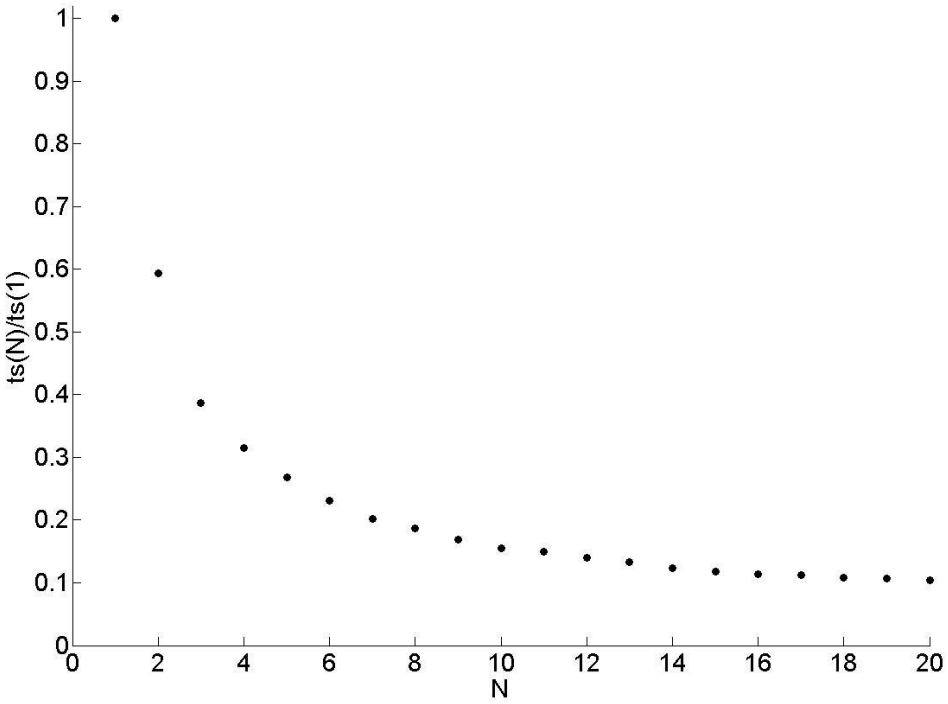

Figure 4.9 Normalized stopping time $t_s/t_s(1)$as a function of N, where $t_s(1)$ is the stopping time required for a single sphere.

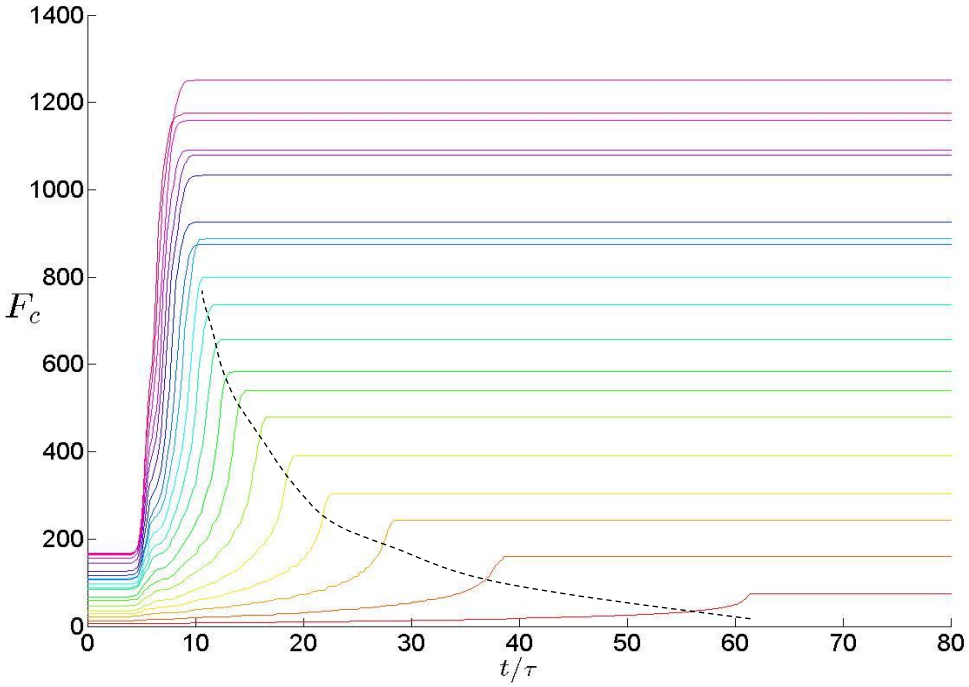

Figure 4.10 Evolution of the cumulative number of collisions $F_c(N)$ over the duration of a single tap ($a/d = 0.50$) as a function of t/τ. Each curve represents a different system size. The dashed line is added as an aid to identify the location of the plateaus in the data.

4.5.1 Collision Frequency

It is clear that f_c must depend on N and e, which is the subject matter of this section. A collision is counted when a particle overlaps with another, undergoes an interaction modeled by the linear loading/unloading springs (K_1, K_2) and then separates. For a single tap of each system of size N, the evolution of the cumulative number of collisions F_c is computed over the duration of the process from tap initiation to the end of the relaxation phase. After the system dilation phase has ended and the cooling process begins, F_c increases (at a rate that depends on N), and then saturates to a plateau, indicating that the column has reached a 'static' state. Figure 4.10 shows $F_c(t/\tau)$, where the different colors

represent N for $1 \leq N \leq 50$. The upper curve is for $N = 50$, while the lowest is for $N = 1$. From this data, two important quantities can be extracted. For each N, the stopping time $t_s(N)$ can be found at the location of the plateau, while the slope of the graph provides an approximation to the collision frequency f_c. The dashed line in the figure has been included to aid in the location of plateaus in the data.. Some important observations from the trends depicted in Figure 4.10 are warranted. As N increases, there is a clustering of the $F_c(N)$ curves, and for large N, the values of $t_s(N)$ derived from the data oscillates. It is hypothesized that these oscillations reflect the complex dynamics present in relatively large systems, where collisional interactions become more severe due to the greater effect of an increased mass overburden. Moreover, the influence of initial conditions (i.e., momentum of the spheres and the inter-particle forces) as the system size grows may also have a bearing on the ensuing dynamics, akin to sensitive dependence on initial condition characteristic of chaotic behavior.

In addition to extracting the average collision frequency- dividing the final total number of collisions by the time required to reach this value (see Figure 4.10) - the number of collisions C is also computed every 0.01 seconds and plotted as a function of time. The result of this computation for $N = 20$ is displayed in Figure 4.11. The motion of the floor representing the tap triggers a wave that moves up through the column, followed by a dilation in which sphere contacts are broken. This can be seen in the figure immediately after the first small peak $t/\tau \cong 2$. Subsequently, as the spheres begin their descent in the cooling phase, collisions are prevalent as evidenced in the figure from $t/\tau \cong 35$ to $t/\tau \cong 50$.

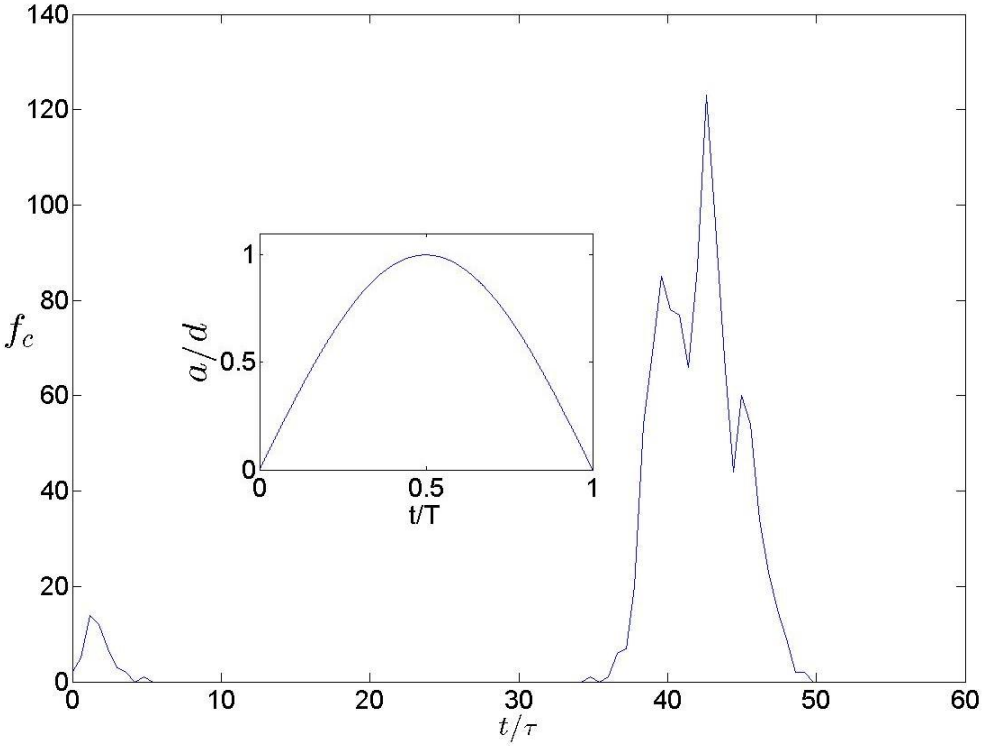

Figure 4.11 Collision frequency f_c (collisions / second) as a function of time for a 20 particle column. The cooling phase begins at $t/\tau \cong 35$. The inset shows the motion of the floor.

Figure 4.12 shows f_c versus t/τ, where the inset is the result for a single sphere and the colors represent columns of different size ($1 \leq N \leq 20$). The spread of the data simply reflects the variation of f_c with N. It is possible now to compute a mean collision frequency $\bar{f}_c$ by numerical integration, i.e., Simpson's rule $\bar{f}_c^{(s)}$,

$$\bar{f}_c^{(s)} = \frac{1}{3M}\left[(C)_1 + 2\sum_{k=1}^{\frac{M}{2}-1}(C)_{2k} + 4\sum_{k=1}^{\frac{M}{2}}(C)_{2k-1} + (C)_M\right] \qquad (4.5.1)$$

or trapezoidal integration $\bar{f}_c^{(tr)}$,

$$\bar{f}_c^{(tr)} = \frac{1}{M}\sum_{i=1}^{M} C_i \qquad (4.5.2)$$

where C_i is the number of collisions that occur in a 0.01s time interval, and M is the number of intervals spanning the data set.

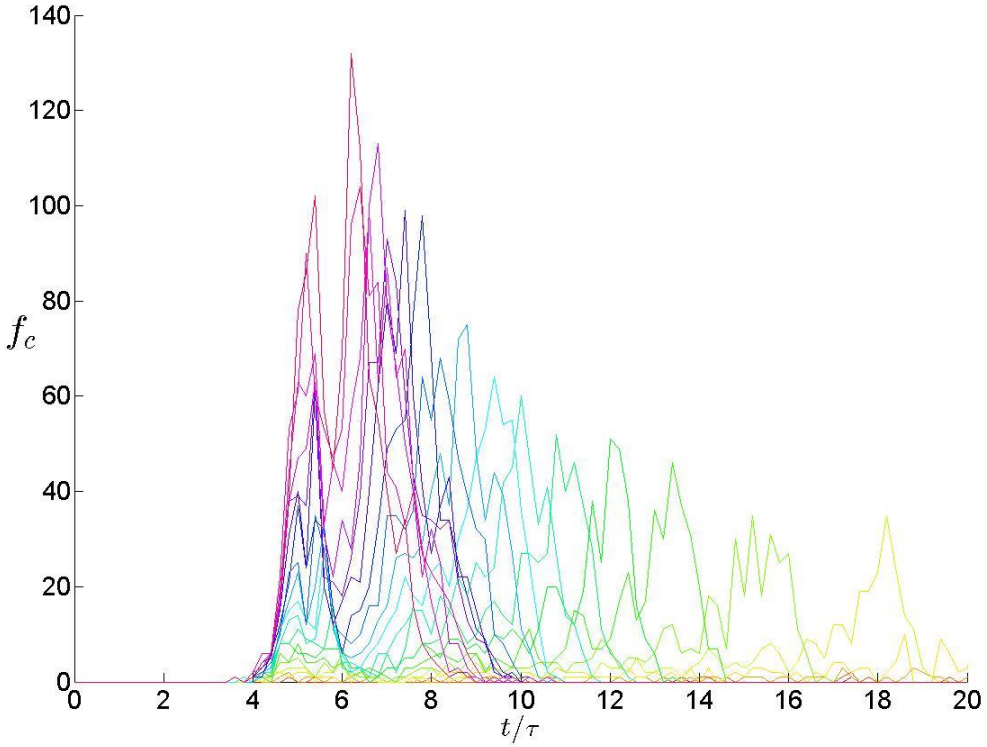

Figure 4.12 f_c versus t/T, where the colors represent column sizes $1 \leq N \leq 20$

The result of the calculations displayed in Figure 4.13 indicates fairly good agreement between the three averaging methods, albeit some slight differences for larger values of N exist. A linear fit to the data obtained from Simpson's method (4.5.1) with $R^2 = 0.9815$ suggests that $\bar{f}_c$ scales directly with N for $1 \leq N \leq 50$.

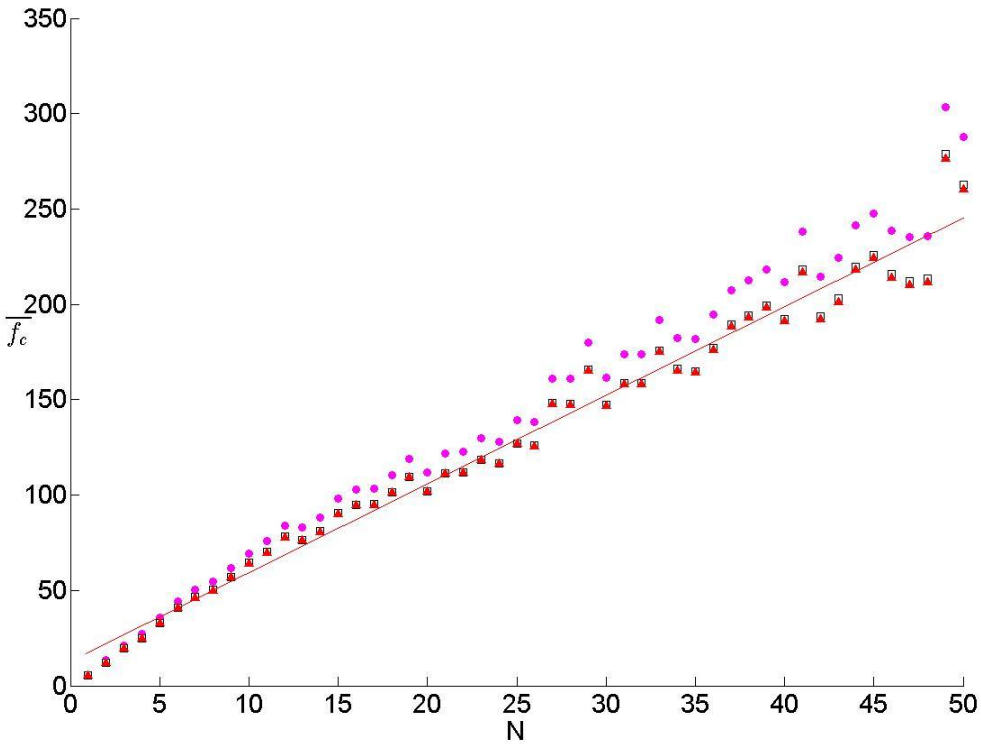

Figure 4.13 Average collision frequency $\bar{f}_c$ versus system size N: ●correspond to $\bar{f}_c^{(a)}$; ▲ Trapezoidal integration; □ corresponds to $\bar{f}_c^{(s)}$. The straight line is the fit to the data obtained from Simpson's rule (4.5.2).

4.5.2 Heuristic Considerations: Stopping Time Versus System Size

A heuristic model of the behavior just described is developed by expressing the rate of energy loss as the product of the collision frequency and the energy lost in a single collision, i.e.,

$$\frac{d}{dt}(KE) = f_c(t)\Delta KE_{(1)} \tag{4.6}$$

where $\Delta KE_{(1)} = (e^2 - 1)KE_0$, and KE_0 is the initial kinetic energy. A rearrangement of the latter relation leads to

$$d(KE) = (e^2 - 1)f_c(t)KE_0 dt < 0. \tag{4.7}$$

Upon setting $\mathcal{E} := KE/KE_0$, and noting that $\mathcal{E}|_{t=0} = 1$, $\mathcal{E}|_{t=t_s(N)} = 0$,

$$\int_1^0 d\mathcal{E} = (e^2 - 1)\int_0^{t_s} f_c\left(N, e, \frac{a}{d}, \omega; t\right) dt \qquad (4.8)$$

where the terms in the parenthesis indicate the dependency of $\bar{f}_c$ on N, e, a/d and ω. If all of these parameters are considered constant except for N, then

$$\frac{1}{1-e^2} = \int_0^{t_s} f_c(N;t)dt = \bar{f}_c(N)t_s\,. \qquad (4.9)$$

In the latter relation, it has been assumed that the integral can be approximated by the mean collision frequency $\bar{f}_c$, which depends on N as seen in the simulation results of Figure 4.13. Therefore, one might expect a scaling of the form,

$$t_s(N) \sim \frac{1}{(1-e^2)\bar{f}_c} \qquad (4.10)$$

If the linear scaling suggested by Figure 4.2 is substituted in (4.10),

$$t_s(N) = \frac{1}{1-e^2}(a_1 N + a_2)^{-1} \sim \frac{\alpha}{N} + \beta \qquad (4.11)$$

Naturally, the coefficients α and β in (4.11) must depend on the restitution coefficient in such a way that a reduction of e will result in a shorter stopping time.

A fit of the data $t_s(N)/t_s(1)$ to equation (4.11) for $1 \leq N \leq 20$ is presented as the solid line in Figure 4.14 for which $R^2 = 0.9952$ suggests a good correlation. The solid lines in Figure 4.14 are fits to equation (4.11) normalized by $t_s(1)$ for $1 \leq N \leq 50$ ($e = 0.92$), while Table. 4.2 tabulates the corresponding values (α, β) and correlation coefficients. In Figure 4.15, the fluctuations in $t_s(N)/t_s(1)$ that appear as N increases beyond 20 (R^2 for $N = 50$ was somewhat smaller as compared with $N = 20$) may be a consequence of progressively complex system dynamics.

It is noted that least-square fits to the form $(\alpha N^{-\gamma} + \beta)$ yielded values of γ very close to unity, as seen in Table 4.3, which lists fitted values of α, β, and γ, their 95% confidence intervals, and R^2 for $0.91 \leq e \leq 0.99$ and $N = 50$.

Table 4.2 Correlation Coefficients of Fits of the Normalized Stopping Time $t_s(N)/t_s(1)$ Data to $(\alpha N^{-1} + \beta)$ for $a/d = 0.25, 0.50, 1.0, 1.25, 1.50$ at $f = 10Hz$, and $e = 0.92$. (See Figures. 4.14, 4.15 and 4.16).

$e = 0.92$	N	α	α_{ci}	β	β_{ci}	R^2
$a/d = 0.25$	$1 \leq N \leq 20$	1.427	1.372 - 1.482	0.1418	0.126 - 0.157	0.9936
	$1 \leq N \leq 50$	1.31	1.216 - 1.404	0.1981	0.181 - 0.215	0.941
$a/d = 0.5$	$1 \leq N \leq 20$	2.965	2.865 - 3.064	0.2101	0.182 - 0.238	0.9952
	$1 \leq N \leq 50$	2.919	2.841 - 2.997	0.2303	0.216 - 0.244	0.9914
$a/d = 1$	$1 \leq N \leq 20$	5.918	5.764 - 6.073	0.4187	0.391 - 0.447	0.9919
	$1 \leq N \leq 50$	5.93	5.684 – 6.176	0.4168	0.347 - 0.486	0.993
$a/d = 1.25$	$1 \leq N \leq 20$	7.486	7.131, 7.841	0.508	0.408, 0.608	0.9904
	$1 \leq N \leq 50$	7.49	7.287, 7.692	0.5022	0.466, 0.539	0.9912
$a/d = 1.5$	$1 \leq N \leq 20$	8.962	8.541, 9.383	0.6173	0.498, 0.736	0.9906
	$1 \leq N \leq 50$	8.987	8.754, 9.221	0.6008	0.559, 0.643	0.9919

Table 4.3 Fit Values of α, β, γ in (4.11) and Confidence Intervals α_{ci}, β_{ci} and γ_{ci} for $0.91 \leq e \leq 0.99$, $a/d = 0.50$, and $N = 50$. Figure 4.19 Shows t_s vs. N for $\gamma = 1$.

e	α	α_{ci}	γ	γ_{ci}	β	β_{ci}	R^2
0.91	2.533	2.423 - 2.643	1.037	0.995 - 1.079	0.2587	0.239 - 0.278	0.9781
0.92	2.908	2.826 - 2.989	0.983	0.960- 1.007	0.2237	0.209 - 0.239	0.9908
0.93	3.413	3.312 - 3.514	0.938	0.884 - 0.993	0.1951	0.159 - 0.232	0.9875
0.94	4.099	3.977 - 4.220	1.014	0.972 - 1.047	0.2417	0.220- 0.263	0.9895
0.95	4.942	4.808 - 5.075	0.985	0.949 - 0.993	0.2203	0.196 - 0.245	0.9913
0.96	6.446	6.229 - 6.662	1.007	0.967 - 1.036	0.2442	0.205 - 0.283	0.9868
0.97	8.501	8.327 - 8.675	0.957	0.945 - 0.976	0.1967	0.165 - 0.229	0.9951
0.98	13.15	12.73 - 13.56	1.008	0.983 - 1.032	0.3296	0.255 - 0.404	0.9883
0.99	26.68	25.92 - 27.44	0.964	0.944 - 0.985	0.3598	0.221 - 0.499	0.9905

A further series of studies was conducted at four other displacement amplitudes $(a/d = 0.25,\ 0.50, 1.0, 1.25, 1.50)$ at $e = 0.92$, and the data was fit to the form given by (4.11) for $1 \leq N \leq 20$. The symbols on Figure 4.16 are the values of t_s (sec.) while the solid lines are the fitted curves. Note that the normalization constant was selected to be the time required for a single ball tapped at $a/d = 1$ to come to rest. Except for the case

$a/d = 0.25$ and $1 \leq N \leq 50$, R^2 values were all larger than 0.98, suggesting a strong correlation of the data with (4.11).

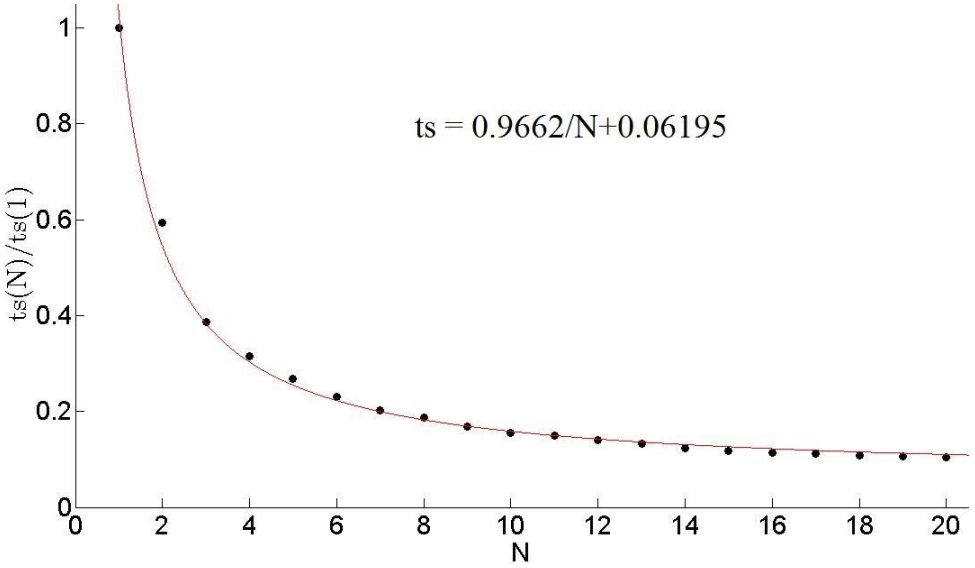

Figure 4.14 Normalized stopping time $t_s(N)/t_s(1)$ versus system size N, where $t_s(1) = 3.086\ s,\ e = 0.92, a/d = 0.50.$

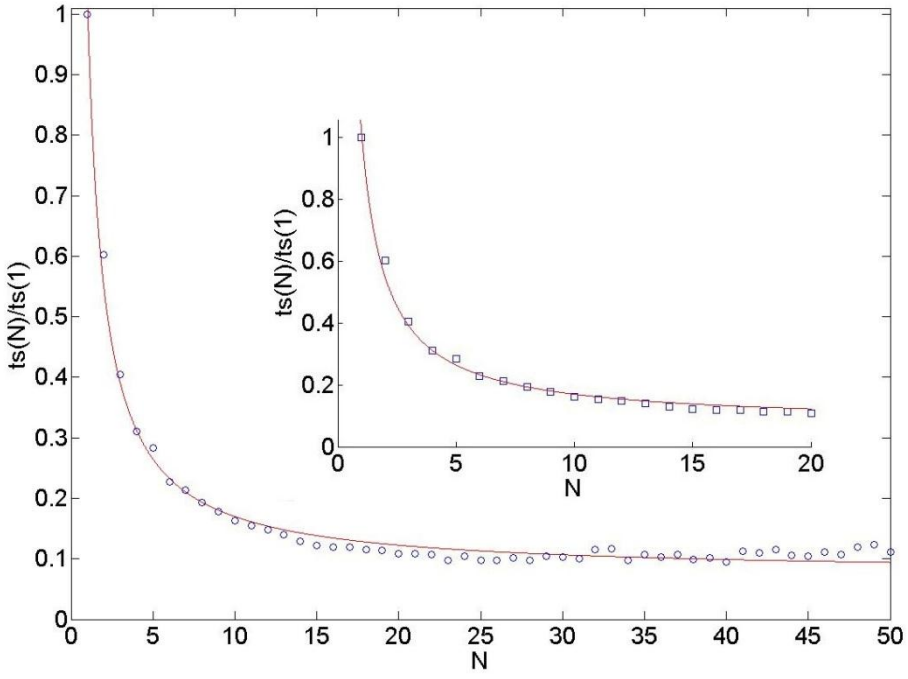

Figure 4.15 Normalized stopping time $t_s(N)/t_s(1)$ versus N for $1 \leq N \leq 50$, $a/d = 0.50$ and $e = 0.92$. The inset shows the result for $1 \leq N \leq 20$. Solid lines are the fitted curve from (4.11)

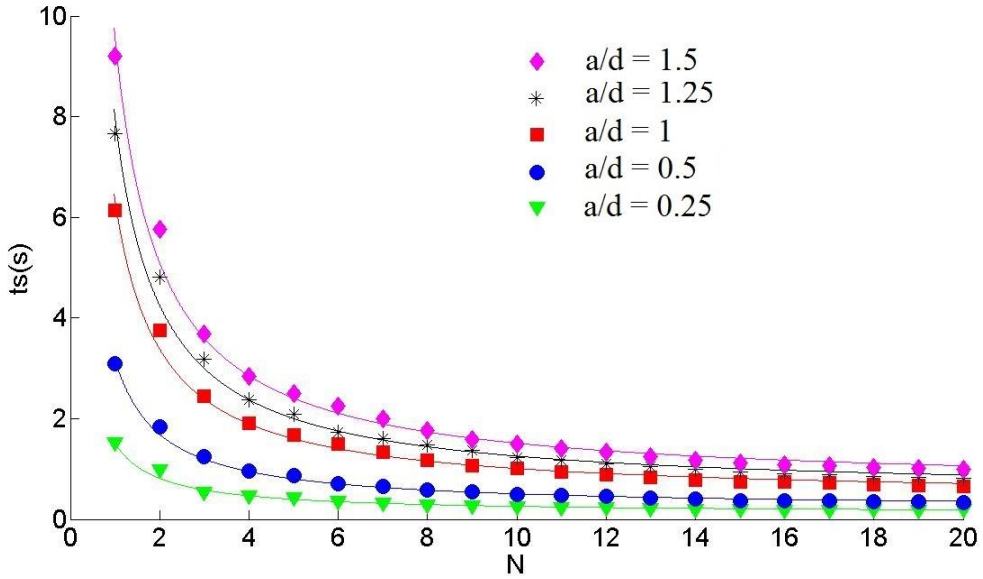

Figure 4.16 Absolute stopping time t_s versus N ($e = 0.92$, $f = 10\,Hz$) for $a/d = 0.25, 0.50, 1.0, 1.25, 1.50$. The solid lines are fits to $t_s = \alpha N^{-1} + \beta$ (equation (4.11)), for which the fit parameters are listed in Table 4.2.

4.5.3 Stopping Time Versus Restitution Coefficient

If the coefficient of restitution decreases so that more energy is dissipated in a collision, there will be a reduction in the collision frequency (assuming that N, a/d and ω are fixed). In order to substantiate this expected behavior, a study was done in which e was varied ($0.04 \leq e \leq 0.99$) for $N = 20$, $f = 10\,Hz$, and $a/d = 1.0$. The possibility of there being an exponential relationship between $\bar{f}_c$ and e for fixed N, a/d and ω is tested by plotting $\log(\bar{f}_c)$ versus e. The result shown in Figure 4.17 suggests a moderate correlation for $e < 0.9$.Therefore, the mean collision frequency data ($\bar{f}_c$), computed via the method detailed in Section 4.5.1, was fit to an exponential of the form,

$$\bar{f}_c = A_1 exp(A_2 e) + A_3, \qquad (4.12)$$

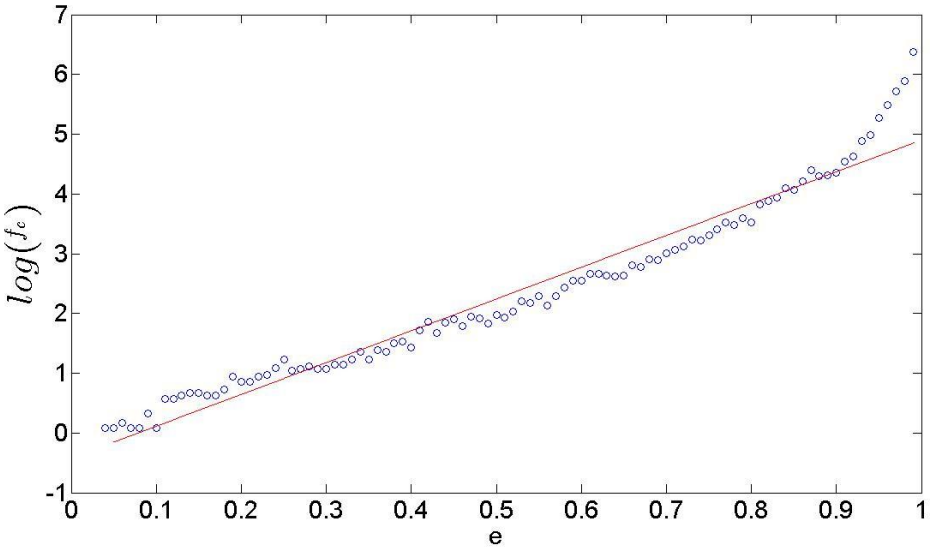

Figure 4.17a Log of $\bar{f}_c$ versus restitution coefficient e.

for five different tap amplitudes, $a/d = 0.25, 0.50, 1.0, 1.25$ 1.5. The symbols in Figure 4.18 are the simulation data and the lines are fits to (4.12). Fit parameters are listed in Table 4.4, where the R^2 values and overlapping 95% confidence intervals of the coefficients suggest weak correlation with (4.13). The fact that there is no clear separation of the data with a/d indicates that $\bar{f}_c$ may not be strongly dependent on a/d.

Table 4.4 Fit Parameters for $\bar{f}_c = A_1 exp(A_2 e) + A_3$ (Equation 4.12 and Figure 4.18)

a/d	$A_1 \times 10^{-8}$	$A_{1ci} \times 10^{-8}$	A_2	A_{2ci}	A_3	A_{3ci}	R^2
0.25	1.17	-1.536, 3.876	24.63	22.26, 27.00	9.01	5.365, 12.66	0.947
0.5	7.607	-5.865, 21.08	22.84	21.02, 24.65	10.62	7.183, 14.06	0.963
1.0	2.715	-2.392, 7.821	24.16	22.23, 26.09	12.77	8.341, 17.21	0.964
1.25	19.46	-16.59, 55.52	22.08	20.18, 23.98	12.48	7.892, 17.06	0.957
1.5	23.48	-18.49, 65.45	21.93	20.1, 23.76	13.09	8.46, 17.72	0.960

A plot of $\log(t_s)$ versus e shown in Figure 4.17b suggests a fairly good correlation so that an exponential behavior of the stopping time with e is reasonable, except at $e = 1$, where physical intuition dictates that t_s should diverge. The $(1 - e^2)^{-1}$ term in equation (4.10) captures this behavior. Under the assumption that e varies and all other parameters are fixed, a substitution of (4.12) into (4.10) gives,

$$ts = \frac{1}{(A_1 exp(A_2 e) + A_3)(1 - e^2)} \tag{4.13}$$

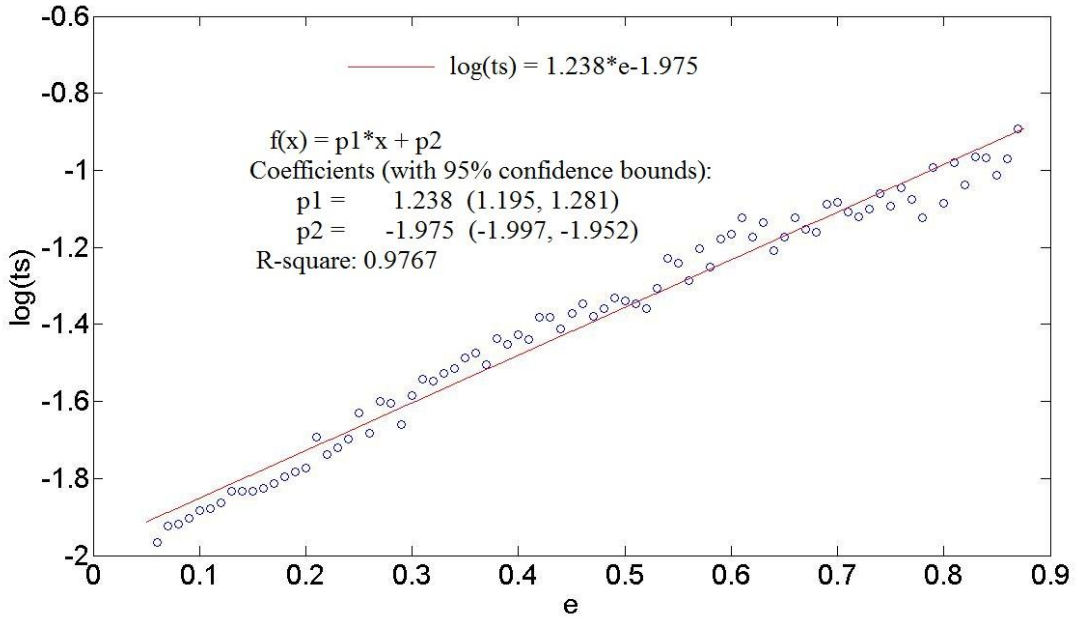

Figure 4.17b $log(t_s)$ vs. e. The data (○) is well-correlated to $log(t_s) = ae + b$, with $a = 1.238, b = -1.975$, $R^2 = 0.9767$, shown by the straight line.

Fits of the data to (4.13) are shown in Figure 4.19 as the solid lines, where the symbols are the data for $a/d = 0.25, 0.50, 0.75, 1.0\ 1.25$. Table 4.5 lists the fit parameters A_1, A_2, A_3, their 95% confidence intervals and R^2 values. One sees a clearer separation of the curves with a/d, that is, as a/d increases, more time is needed for the system to relax.

Table 4.5 Fit Parameters for$t_s = [(A_1 exp(A_2 e) + A_3)(1 - e^2)]^{-1}$(Equation (4.13) and Figure 4.19)

a/d	$A_1 \times 10^{-6}$	$A_{1ci} \times 10^{-6}$	A_2	A_{2ci}	A_3	A_{3ci}	R^2
0.25	40.28	3.573, 76.98	13.97	13.04, 14.9	9.558	9.23, 9.886	0.9655
0.5	474.8	166.6, 783.0	10.87	10.2, 11.53	5.224	5.052, 5.397	0.9737
1.0	1265.	425.1, 2105	9.157	8.48, 9.835	2.886	2.769, 3.002	0.9811
1.25	1597.	863.3, 2331	8.694	8.226, 9.162	2.358	2.288, 2.427	0.9576
1.5	1736.	977.6, 2495	8.417	7.972, 8.862	2.031	1.973, 2.09	0.9854

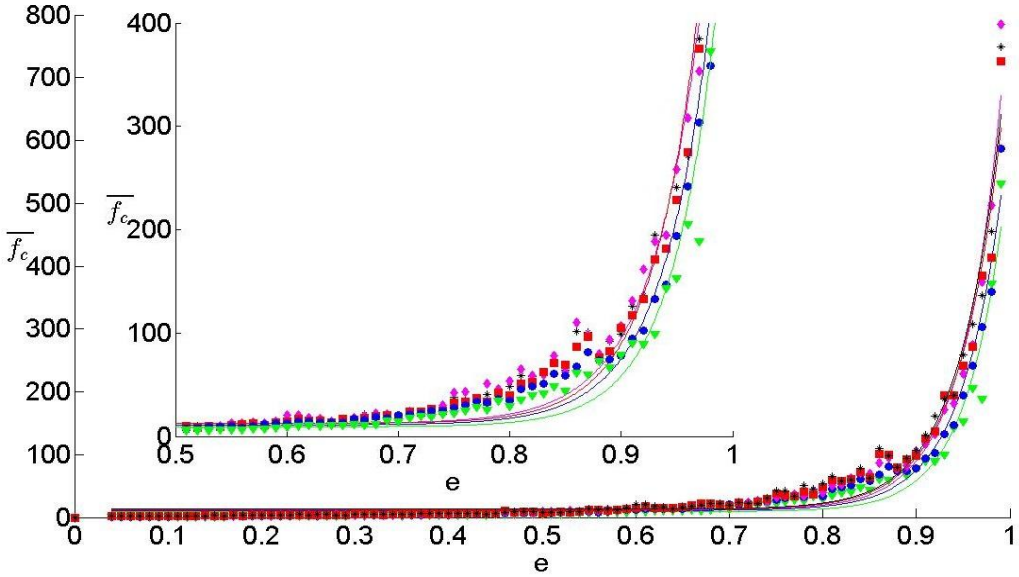

Figure 4.18 $(\bar{f}_c)$ vs. e for $N = 20$ and $f = 10\ Hz$. Open symbols are the data and the lines are fits to (4.12), for which parameters are listed in Table 4.4. ▼$a/d = 0.25$; ●$a/d = 0.50$; ■$a/d = 1.0$; ∗$a/d = 1.25$; ◆$a/d = 1.50$. The inset shows a reduced range of the data.

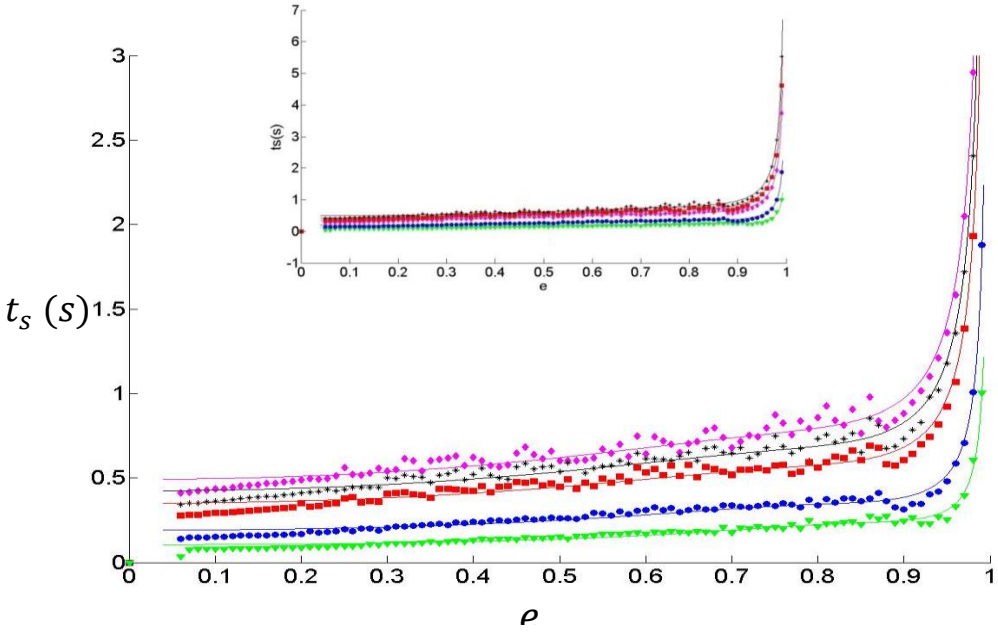

Figure 4.19 t_s (s) vs. e for $N = 20$, $f = 10\ Hz$. Solid lines are fits to (4.13). ▼$a/d = 0.25$; ●$a/d = 0.50$; ■$a/d = 1.0$; ∗$a/d = 1.25$; ◆$a/d = 1.50$. The inset shows the full range of data.

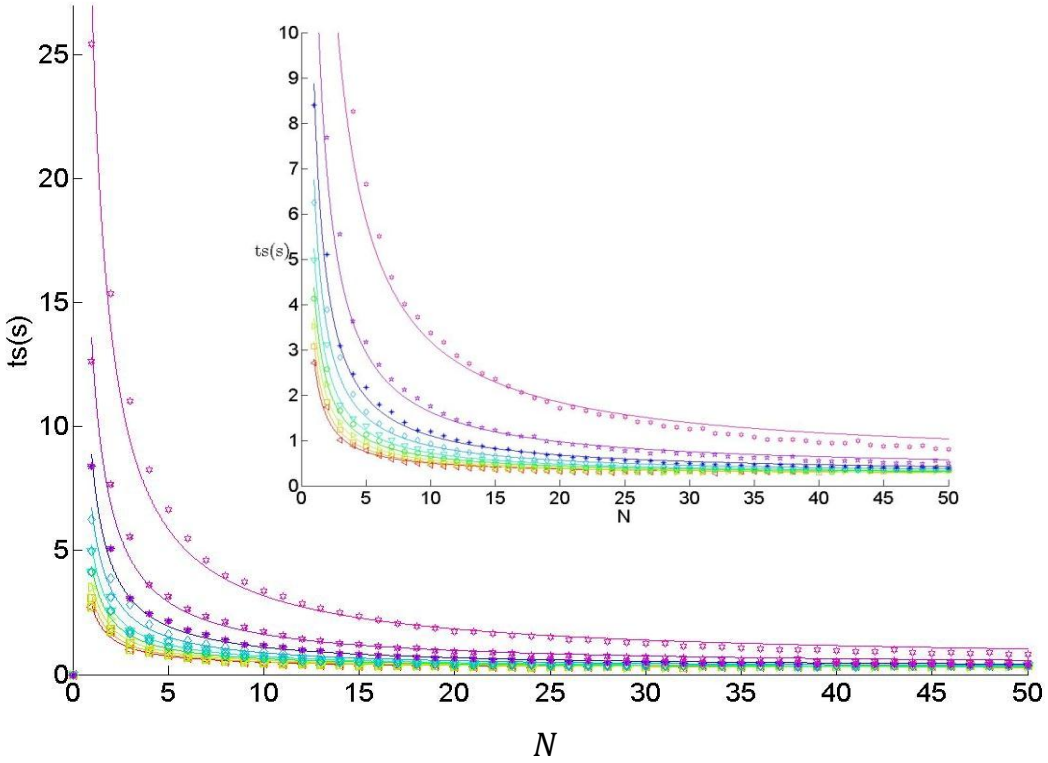

Figure 4.20 Stopping time as a function of N for different restitution coefficients $0.91 \leq e \leq 0.99$ at $a/d = 0.50$). Solid lines are fits to equation (4.11), i.e., $t_s = \alpha N^{-1} + \beta$. The inset is the same plot for a restricted range of stopping times.

The variation of t_s with N for $(0.91 \leq e \leq 0.99)$ is shown in Figure 4.20, where again the data is well-correlated with (4.13). The inset is the result for $t_s(N)/t_s(1)$.

CHAPTER 5

EXPANSION DYNAMICS OF GRANULAR COLUMN

In this chapter, an attempt is made to map the dependence of the evolution of the total kinetic energy on the parameter set a/d, f, N, e, and to connect this with system's general behavior as regards its dilation and collapse. During the course of the study, various physical measures of the column's dilation or expansion are used. For a single ball, a tap applied to the floor on which it rests causes the ball to move upwards, the height of which depends on the tap energy and the mass of the ball. But if there are several spheres placed on top of each other so as to create a column, energy will be distributed to each particle in some manner. If the tap energy is sufficient, the system density will evolve to a minimum value corresponding to the maximum dilation of the column. Even if the tap energy is not sufficient to break the column apart, there will always be an impulse wave transmitted through the column. This occurs over a short time scale $dt \sim N\sqrt{\rho\pi d^3/12K_1}$, as per the contact model, where N is the number of particles each of mass m and K_1 is the contact loading stiffness. For the value of K_1 ($= 2.8 \times 10^5\ N/m$) and ρ($= 1200\ kg/m^3$) used in this dissertation, $dt \sim 9.47 \times 10^{-5} N$. In this chapter, an attempt is made to map the dependence of the evolution of the total kinetic energy on a/d, f, N,and e, and to connect this with system's general behavior as regards its dilation and collapse.

5.1 Problem Description

Consider the situation where the particles of the column are just touching each other with

no active overlaps, which would be the situation in the presence of gravity. Then, as the floor begins to move upwards, the overlap between it and the first sphere (sitting on top of the floor) begins to increase so that after one integration time step, that particle begins to intersect (or overlap) at the contact point with its upper neighbor. This process continues upwards through the column until integration of the top particle's equation is initiated. The latter illustration reflects in a simple manner the explicit Verlet leap-frog time integration scheme featured in the DEM code. If the condition $a\omega^2/g \gtrsim 1$ is

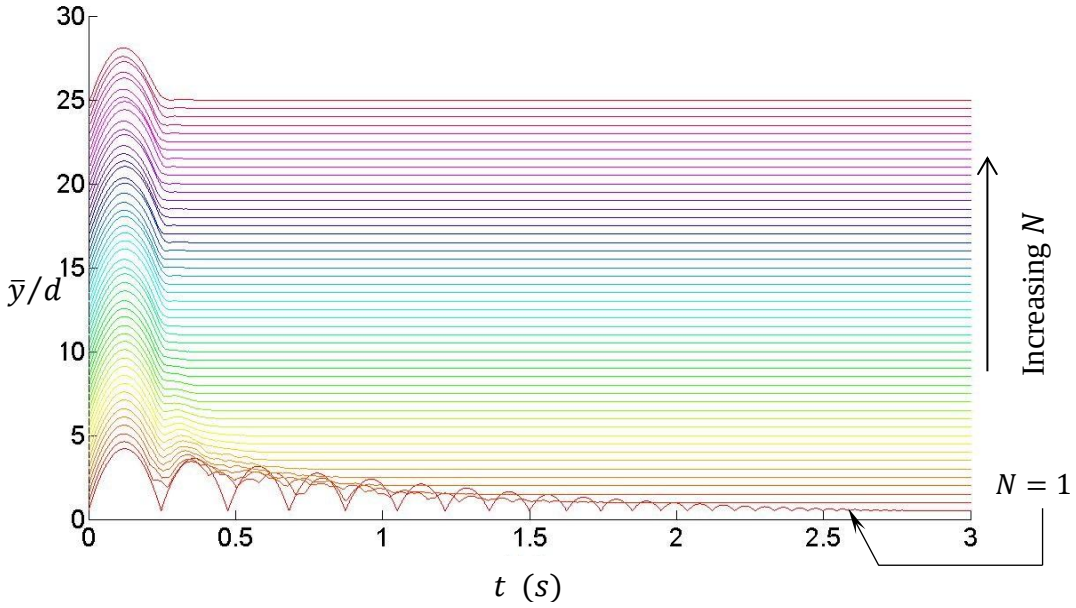

Figure 5.1 Evolution of the mass center as a result of a single tap ($a/d = 0.5, f = 10\ Hz$) applied to the column for varying system sizes $1 \leq N \leq 50$.

satisfied, contacts between some of the adjacent particles will break as the floor separates from the first particle in its downward stroke. Consequently, the amplitude a/d and frequency ω play a critical role in the system dynamics, as well as N and e. The subsequent sections present the results of an exploratory study of the effects of these parameters on the system.

5.2 Dependence of the Column Expansion on System Size

The dynamic behavior of the column is strongly dependent on the number of particles. One expects that as N increases under fixed tap conditions (a/d, and f), eventually the input energy will not be sufficient to promote any significant dilation[4] (if any at all) of the system. A measure of the behavior of the system is provided by the evolution of its mass center trajectory $\bar{y}/d\ (t)$, which is shown in Figure 5.1 for a single tap ($a/d = 0.5, f = 10\ Hz,\ e = 0.90$) as a function of the number of particles, $1 \leq N \leq 50$. The damping of the oscillations with increasing N reflects greater energy dissipation as a result of

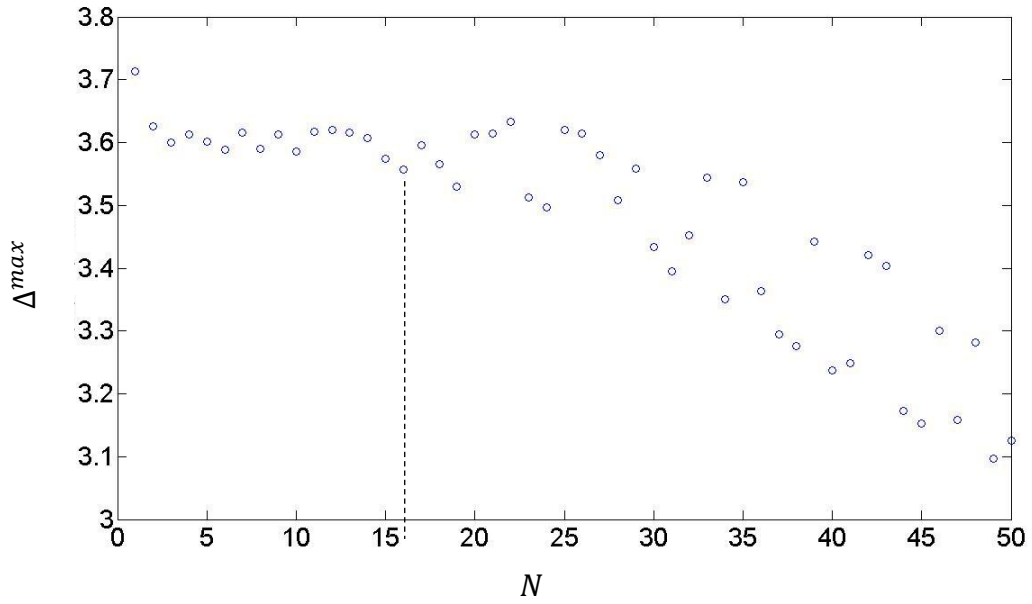

Figure 5.2 Graph of Δ^{max} as a function of N for tap parameters $a/d = 0.5, f = 15\ Hz$, and $e = 0.90$. The horizontal dashed line demarcates the value of $N = 16$ when significant fluctuations appear.

larger collision frequencies. In fact, for $N \gtrsim 15$, the second peak of the $\bar{y}/d\ (t)$ disappears. A somewhat clearer picture of the effect of N emerges in Figure 5.2 - the

4 Loss of contacts between particles

graph of the maximum value of $\bar{y}/d\ (t)$ relative to $\bar{y}/d\ (0)$ versus N, given by

$$\Delta^{max}(N) = \underbrace{max}_{t\geq 0}\left\{\frac{\bar{y}}{d}(t) - \frac{\bar{y}}{d}(0)\right\}. \qquad (5.1)$$

There is a decreasing trend of $\Delta^{max}(N)$ with N as would be expected since the fixed input energy of the tap becomes less effective - a consequence of greater collisional dissipation for larger N. One also observes fluctuations in Δ^{max} grow with N, and they become significant (and physically improbable) for $N \geq 16$, as indicated by the vertical

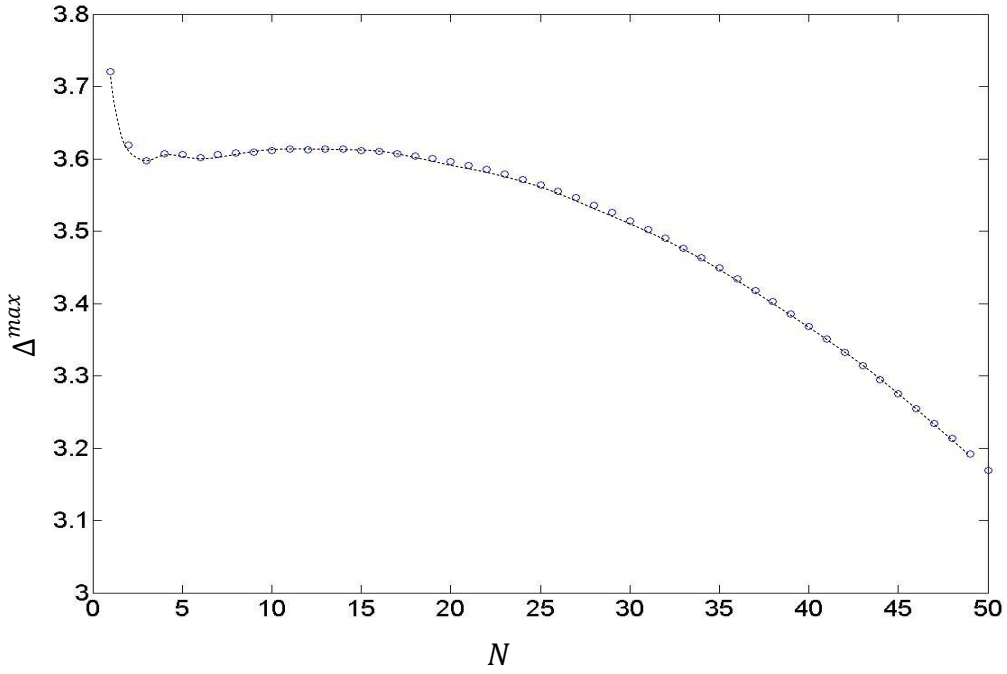

Figure 5.3 Graph of Δ^{max} as a function of N for tap parameters $a/d = 0.5, f = 15\ Hz$, and $e = 0.90$. Each of the $N = 50$ systems had the same initial conditions, i.e., $\{\boldsymbol{y}(0), \boldsymbol{v}(0)\} = \{\mathbf{0}, \mathbf{0}\}$. The dotted line shows the trend of the data.

dashed line. The reason for these fluctuations (explained in what follows) is connected with the dynamic state of the system when the tap is initiated.

The fluctuations originate from differences (consequent on the value of N) in dynamic initial conditions, or equivalently, the point in phase space of dimension $2N$(i.e.,

particle positions $\boldsymbol{y} \in \mathbb{R}^{\boldsymbol{N}}$ and velocities $\boldsymbol{v} \in \mathbb{R}^{\boldsymbol{N}}$) of the system when the tap is initiated. As further explication, consider a column of N spheres whose initial placement is such that the particles are just touching each other. When the simulation begins, gravity acts on each particle, causing it to overlap with its neighbors thus activating the linear springs (loading stiffnessK_1; unloading stiffnessK_2) between them. Consequently, there will be small oscillations of the spheres until eventually (say at $t = t_\infty$) the assembly attains a state of dynamic equilibrium. That is,

$$\forall\, t \geq t_\infty, \big(\boldsymbol{y}(t), \boldsymbol{v}(t)\big) \subseteq \mathcal{B}_{\boldsymbol{\varepsilon(N)}} := \{(\boldsymbol{y}, \boldsymbol{v}) \in \mathbb{R}^{2\mathrm{N}} \,|\, \|(\boldsymbol{y}, \boldsymbol{v}) - (\boldsymbol{y}_\mathrm{o}, \boldsymbol{v}_\mathrm{o})\| < \varepsilon(N)\} \quad (5.3)$$

where $\big(\boldsymbol{y}(t), \boldsymbol{v}(t)\big) := (y_1, y_2, y_3, \cdots y_N, v_1, v_2, \cdots, v_N)$. For the results depicted in Figure 5.2, the tap (i.e., floor begins to move) is initiated at $t = 10\,s$ at which time it is presumed that $\big(\boldsymbol{y}(10), \boldsymbol{v}(10)\big) \in \mathcal{B}_{\boldsymbol{\varepsilon(N)}}$. Because the system size is varied in generating Figure 5.2, each column of size N will occupy a different point of the system phase space (size $2N$) so that the particle positions and velocities will not be the same when the tap is initiated. In order to test the conjecture that the fluctuations seen in Figure 5.2 are due to the initial conditions, a series of simulations were done for which the initial state (at $t = 0$) was such that particles were simply placed on top of each other (just touching). In this way, each system of size N was static so that $(\boldsymbol{y}, \boldsymbol{v})_{t=0} := \{\boldsymbol{0}, \boldsymbol{0}\}$. A simulation begins by moving the floor simultaneously with gravity operating on the particles. The result of this simulation series depicted in Figure 5.3 confirms that the fluctuations seen in Figure 5.2 disappear.

An equivalent characterization of the effect of N is given by the graph of the maximum free space ϕ^{max} in Figure 5.4, defined as,

$$\phi^{max} := \underbrace{max}_{t\geq 0}\left\{\frac{y_N(t) - y_o(t) - \left(N - \frac{1}{2}\right)d}{d}\right\}. \qquad (5.2)$$

One observes a peak in ϕ^{max} followed by a decreasing trend with fluctuations growing with N. These fluctuations are caused by differences in initial conditions as was

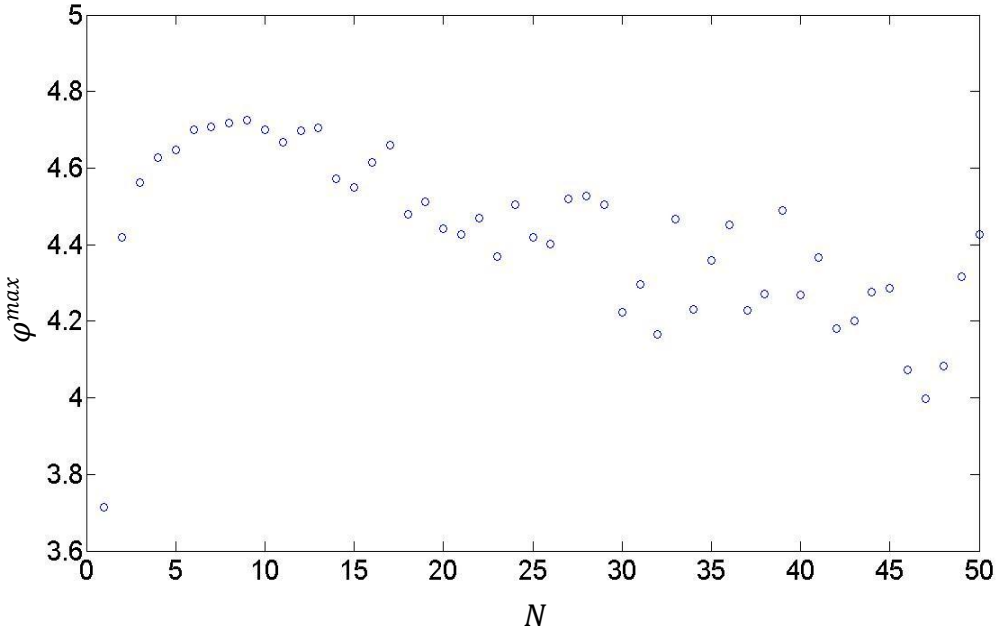

Figure 5.4 Graph of φ^{max} versus N for $a/d = 0.5, f = 15\ Hz$, and $e = 0.90$.

the case for Δ^{max} (see Figure 5.2). For the same initial conditions ($\{\boldsymbol{y}(0), \boldsymbol{v}(0)\} = \{\boldsymbol{0}, \boldsymbol{0}\}$) for each system of size N, the fluctuations disappear, as seen in Figure 5.5.

A final portrait of the dynamics of the system resulting from the application of a single tap can be obtained through the evolution of the total specific kinetic energy, $KE = \frac{1}{2}\sum_{i=1}^{N} v_i^2$. The tap was initiated with particles just touching each other so that$\{\boldsymbol{y}(0), \boldsymbol{v}(0)\} = \{\boldsymbol{0}, \boldsymbol{0}\}$. Figure 5.7 shows $KE/KE_{max}^{(1)}$ ($KE_{max}^{(1)}$ denotes the maximum

kinetic energy attained by a single sphere, i.e., $N = 1$) versus t/T , where the colorspectrum represents columns of sizes $1 \leq N \leq 50$, with pure red signifying $N = 1$, transitioning through orange as N increases, and finally to violet for $N = 50$ (the top curve). In describing the graph of $KE/KE_{max}^{(1)}$ versus t/T, reference to the term 'peak' will be used to generically explain the physical phenomenon, with the understanding that the actual location (in time) and magnitude of the peak depends on N. The first peak of

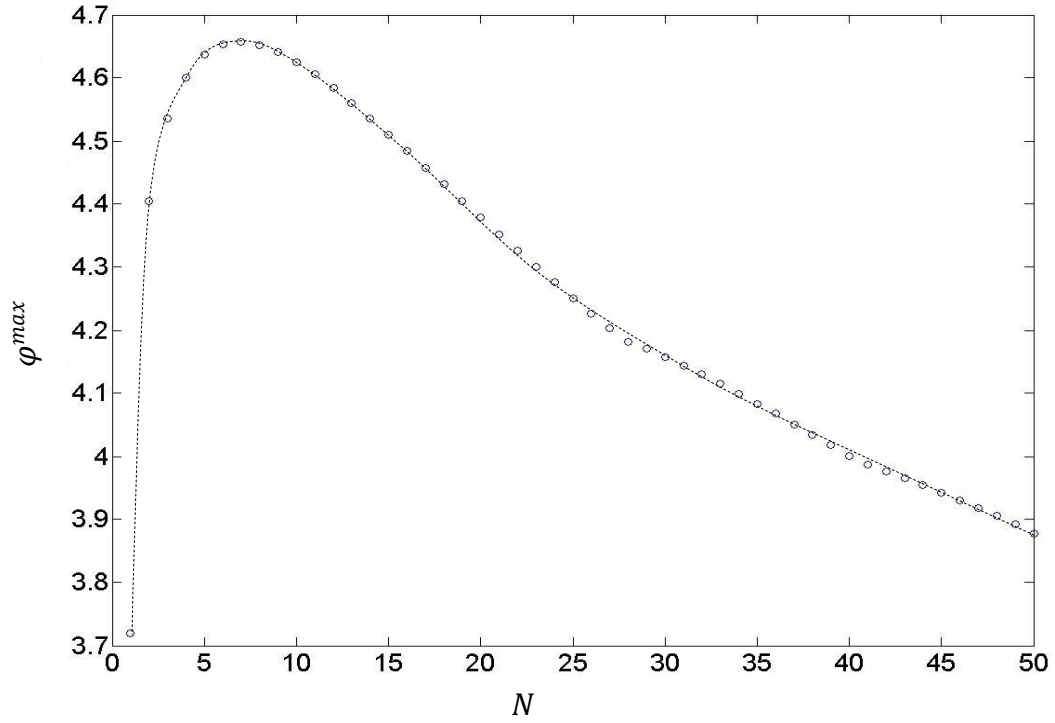

Figure 5.5 Graph of φ^{max} as a function of N for tap parameters $a/d = 0.5$, $f = 15\ Hz$, and $e = 0.90$. Each of the N systems have the same initial conditions, $\{\boldsymbol{y}(0), \boldsymbol{v}(0)\} = \{\mathbf{0}, \mathbf{0}\}$. The dotted line shows the trend of the data.

the graph is a result of the tap (floor motion) transmitting energy (velocities) to the particles of the column[5]. In fact, during this initial stage while the tap is being applied, the only collisional dissipation is that due to ensuing contact interactions between the particles as they begin to acquire their velocities. After attaining a maximum kinetic

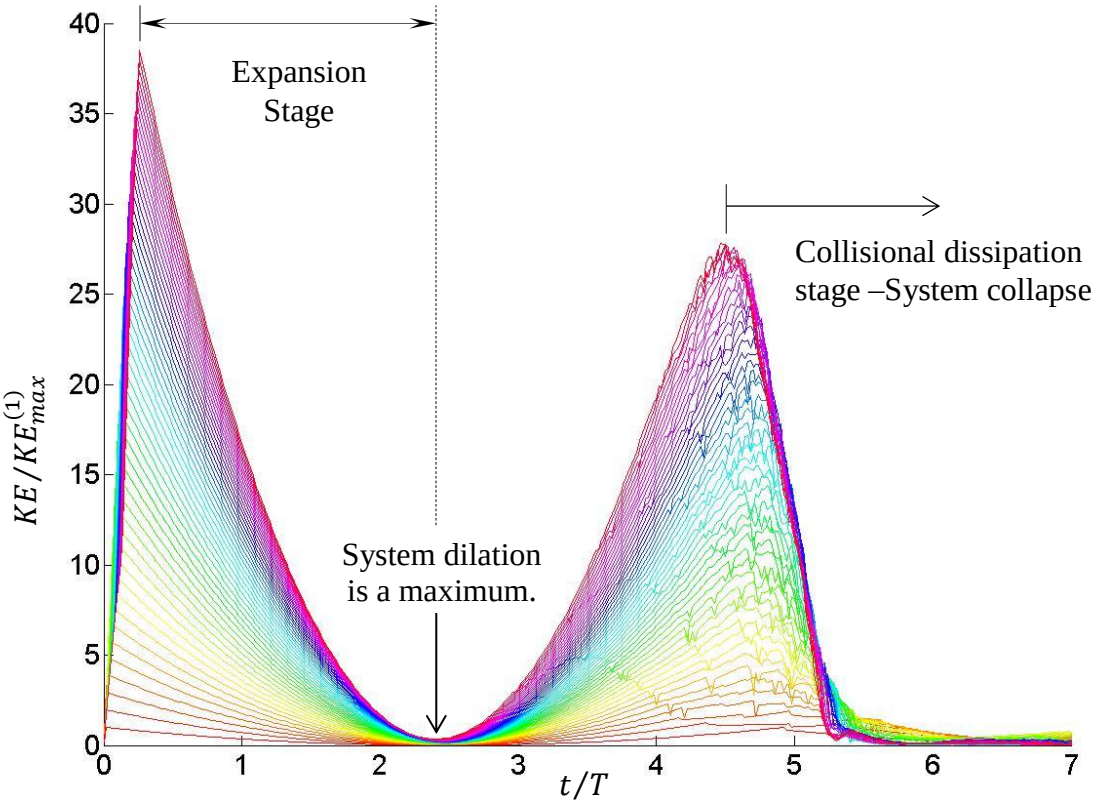

Figure 5.6 Normalized kinetic energy of the system versus t/T for a single tap ($a/d = 0.5,\ f = 10\ Hz,\ e = 0.90$. The color scale (red through violet) signifies columns of increasing size, $1 \leq N \leq 50$.

energy, the system as a whole begins to dilate (or expand) as inter-particle contacts are broken, accompanied by a reduction of particle velocities (due to gravity) until the

5 Note that the sharp gradient up to this peak is due to the scale of the horizontal axis.

dilation is maximum, as can been seen in the figure. From the maximum dilated state, the system then begins to experience a collapse from gravitational forces during which time, particle velocities increase until the second peak of the graph. In due course,

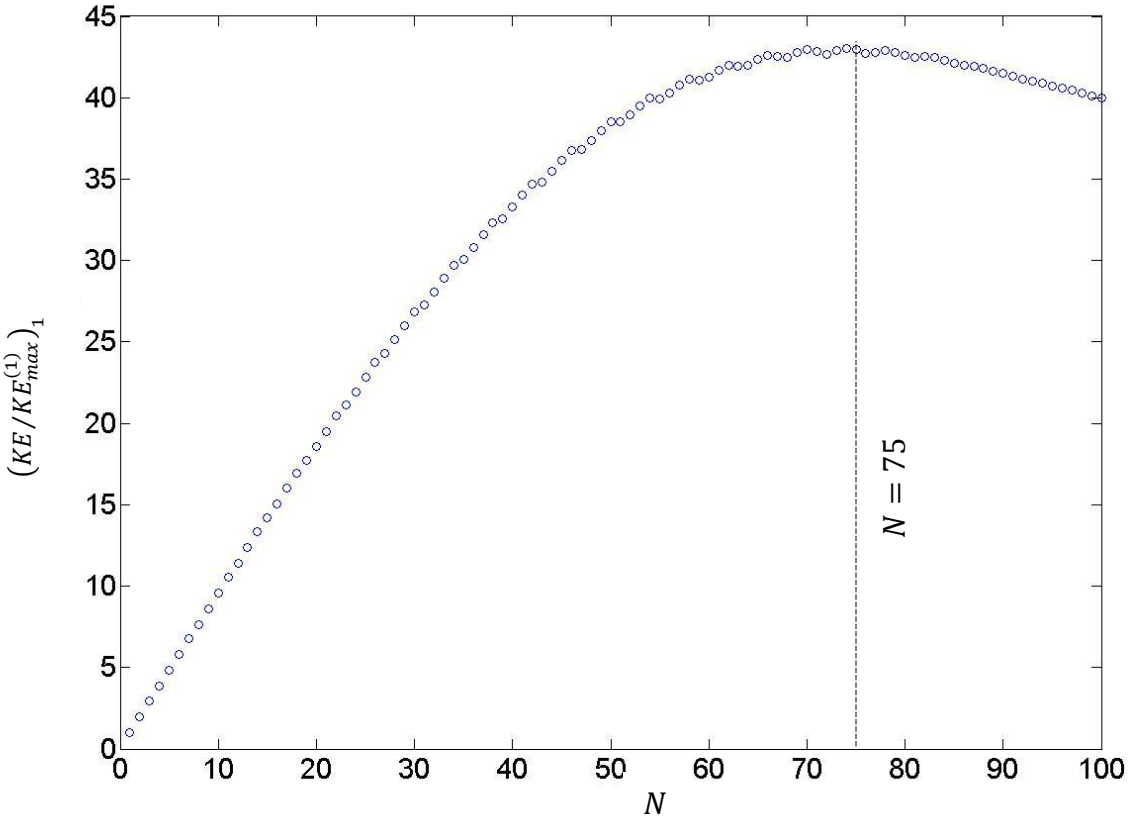

Figure 5.7 The first peak of $KE/KE_{max}^{(1)}$ as a function of N ($1 \leq N \leq 100$) for a single tap ($a/d = 0.5,\ f = 10\ Hz,\ e = 0.90$.

particles begin to collide, signaling the onset of the collisional dissipation stage that is roughly denoted in the figure. The first peak of $KE/KE_{max}^{(1)}$ as a function of N ($1 \leq N \leq 100$) displayed in Figure 5.7 grows with N, reaches a maximum, and then begins to drop at $N \cong 75$ as a consequence of the interplay between a fixed input energy and greater contact dissipation. In a similar fashion, the second peak of $KE/KE_{max}^{(1)}$ versus $N(1 \leq$

$N \leq 100$) is plotted in Figure 5.8. The peak scaled with N for $1 \leq N \lesssim 42$, which is consistent with the proportionality of the average collision frequency $\bar{f}_c$ versus N for $1 \leq N \leq 50$ as shown in Figure 4.13. In particular, a linear regression on the data yields that $\left(KE/KE_{max}^{(1)}\right)_2 = 0.5688N + 0.6738$ with $R^2 = 0.988$.

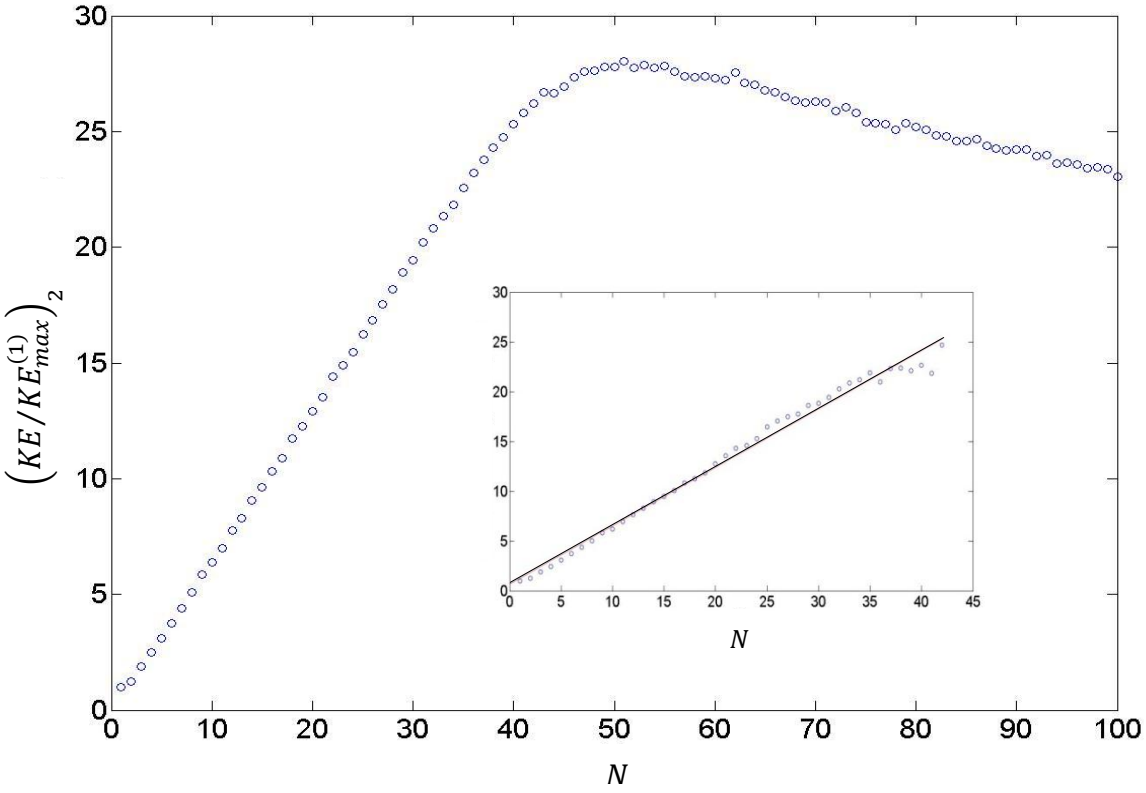

Figure 5.8 The second peak of $KE/KE_{max}^{(1)}$ as a function of N ($1 \leq N \leq 100$) for a single tap ($a/d = 0.5,\ f = 10\ Hz,\ e = 0.90$. The inset shows the linear regression line for $1 \leq N \leq 42$.

5.2.1 Further Discussion on the Effect of Gravity Preload on the Dynamics

As exhibited in the previous section, the initial state of the system (equivalently, the initial phase space point) when tapping begins has a significant effect on the ensuing

dynamics (e.g., see Figures 5.2 to 5.5). Under the preloading[6] caused by gravity, contacts are active due to slight overlaps between particles. Despite the fact that tapping is initiated at the same time instant for all of the systems, the state of each will be at

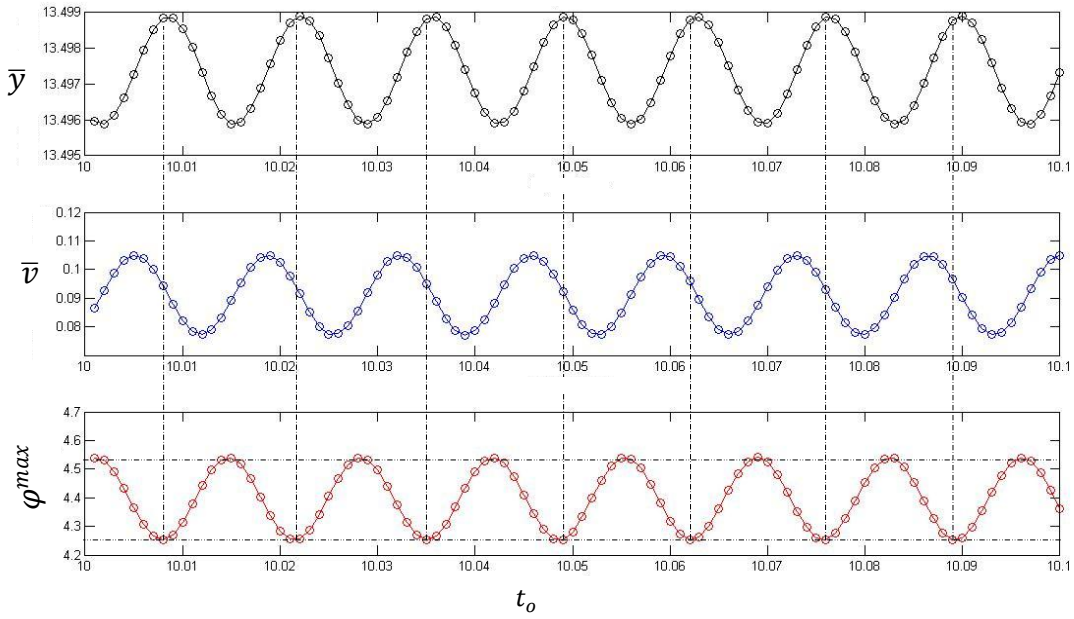

Figure 5.9 Variation of φ^{max} as a function of the time instant t_o when the tap is initiated. The top and center graphs show the location of the mass center $\bar{y}$ and its velocity $\bar{v}$, respectively at t_o. $(a/d = 0.5, f = 10\ Hz, e = 0.90)$.

different point of phase space since this is contingent upon the number of particles N in the column. Indeed, if one were to fix the column size and then very slightly perturb the time instant when the floor begins to move, analogous fluctuations would be present in computed physical quantities, as was observed in Figures 5.2 – 5.5.

The aforementioned conjecture is tested by computing the evolution of the maximum free space φ^{max} (equation (5.2)) for a column having $N = 27$ particles over a range of tap starting times in a small time interval $[10, 10.1]\ s$. The 10 second waiting period was chosen to ensure stability of the column fluctuations from the gravity preload.

6 Before the floor is moved.

Results are summarized in Figure 5.9, which shows the phase point coordinate $(\bar{y},\ \bar{v})$ of the mass center at the instant when the tap is initiated (denoted as t_o) versus $\varphi^{max} \subset$

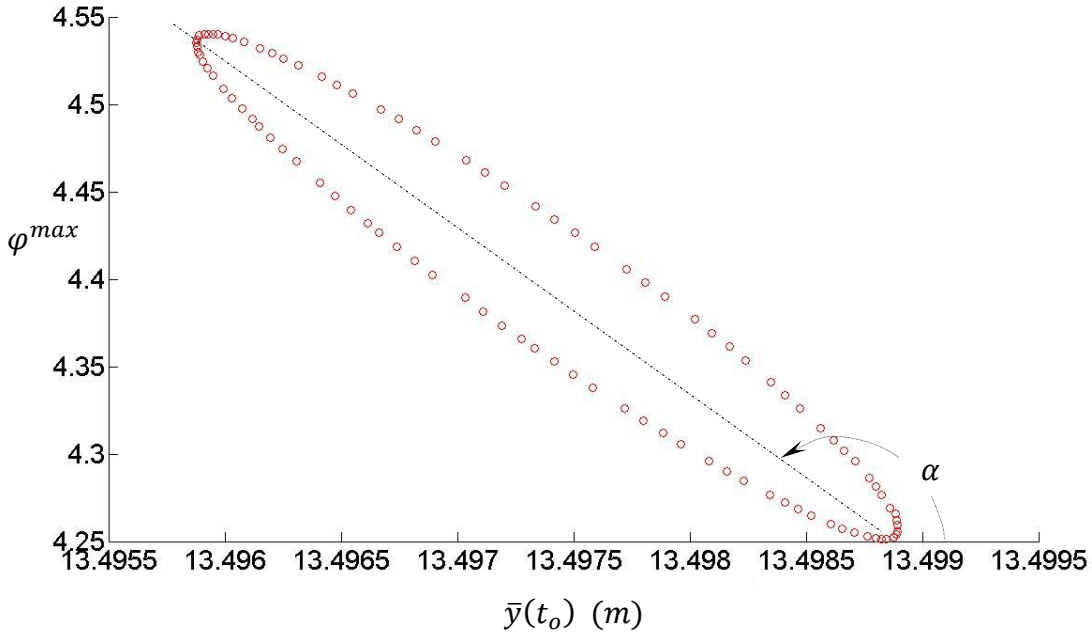

Figure 5.10 φ^{max} plotted against the location of the mass center $\bar{y}$ at the time t_o when the floor motion is initiated over the duration of a single tap ($a/d = 0.5$, $f = 10\ Hz$, $e = 0.90$). The dotted line signifies the major axis of the ellipse at angle α from the horizontal axis.

$[4.25, 4.54]$. Dashed vertical lines in the figure are drawn to display correlations between the data. The data of Figure 5.8 can be rearranged by plotting φ^{max} against $\bar{y}(t_o)$ and $\bar{v}(t_o)$, the results of which are shown in Figures 5.10 and 5.11, respectively. For both plots, the data takes on an elliptical shape whose parametric equations are given by

$$\begin{aligned} \varphi^{max} &= \varphi_o^{max} + a\cos\theta\ (\sin\alpha) + b\sin\theta\ (\cos\alpha) \\ x &= x_o + a\cos\theta\ (\cos\alpha) - b\sin\theta\ (\sin\alpha) \end{aligned} \quad , \qquad (0 \le \theta \le 2\pi), \qquad (5.3)$$

where $x := \bar{y}$ (Figure 5.10), $x := \bar{v}$ (Figure 5.11), (φ_o^{max}, x_o) is ellipse center, α is the angle between the x–axis and the major axis of the ellipse and θ is the parameter.

It was noted in Figure 5.4 that the magnitude of the fluctuations in φ^{max} increased with the number of particles in the column. Although the dimension of the phase space increases with N so that initial conditions are not the same upon initiation of the tap for different column sizes, this does not explain why the fluctuations grow. However, as the column size grows, the magnitude of the overlap between any particular sphere and its upper neighbor depends on the overburden load, i.e., number of sphere sitting on top of it. Consequently, the cumulative overlap and subsequently the net force acting at the column mass center increases with N so that the amplitude of oscillations of the phase space also grows with N. This in turn will cause larger fluctuations in φ^{max} as N increases.

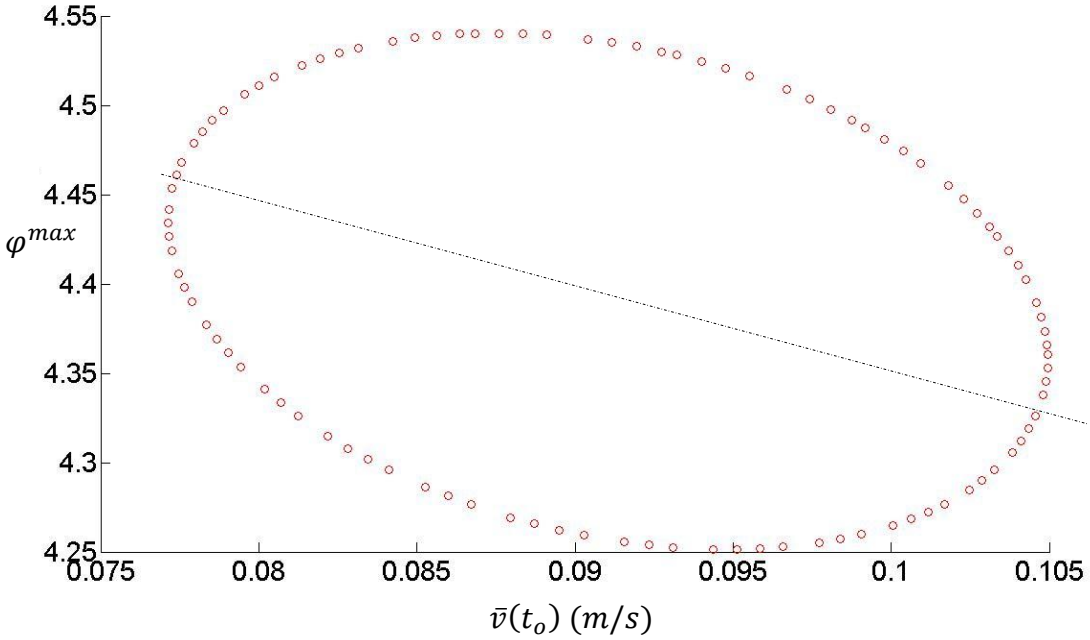

Figure 5.11 φ^{max} plotted against the velocity of the mass center $\bar{v}$ at the time t_o when the floor motion is initiated over the duration of a single tap ($a/d = 0.5$, $f = 10\ Hz$, $e = 0.90$). The dotted line signifies the major axis of the ellipse.

5.3 Influence of Restitution Coefficient on Column Dilation

The restitution coefficient determines the quantity of energy lost in collisions and as such, it will have a significant effect on the dynamics of each particle in the column. Consequently, the mass center embodies the behavior of the individual particles. Figure 5.12 shows the mass center evolution for a single tap (initiated at $t = 10\,s$, such that

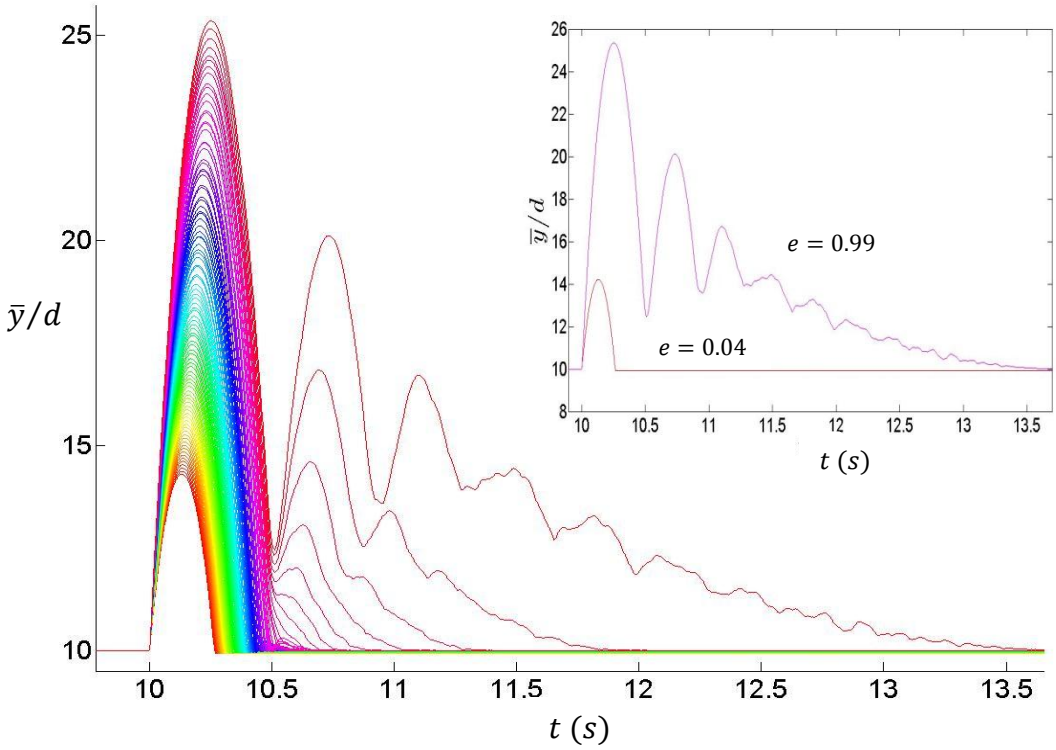

Figure 5.12 Evolution of the mass center for a single tap (initiated at $t = 10\,s$, such that $a/d = 0.50,\ f = 10\,Hz$) applied to a column of $N = 20$ spheres for $0.04 \leq e \leq 0.99$ as indicated by the different line colors. The inset shows the evolution for $e = 0.04$ and $e = 0.99$.

$a/d = 0.50,\ f = 10\,Hz$) applied to a column of $N = 20$ spheres for $0.04 \leq e \leq 0.99$ as indicated by the different line colors. For small restitution coefficients, the trajectories

exhibit only a single large peak characteristic of enough collisional dissipation to damp out the motion; however, as e increases, one begins to observe the formation of other peaks. The maximum dilation or expansion of the system is associated with the first

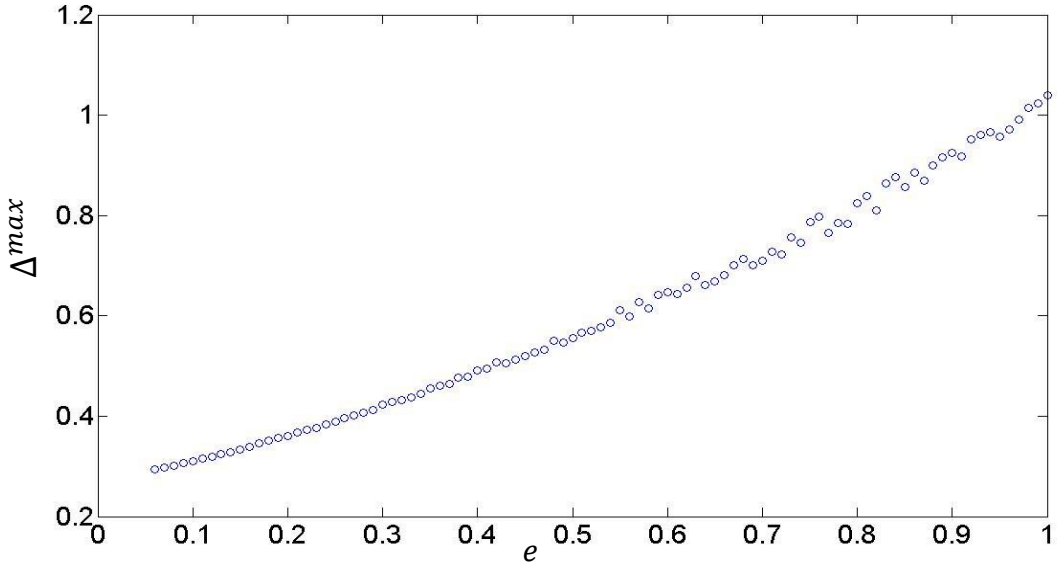

Figure 5.13 Graph of $\Delta^{max} = \underbrace{max}_{t \geq 0} \left\{ \frac{\bar{y}}{d}(t) - \frac{\bar{y}}{d}(10) \right\}$ (equation (5.1)) versus e for a column of $N = 20$ spheres tapped at $a/d = 0.5$ and $f = 10\ Hz$.

peak of the mass center, denoted by Δ^{max} (see equation (5.1) for definition) which is shown versus e in Figure 5.13.

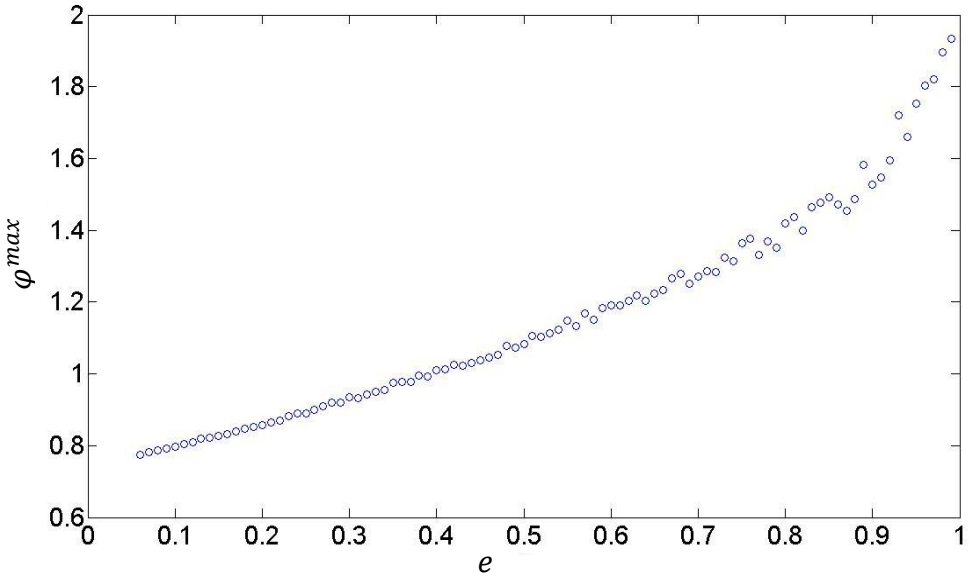

Figure 5.14 φ^{max} (see equation (5.2)) versus e for a column of $N = 20$ spheres tapped at $a/d = 0.5$ and $f = 10\ Hz$.

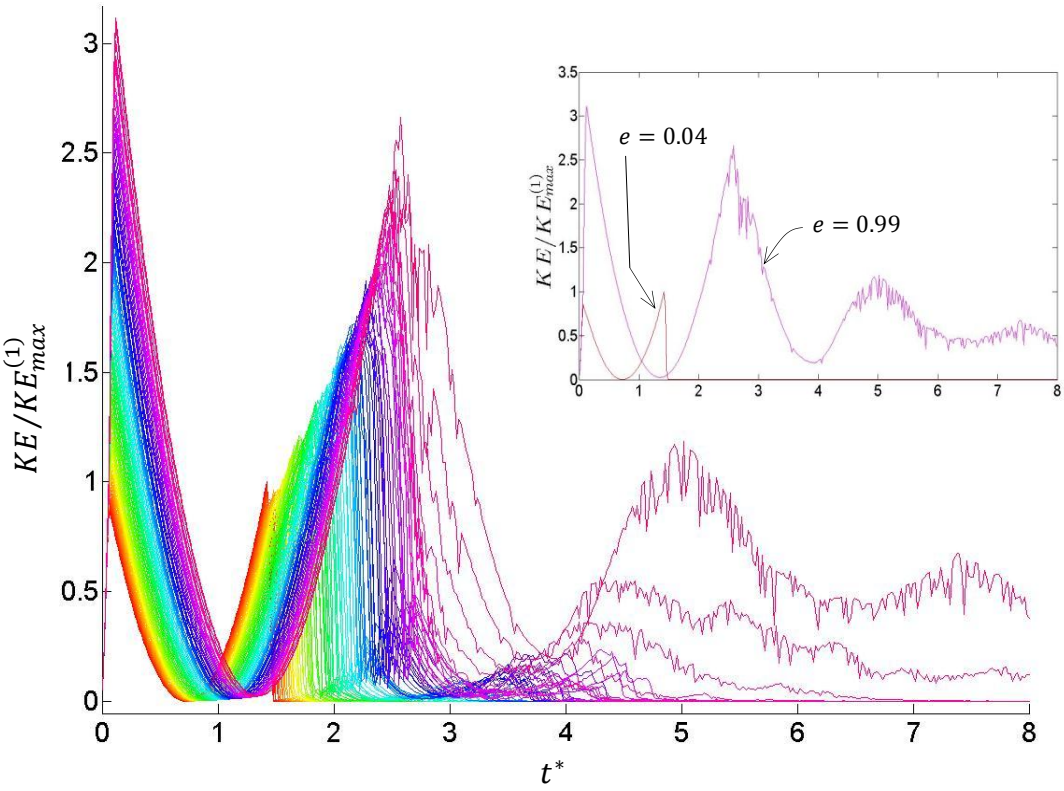

Figure 5.15 Kinetic energy of the system $KE/KE_{max}^{(1)}$ versus $t^* := (t - 10)/T$ Fora column of $N = 20$ spheres tapped at $a/d = 0.5$ and $f = 10\,Hz$. The different colors represent restitution coefficients $0.04 \leq e \leq 0.99$. The inset shows the evolution for $e = 0.04$ and $e = 0.99$.

The slight upward bending of the data for large e points to the availability of more of the initial tap energy, which will cause it to execute a progression of bounces as its motion damps out. Another representation of the effect of restitution coefficient is obtained via the maximum free space (equation (5.2)) φ^{max}, as shown in Figure 5.14. When $e \gtrsim 0.80$, the data bends upward more steeply than what occurs for Δ^{max} (Figure 5.13) since φ^{max} captures the dynamics of only the top particle of the column.

The evolution of the scaled kinetic energy $KE/KE_{max}^{(1)}$ of the system in a single tap as a function restitution coefficient ($0.04 \leq e \leq 0.99$) is depicted in Figure 5.15. (Recall that $KE_{max}^{(1)}$ denotes the maximum kinetic energy of a single sphere during a tap). The inset shows the results for $e = 0.04$ and $e = 0.99$. In the former case ($e =$

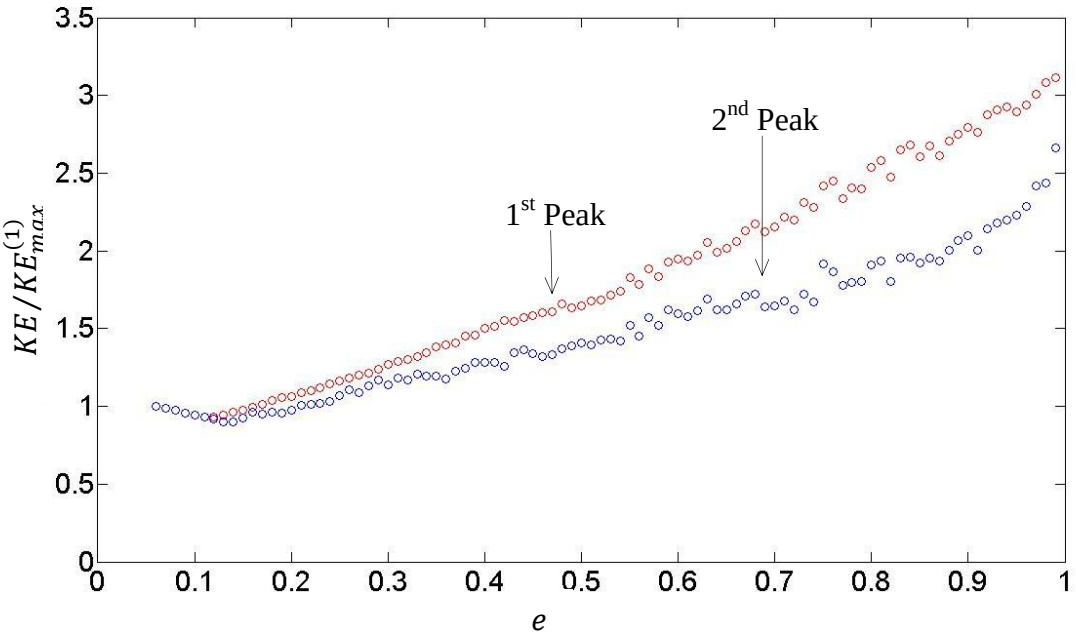

Figure 5.16 First and second peaks of $KE/KE_{max}^{(1)}$ versus e (data presented in Figure 5.15) for a column of $N = 20$ spheres tapped at $a/d = 0.5$ and $f = 10\ Hz$.

0.04), the energy evolution consists of two symmetric peaks (see figure inset), which reflects that fact that due to the very dissipative nature of the contacts, the column will simply bounce upward with spheres in contact with each other. When it returns and strikes the floor, all but approximately 0.16% of the initial tap energy remains. As dissipation decreases, spheres will begin to lose contact with each other, which is reflected in increasing decay rate after the 2nd peak. Note that for $e = 0.99$, the system requires much more time to relax to a state of 'zero' kinetic energy. In fact, the data suggests that for $e \gtrsim 0.85$, the relaxation process involves particles bouncing upwards as they ultimately settle down to their pre-tapped state. The first and second peaks of the normalized kinetic energy $KE/KE_{max}^{(1)}$ versus e are shown on the same set of axes in Figure 5.16. The first peak essentially characterizes the transmission of energy from the tap into the system. The source of the small oscillations at larger values of e in the second peak is due to collisions of particles that take place during the collapse of the

column.

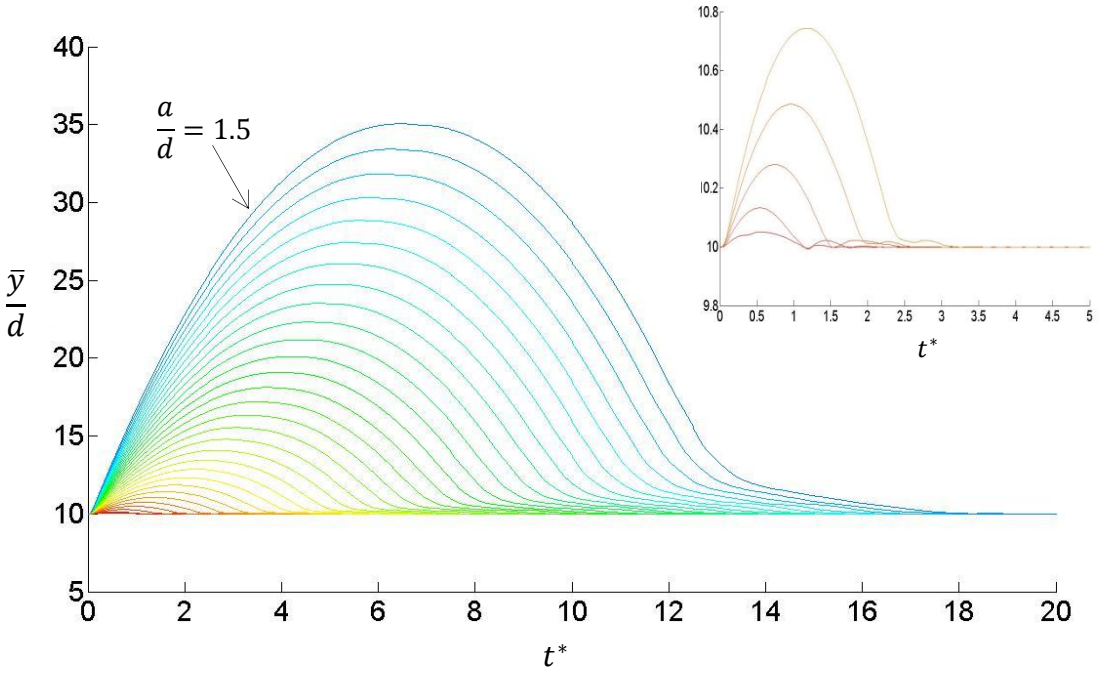

Figure 5.17 Evolution of the mass center $\bar{y}/d$ for tap amplitudes $0.05 \leq a/d \leq 1.5$, $f = 10\ Hz$, $e = 0.90$, and $N = 20$. Each color represents a different amplitude, with the largest noted on the figure. The inset shows $\bar{y}/d$ for the first five a/d values.

5.4 Effect of the Tap Amplitude on Column Dilation

The tap amplitude a/d will change the dynamics of the column by either increasing or decreasing the energy transferred into the system. This subsection presents results of a series of studies in which the tap amplitude is varied while keeping other parameters fixed: $f = 10\ Hz$, $e = 0.90$, $N = 20$. Figure 5.17 shows the evolution ($t^* := (t - 10)/T$) of the mass center for $0.05 < a/d \leq 1.5$, which are denoted by lines of different color, while Figure 5.18 is a graph of the maximum mass center coordinate $(\bar{y}/d)_{max}$ as a function of a/d. A parabolic fit ($R^2 \cong 1$) to the data (shown as the red line in the figure),

$$(\bar{y}/d)_{max} = 11.1\left(\frac{a}{d}\right)^2 + 10.07 \qquad (5.4)$$

is suggestive of the quadratic relationship governing the maximum height attained by a

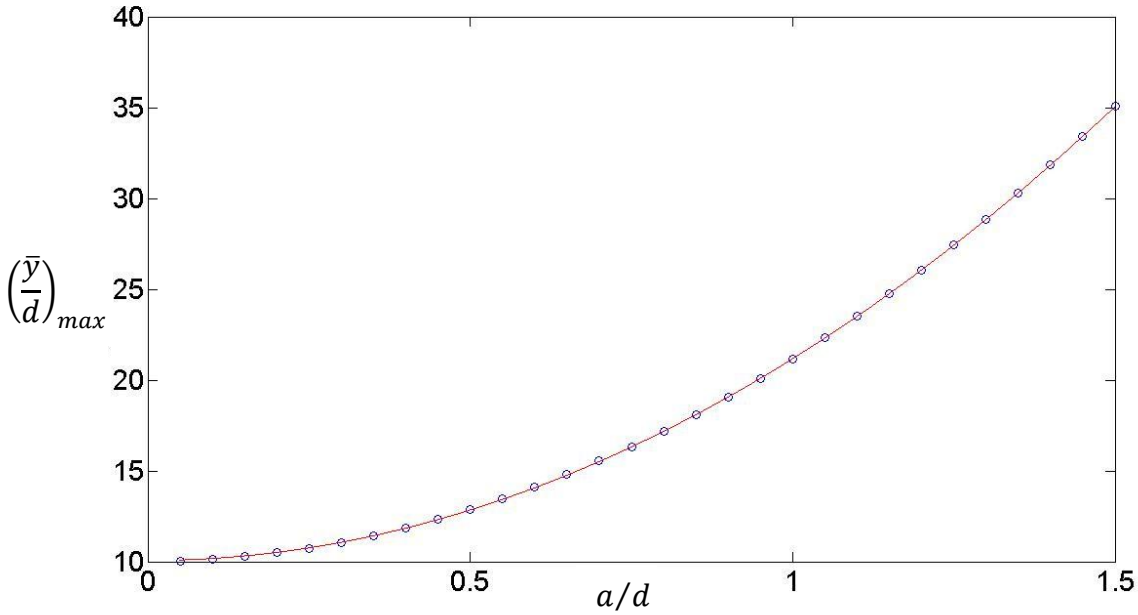

Figure 5.18 Maximum value $\bar{y}/d$ versus a/d over the duration of a single tap for $N = 20, f = 10\,Hz$ and $e = 0.90$. The red line is the parabolic regression given by (5.4).

single ball having an initial velocity $a\omega$, that is, $h = \frac{(\omega d)^2}{2g}(a/d)^2$. Thus the motion of the mass center of the column is qualitatively similar to that of a single particle. Unlike a single ball however, the column will undergo dilation, whose maximum is given by

$$y^d_{max} := \max_{t\geq 0}\left\{\frac{y_N(t) - y_o(t)}{d}\right\} = \varphi^{max} + \left(N + \tfrac{1}{2}\right) \qquad (5.5)$$

The equality follows directly from (5.2). Figure 5.19 shows y^d_{max} versus a/d, where the red line is a parabolic fit ($R^2 \cong 1$) of the form,

$$y^d_{max} = 14.64(a/d)^2 + 19.56 \qquad (5.6)$$

The evolution of the kinetic to energy should also scale with the square of the tap

amplitude in support of the trends reported above (i.e., (5.4) and (5.6)). Let $\mathcal{K}$ be the ratio of the system kinetic to potential energy at time t, written as

$$\mathcal{K}(t) := \frac{\sum_{j=1}^{N} m v_j^2}{2\sum_{j=1}^{N} m g y_j} = \frac{\sum_{j=1}^{N} v_j^2}{2gN\bar{y}} \,. \tag{5.7}$$

So as to maintain the same normalization over all amplitudes, the denominator is chosen to be potential before the tap begins, so that $\bar{y} = Nd/2$ and

$$\mathcal{K}_{max} = \frac{1}{gdN^2} \max_{t\geq 0}\left(\sum_{j=1}^{N} v_j^2\right). \tag{5.8}$$

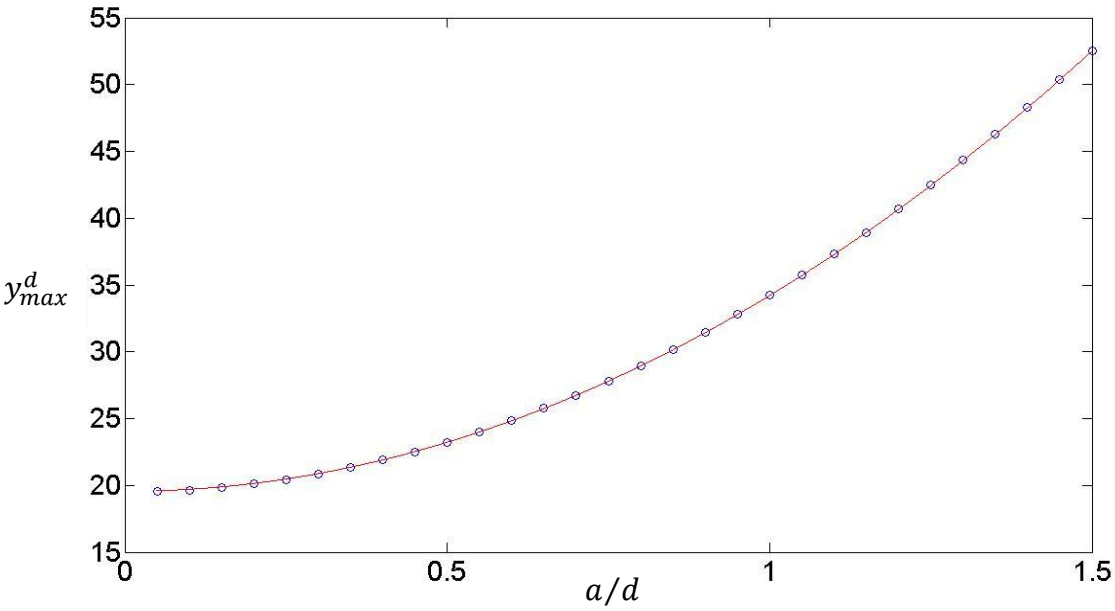

Figure 5.19 Maximum dilation of the column (5.5) versus a/d over the duration of a single tap for $N = 20$, $f = 10\,Hz$ and $e = 0.90$. The red line is the parabolic regression given by (5.6).

Figure 5.20 shows $\mathcal{K}$ versus $t^* := (t - 10)/T$, where the colors represent different values of a/d, such that $0.05 < a/d \leq 1.5$, while Figure 5.21 presents $\mathcal{K}_{max}$ versus a/d. Regression of the data to a quadratic form yields,

$$\mathcal{K}_{max} = 1.1081(a/d)^2 - 0.002769 \qquad (5.9)$$

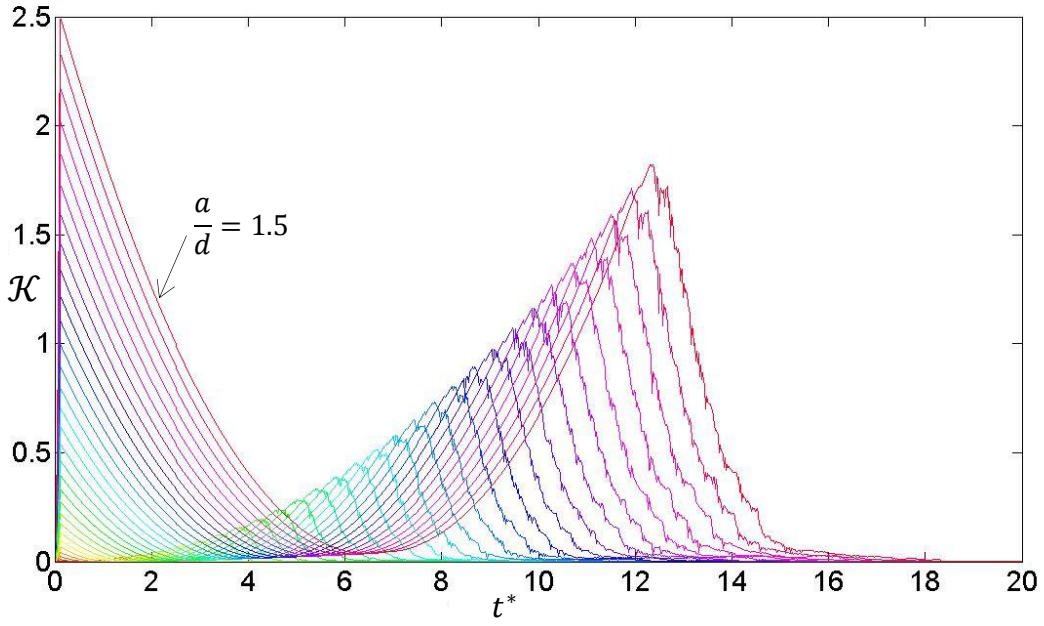

Figure 5.20 Evolution of the kinetic energy $\mathcal{K}$ for $0.05 \leq a/d \leq 1.5$, $f = 10\,Hz$, $e = 0.90$, and $N = 20$ over the duration of a single tap. Each color represents a different amplitude, which decreases from the uppermost curve where $a/d = 1.5$.

Table 5.1 summarizes the statistics of the fits represented by (5.4), (5.6) and (5.9). For each a/d, $\mathcal{K}_{max}$ regulates the degree to which the column dilates, corresponding to the minimum point on each of the curves in Figure 5.20.

Table 5.1 Statistical Parameters for (5.4), (5.6) and (5.9); $f = \alpha(a/d)^2 + \gamma$
Bracketed Numbers are 95% Confidence Intervals.

f	α	γ	R^2
$(\bar{y}/d)_{max}$	11.11(11.1,12 11.12)	10.07(10.05, 10.08)	$\cong 1$
y^d_{max}	14.67(14.66, 14.68)	19.54(19.53, 19.55)	$\cong 1$
$\mathcal{K}_{max}$	1.1081(1.1077, 1.1085)	−0.002769(−0.003240, −0.002299)	$\cong 1$

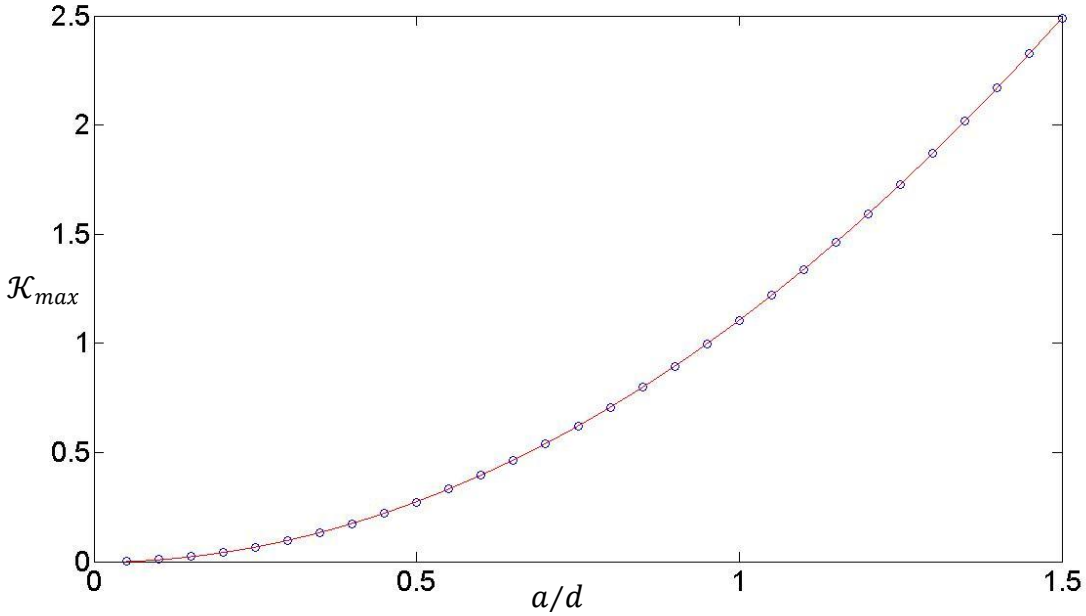

Figure 5.21 The first peak $\mathcal{K}_{max}$ of the scaled kinetic energy (Figure 5.20) versus a/d over the duration of a single tap at $f = 10\ Hz$ applied to a column of $N = 20$ spheres with $e = 0.90$. The red regression line is given by (5.9).

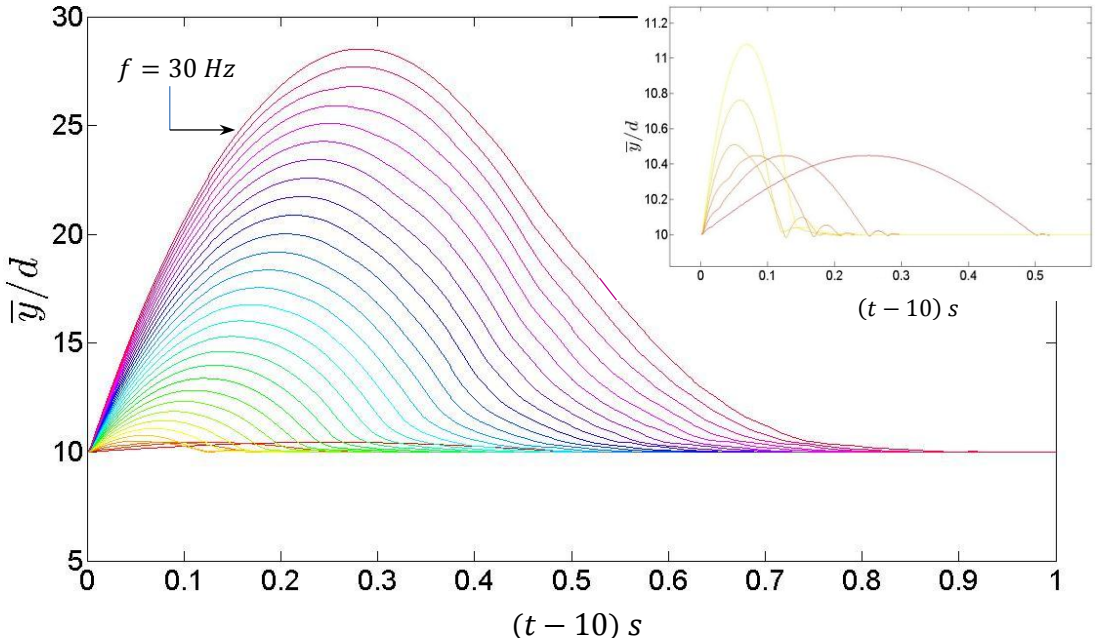

Figure 5.22 Evolution of the mass center $\bar{y}/d$ for $1 \le f \le 30\ Hz$, $a/d = 0.5$, $e = 0.90$, and $N = 20$ for a single tap initiated at $t = 10\ s$. Each color represents a different frequency, with the largest noted on the figure. The inset shows $\bar{y}/d$ for $f = 1, 2, 3, 4\ 5\ Hz$.

5.5 Effect of the Tap Frequency on Column Dilation

In this section, the effect of changing the frequency of the tap at a constant $a/d = 0.5$ is discussed for a column of 20 spheres with restitution coefficient $e = 0.90$. The frequencies here were chosen so that the dimensionless tap energy $(a\omega)^2/gd$, or simply the product of the relative acceleration $a\omega^2/g$ and the normalized amplitude a/d, is the same as for the study (Section 5.4) where $f = 10\ Hz$ and $0.05 \leq a/d \leq 1.5$. The most ostensible effect is associated with the distribution of velocities of the particles over the time scale of the disturbance propagation through the system, which in turn influences column's dilation. Figure 5.22 shows the evolution of the mass center of the column for frequencies $1 \leq f \leq 30\ Hz$, which are distinguished by the different line colors, for a single tap initiated at $t = 10\ s$. Note that the time axis $(t - 10)s$ was not scaled by the

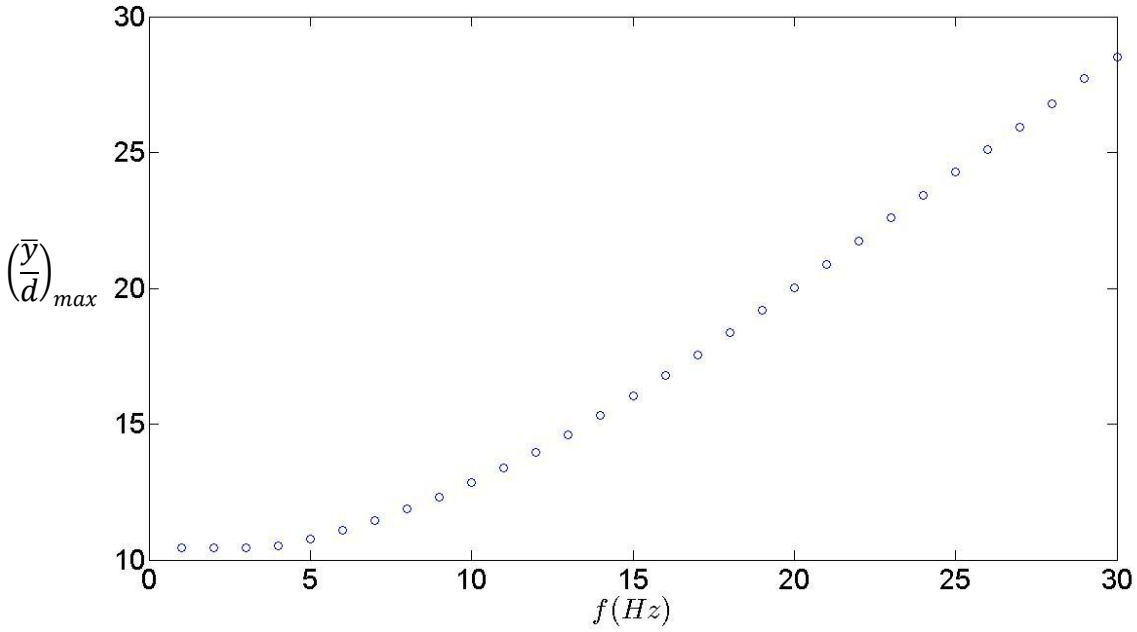

Figure 5.23 Maximum value $\bar{y}/d$ versus f over the duration of a single tap for $N = 20$, $f = 10\ Hz$ and $e = 0.90$. For $f \lesssim 5\ Hz$, the mass center does not experience any appreciable change in its location before the tap was applied. (See inset of Figure 5.22)

period $T = (1/2f) + t_r$ since its value changes with frequency. Peak values $(\bar{y}/d)_{max}$ presented in Figure 5.23 begin to increase with f for $f \gtrsim 5\ Hz$. However, for $f \lesssim 5\ Hz$, the mass center doesn't change appreciably from its pre-tapped position, as is apparent from the inset of Figure 5.22. A plausible explanation for this behavior is related to the fact that for 'hard' spheres (i.e., no overlaps), the column would move intact and in sync with the floor when the tap acceleration is less than g, which corresponds to $f = \left(1/2\pi\sqrt{g/a}\right) = 4.98\ Hz$ when $a/d = 0.5$.

The column will also dilate as indicated in Figure 5.24, which shows y_{max}^{d} (equation (5.5)) versus f. The dotted line marks the location of the top sphere ($y_{20}/d = 20$) if there were no gravitationally-induced overlaps between particles of the column. Note that there is only miniscule dilation for $f \lesssim 5\ Hz$ in agreement with Figure 5.23. It was found that the data was well-fit by a quadratic of the form,

$$y_{max}^{d} = 0.0358f^2 + 19.81 \qquad (5.10)$$

Careful observations of the particle configurations at selected points on Figure 5.19 (amplitude varied) and Figure 5.24 indicated very different distributions of the locations of the particles. When the amplitude was fixed and frequency varied, particles tended to be somewhat evenly spread out. However, this was not the case when the frequency was fixed and the amplitude varied. The reason for this difference is not fully

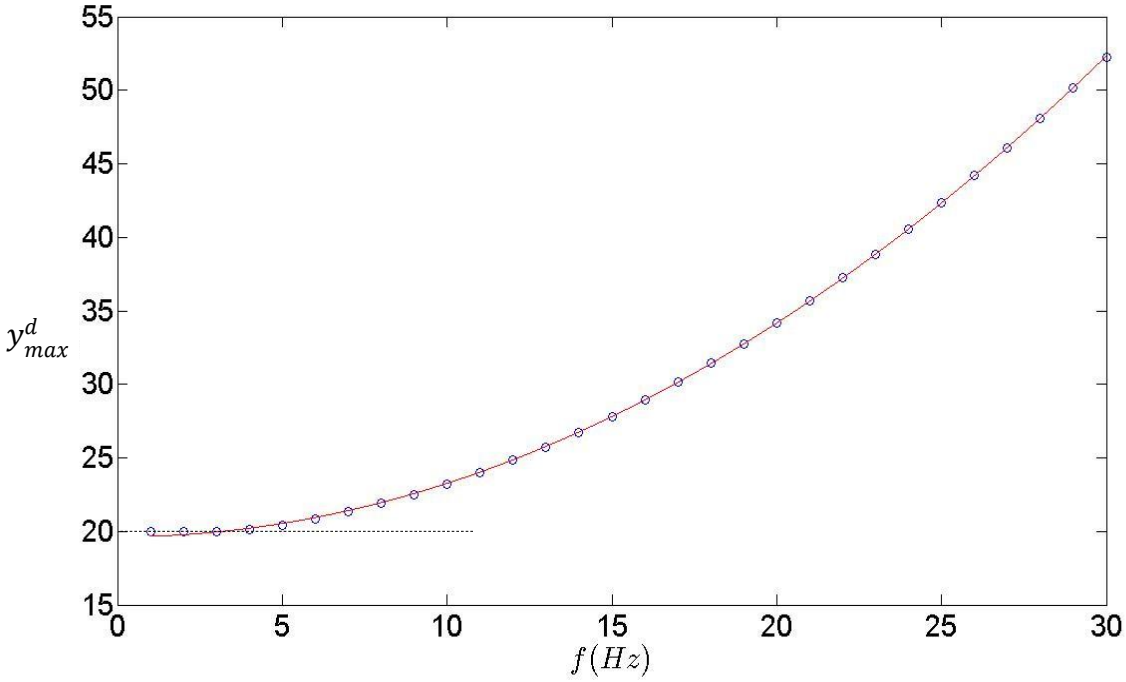

Figure 5.24 Maximum dilation y^d_{max} as a function of f over the duration of a single tap applied to the column for $a/d = 0.5$, $e = 0.9$ and $N = 20$. The dotted line marks the theoretical location of the top sphere before application of the tap.

understood so that further investigation is required. The evolution of the scaled kinetic energy $\mathcal{K}$ is plotted against $(t - 10)$ in Figure 5.25 for $1 \leq f \leq 30\ Hz$, denoted by the different line colors. The inset shows $\mathcal{K}$ vs. $(t - 10)$ for the first five frequencies. As

compared with the profiles seen in Figure 5.20, the sharp second peak in $\mathcal{K}$ is not markedly evident, and the time scale over which the column collapses appears to be longer. It is conjectured that latter observation is a consequence of the configuration of the particles at the time when the column begin its final progression to a state of minimal

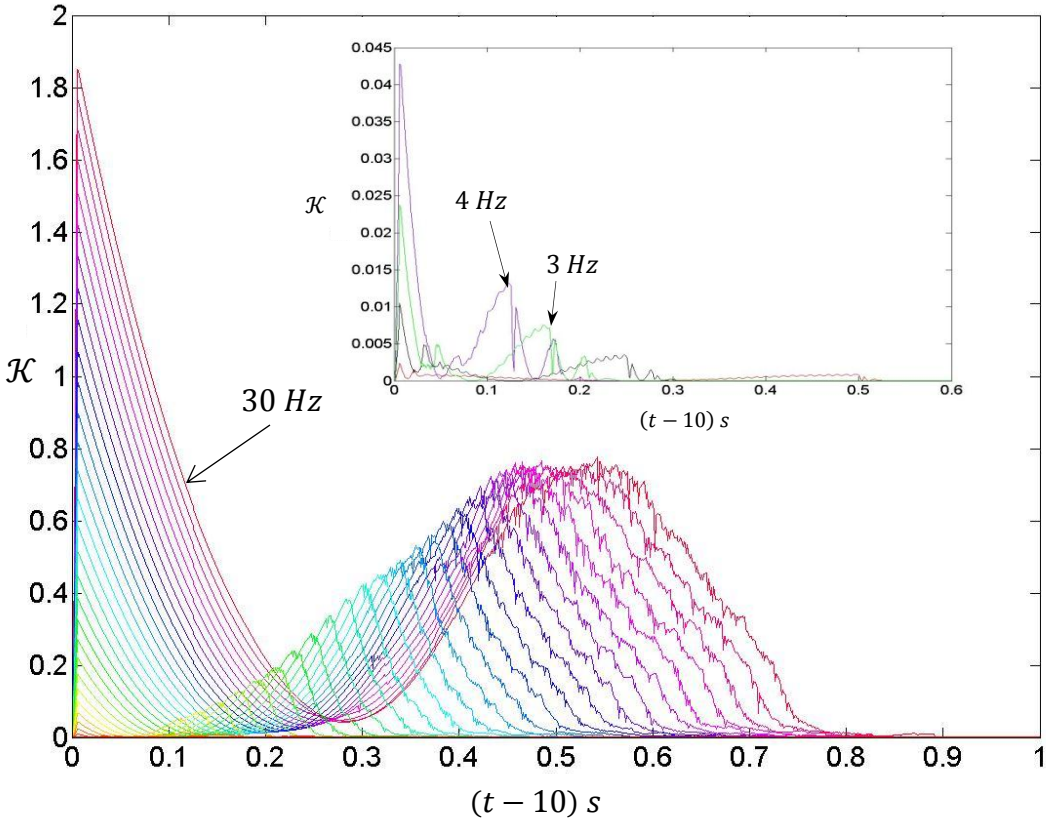

Figure 5.25 Evolution of $\mathcal{K}$ for $1 \leq f \leq 30\ Hz$, $a/d = 0.5$, $e = 0.90$, and $N = 20$ for a single tap initiated at $t = 10\ s$. Each color represents a different frequency, with the largest noted on the figure. The inset shows $\bar{y}/d$ for $f = 1, 2, 3, 4\ Hz$.

kinetic energy. Another observation relevant to the influence of increasing tap frequency at a fixed amplitude is the rather complex evolution seen in the insert to Figure 5.25 compared with the insert of Figure 5.22, where a/d was varied at $f = 10\ Hz$. The first peak in $\mathcal{K}$ versus$f$ are shown in Figure 5.26.

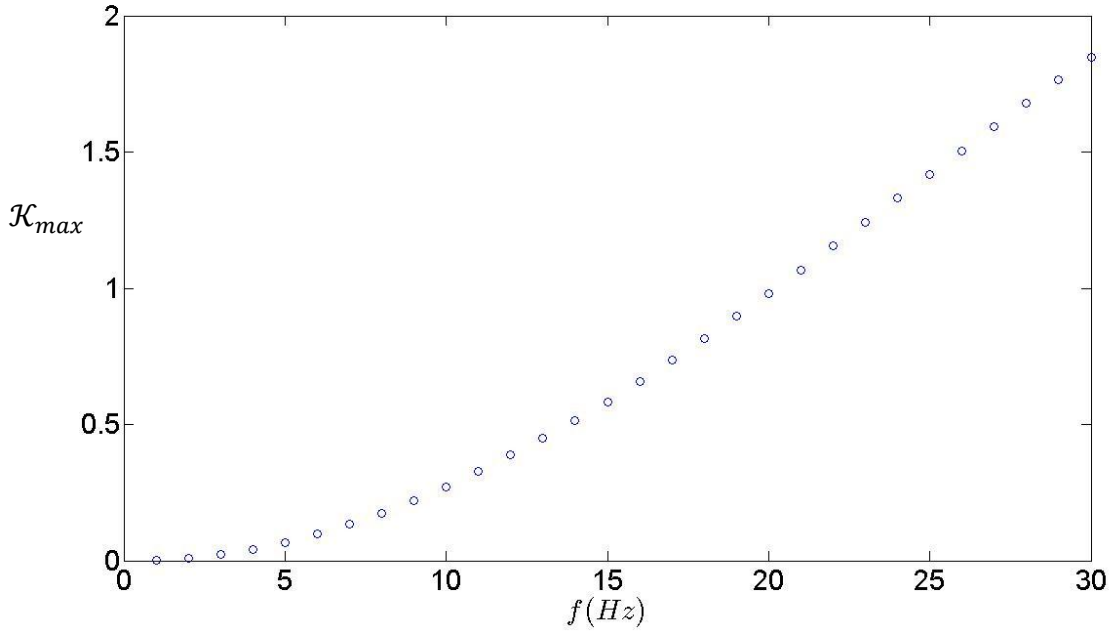

Figure 5.26 The first peak of the scaled kinetic energy $\mathcal{K}_{max}$ (Figure 5.25) versus f over the duration of a single tap at $a/d = 0.5$ applied to a column of $N = 20$ spheres with $e = 0.90$.

5.6 Comparison of Results for Equally Energetic Taps

In order to compare findings for the two studies in which the amplitude and frequency were varied, results are plotted on the same set of axes in Figures 5.27 and 5.28. It is important to note that tap energy for the two case studies matches point for point. That is, $\{(a\omega)^2/dg \mid a/d = 0.5,\ 1 \le f \le 30\} = \{(a\omega)^2/dg \mid f = 10, 0.05 \le (a/d) \le 1.5\}$.

One observes that for both $(\bar{y}/d)_{max}$ and $\mathcal{K}_{max}$ at $f \cong 15\,Hz$, the frequency-varied data (open squares) begins to diverge from the data where the amplitude was varied (open circles). A clearer delineation of this divergence is given in Figures 5.29 and 5.30, in which the data is plotted against the dimensionless tap energy $(a\omega)^2/gd$, or simply the product of the relative acceleration $a\omega^2/g$ and the normalized amplitude a/d. A linear regression (5.11) to the amplitude-varied data (red line) yielded a perfect

fits of both $(\bar{y}/d)_{max}$ and $\mathcal{K}_{max}$ against $(a\omega)^2/gd$, suggesting a direct variation of these quantities with the tap input energy.

$$y_{max}^{d} = 71.97\,[(a\omega)^2/gd] + 19.54$$
$$\mathcal{K}_{max} = 5.434[(a\omega)^2/gd] - 0.002769 \qquad (5.11)$$

However, quadratic variation of $(\bar{y}/d)_{max}$ and $\mathcal{K}_{max}$ with $(a\omega)^2/gd$ was not found as evident in Figures 5.29 and 5.30. Table 5.2 lists the fitting parameters. The application of the same tap energy, regardless of whether the amplitude is fixed and frequency varied, or visa versa, produces the same maximum dilation y_{max}^{d} of the

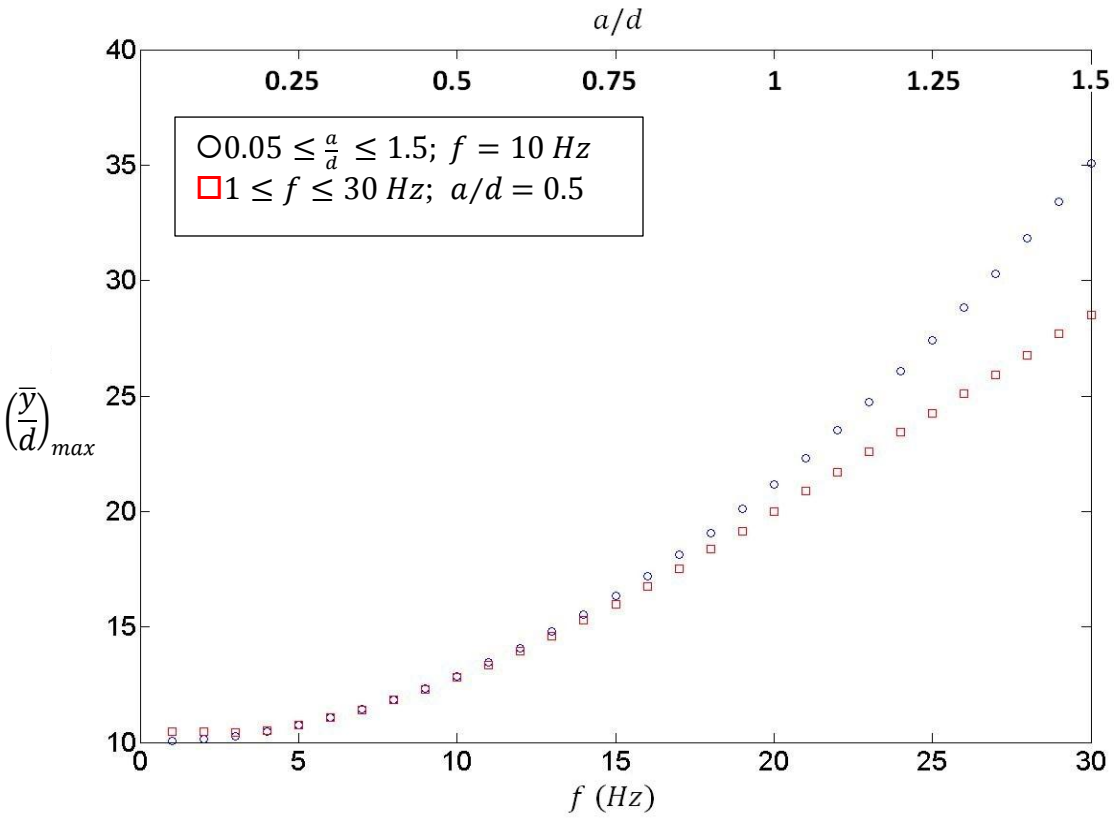

Figure 5.27 $(\bar{y}/d)_{max}$ versus a/d (○) and versus f (□) over the duration of a single tap for $N = 20$ and $e = 0.90$.

column. This can be seen in Figures 5.31 and 5.32. However, the internal arrangement or distribution of the spheres differs depending on how the tap was applied.

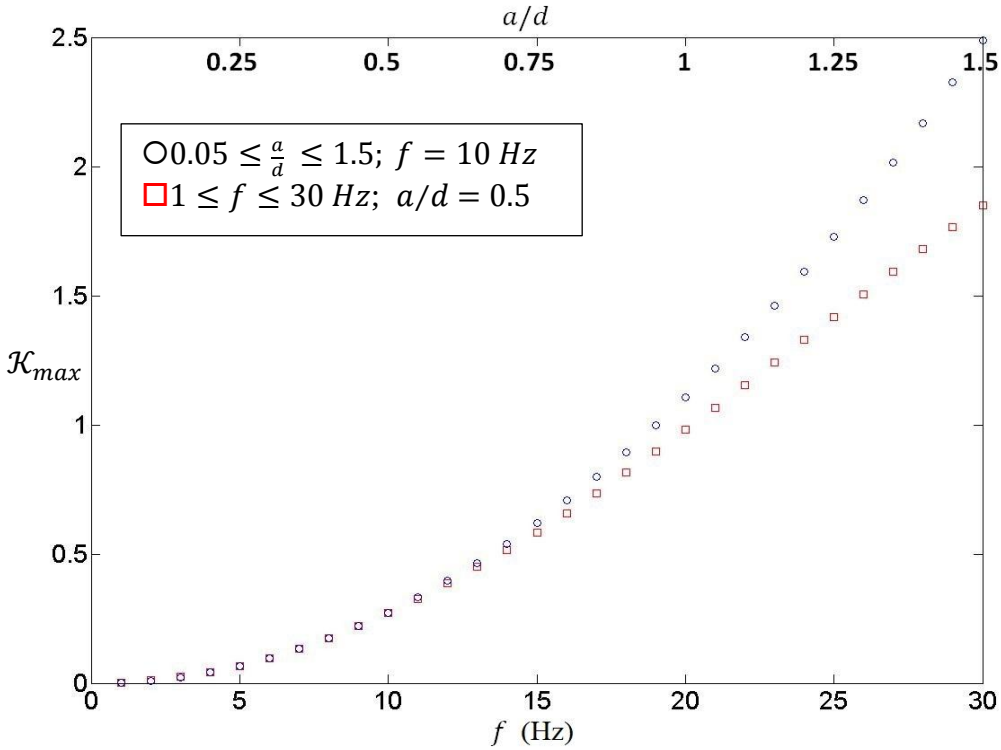

Figure 5.28 $\mathcal{K}_{max}$ versus a/d (○) and versus f (□) over the duration of a single tap for $N = 20$ and $e = 0.90$.

5.7 A General Portrait of the Column's Dynamics

In general, one can qualitatively describe the behavior of the system through the evolution of its kinetic energy as depicted in the specific case of Figure 5.6, or via the general characterization of the process as shown in Figure 5.31. As the tap is applied to the column, particles gain kinetic energy over a short time scale associated with the propagation of a disturbance wave through the system. The system kinetic energy attains a maximum, and thereafter, the column expands (i.e., particles lose contact with other) to its lowest density. The presumption here is that the tap is sufficiently energetic so that particles eventually break contacts, as opposed to the entire system moving in sync with

the floor. From this point, the system as a whole starts to collapse as particles gain kinetic energy due to gravitational acceleration. Eventually, collisions start to occur between adjacent particles in the column to produce energy loss, which ultimately takes the system to a point in its phase space having minimal kinetic energy with very minute fluctuations. As depicted in Figure 5.27, one expects that the time scale over which the system energy decays will depend on the phase point. For instance, consider two identical systems (i.e., same N, e and mass m) at phase points $(\boldsymbol{y}^a, \boldsymbol{v}^a)$ and $(\boldsymbol{y}^b, \boldsymbol{v}^b)$ that have the same system energy $\mathcal{E}^*$ at time t when the column begins to collapse. Further suppose each has the same potential energy $\sum_{i=1}^{N} y_i^a = \sum_i^N y_i^b$, and that they have the same dilation so that $y_N^a = y_N^b$. It is conjectured that the system at $(\boldsymbol{y}^b, \boldsymbol{v}^b)$ which is more uniformly distributed along the column's length follows a more circuitous trajectory in phase space, thus requiring great time to decay to a state of zero kinetic energy. This conjecture is consistent with results seen in Figures 5.22 and 5.25. More generally, the time scale over which the energy decays is contingent on the path through phase space.

Table 5.2 Statistical Parameters Regression $f = \beta\,(a\omega)^2/gd + \gamma$. Bracketed Numbers Are 95% Confidence Intervals.

f	β	γ	R^2
$\mathcal{K}_{max}$	$5.434(5.432, 5.436)$	-0.002769(-0.00324,-0.002299)	$\cong 1$
y_{max}^d	$71.97(71.93, 72.01)$	$19.54(19.53, 19.55)$	$\cong 1$

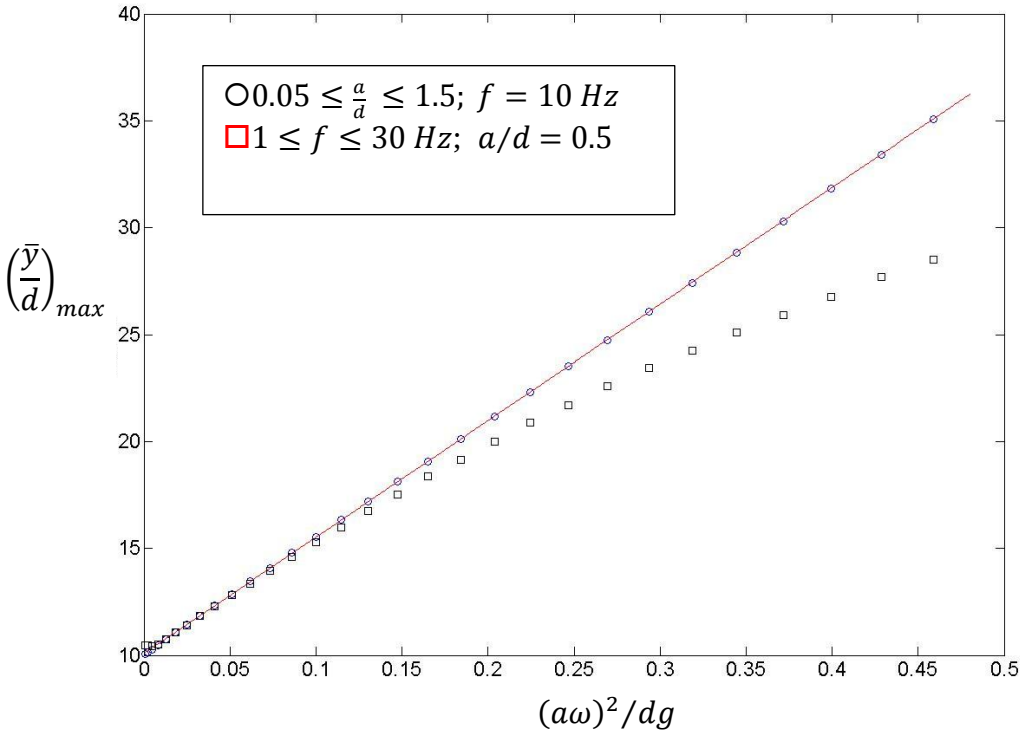

Figure 5.29 $(\bar{y}/d)_{max}$ plotted against $(a\omega)^2/dg$ over the duration of a single tap of $N = 20$ spheres ($e = 0.9$) for ○$f = 10\ Hz$, $0.05 \leq a/d \leq 1.5$, and □a/d 0.5, $1 \leq f \leq 30\ Hz$. The red line through the open circles is a linear regression given in equation (5.11).

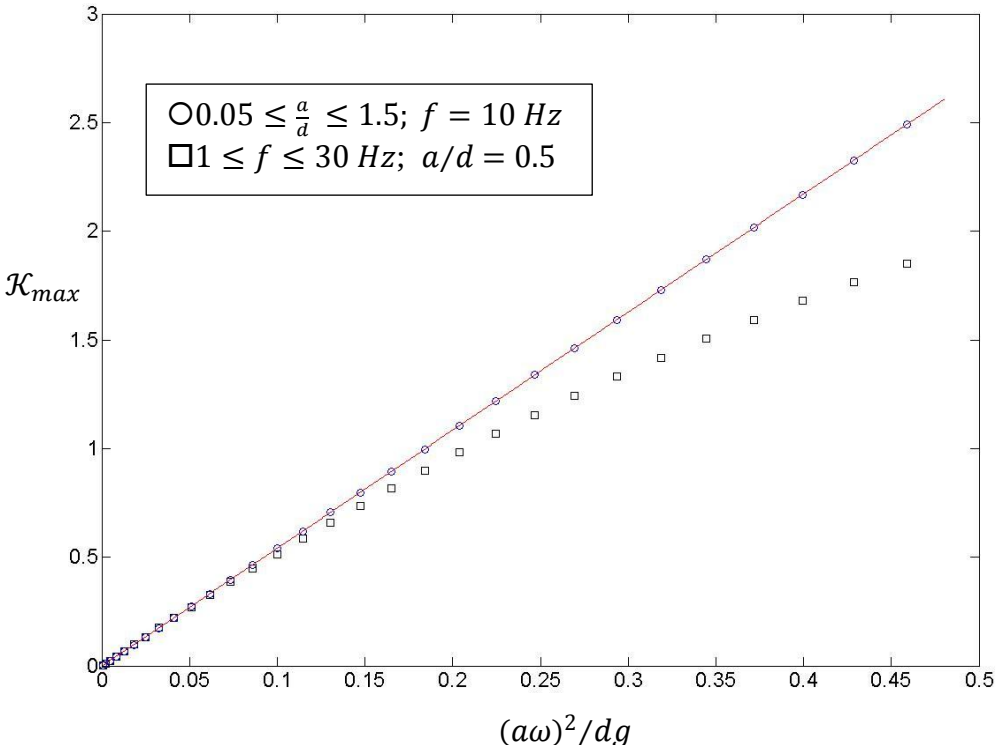

Figure 5.30 $\mathcal{K}_{max}$ plotted against $(a\omega)^2/dg$ over the duration of a single tap of $N = 20$ spheres ($e = 0.9$) for ○$f = 10\ Hz$, $0.05 \leq a/d \leq 1.5$, and □a/d 0.5, $1 \leq f \leq 30\ Hz$. The red line through the open circles is a linear regression given in equation (5.11).

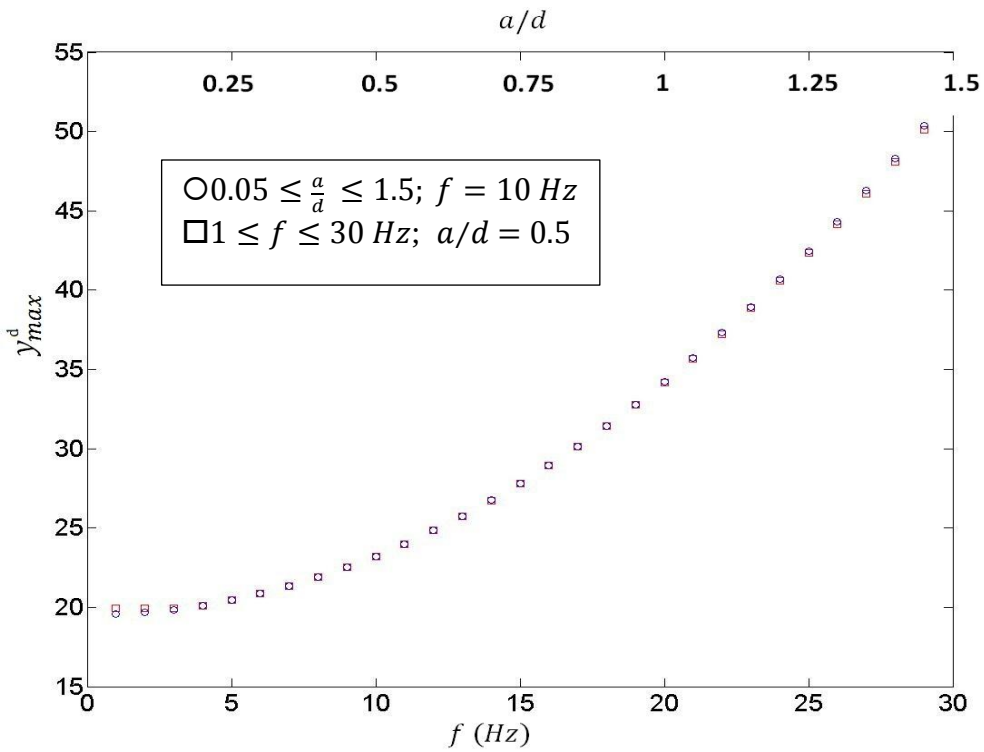

Figure 5.31 Maximum dilation of the column y^d_{max} as a function of f and a/d over the duration of a single tap of $N = 20$ spheres ($e = 0.9$) for ○$f = 10$ Hz, $0.05 \leq a/d \leq 1.5$, and □$a/d = 0.5$, $1 \leq f \leq 30$ Hz.

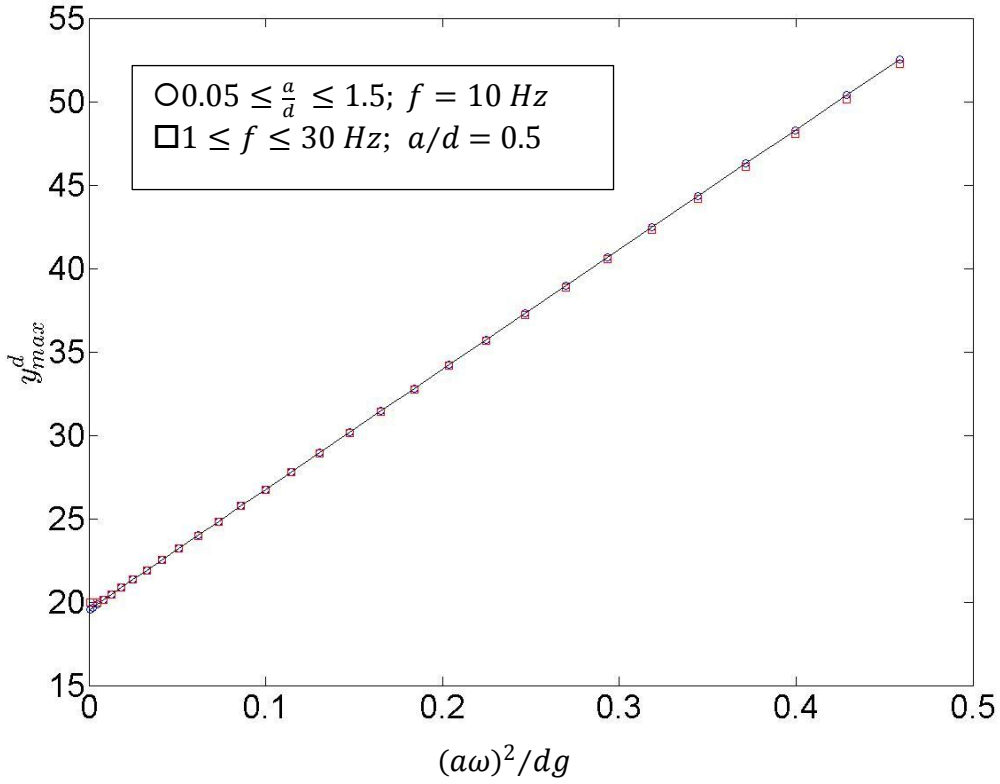

Figure 5.32 Maximum dilation of the column y^d_{max} as a function $(a\omega)^2/dg$ over the duration of a single tap of $N = 20$ spheres ($e = 0.9$) for $\bigcirc f = 10\ Hz$, $0.05 \leq a/d \leq 1.5$, and $\square a/d$ 0.5, $1 \leq f \leq 30\ Hz$. The red line through the data is a linear regression given by (equation (5.11)).

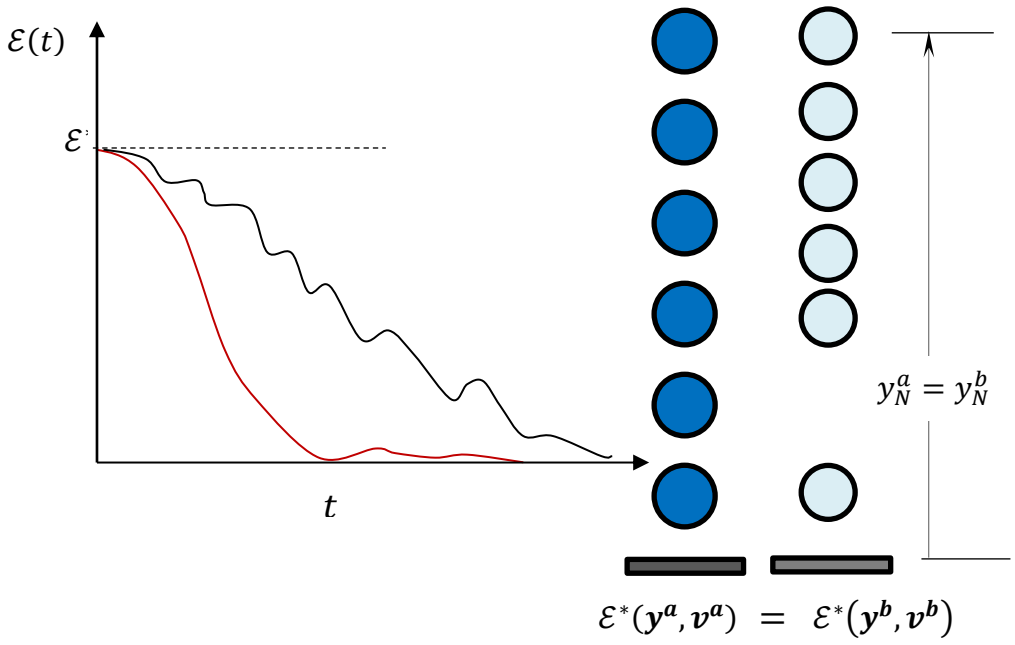

Figure 5.33 Representation of two systems having the same total energy $\mathcal{E}^*$ at time t, but at different points in phase space, $(\boldsymbol{y}^a, \boldsymbol{v}^a)$ and $(\boldsymbol{y}^b, \boldsymbol{v}^b)$. The time scale over which the system energy decays depends on the phase point.

CHAPTER 6

POINCARE MAPS OF THE MASS CENTER TRAJECTORIES

In this chapter, the dynamics of the mass center trajectory are examined via Poincaré maps extracted from the simulation data. The question that is addressed herein is whether or not the mass center of the tapped column possesses features akin to those of a single bouncing ball on an oscillating plate. Particular emphasis is placed on the influence of tap parameters (i.e., a/d, f and relaxation time t_r) on the maps with a view towards identifying periodic, period doubling and transitions to chaotic behavior. A brief discussion of the technique and how the maps are extracted from the discrete simulation data appears in the ensuing sections followed by a presentation and analysis of the results.

6.1 Introduction to Poincaré Maps

A dynamical system is comprised of a set of possible states and a function or rule that determines the evolution of the states. An easy example is an iterative map

$$x_n = f(x_{n-1}) \quad n = 1,2,3 \ldots$$

In this system, x_n are states and f is the deterministic rule. Researchers are interested in how the states evolve under this rule, with the totality of states, starting with an initial point, called the orbit. Some of the orbits are periodic, which means they are finite and cyclic, some are quasi-periodic, which means that are infinite and nearly cyclic in a certain sense and some are chaotic, which means they are definitely not cyclic – in fact, they appear to be almost randomly distributed. When f is linear the orbits always

have a very simple structure and are said to be regular, but when the function is nonlinear, chaotic orbits can occur. Chaos theory is a field that has been actively researched for the last several decades, yet there still remain many unsolved problems.

In 1890, Poincaré introduced a 2D map while he was studying the classical three-body problem of celestial mechanics. This map was obtained from the successive intersections of the trajectories of the governing differential equations with a surface in the state space under investigation. In effect, it reduced the analysis of certain properties (including periodicity) of the solution curves of the differential equations to the discrete iterates of the map. This map showed some chaotic feature which had not been understood at that time. These types of maps are now often used in the theory and applications of dynamical systems and have come to be called Poincaré maps.

Since granular flows can be viewed as dynamical systems; for example, the motion of a column of spheres stacked on top of each other and subjected to gravity as well as an applied vertical force has been studied using dynamical systems analysis by several researchers. In particular, Blackmore et al. [131, 132] constructed a discrete dynamical systems model to analyze this kind of problem. Part of this analysis used Poincaré maps to help determine the motion of the stacked spheres subjected to a periodic tapping force, after reducing the problem – at least approximately – to describing the dynamics of the center of mass of the configuration. In this case a 1D Poincaré map is created by following the position of the mass center at multiples (or submultiples) of the period of oscillation of the applied force. The deterministic rule (function) for this map is simulated using the collision force model in the DEM code that is described in Chapter 2. Up to 100 values of the vertical position of the mass center (states) are recorded by the

mass center location at the same time in each period cycle. How the map varies with tap amplitude and frequency, and the transition from periodic to chaotic dynamics thereby generated, will be discussed in this chapter.

6.2 Extracting the Poincaré Maps

Results discussed herein are for a column of 20 particles. The Poincaré map is constructed by extracting the position of the mass center over $M = 100$ taps at times that are multiples of $T = \frac{1}{2f} + t_r$, from which the influence of variations in a/d, f and t_r can

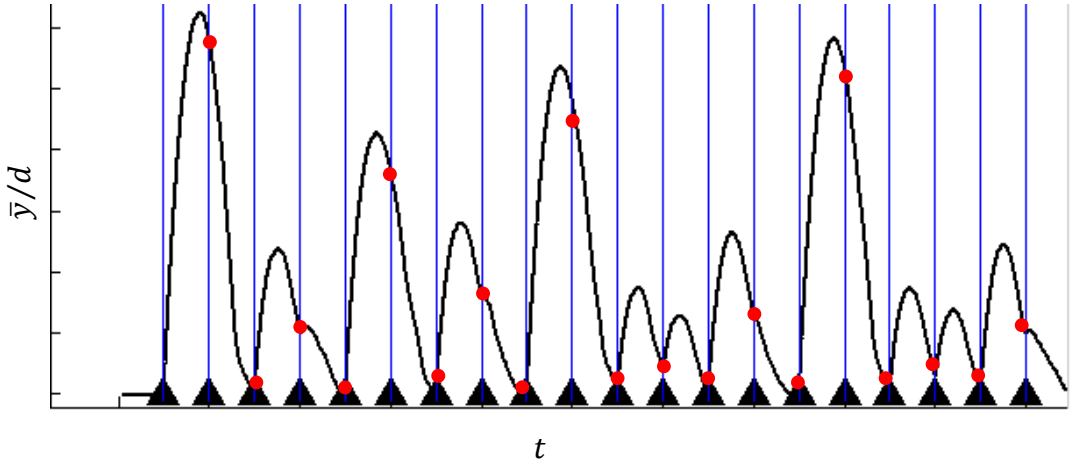

Figure 6.1 Normalized mass center $\bar{y}/d$ versus t for the first 20 taps at $a/d = 1.5$, and $f = 10\ Hz$. The vertical blue lines positioned at $\{t_1\} = 0, T, 2T, 3T, \ldots, 99T$ intersect the trajectory at points of the Poincaré map

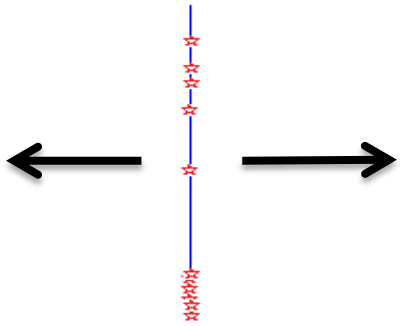

Figure 6.2 A red crosses signifies a point on the Poincaré map at $t = 0, T, 2T, \ldots, 19T$ corresponding to the red dots in Figure 7.1.

be visualized. As an example, suppose that $f = 10\,Hz$ and $t_r = 0.4\,s$ so that $T = \frac{1}{2f} + t_r = 0.45\,s$. Let $\mathcal{T} := \{t_k\}, k = 1,2,3,\ldots,100$ such that for each k, $t_k := \{(j + 0.01(k-1))T \mid j = 0,1,2,\ldots,99\}$. The mass center location is thus extracted from the discrete trajectory at $\{t_k\}$. The procedure is illustrated in Figure 6.1, in which the intersections of the vertical blue lines with the mass center trajectory are the points $\bar{y}/d$ of the map. Note that the figure shows only a small portion of the mass center trajectory. Figure 6.2 is a graphic depicting points the Poincaré map (red crosses) at $t = 0, T, 2T, 3T, \ldots, 19T$

6.3 Poincaré Map Versus Tap Amplitude

It is well-known that the behavior of a single, inelastic ball on an oscillating plate depends very strongly on the tap amplitude. Various behavioral regimes are possible –

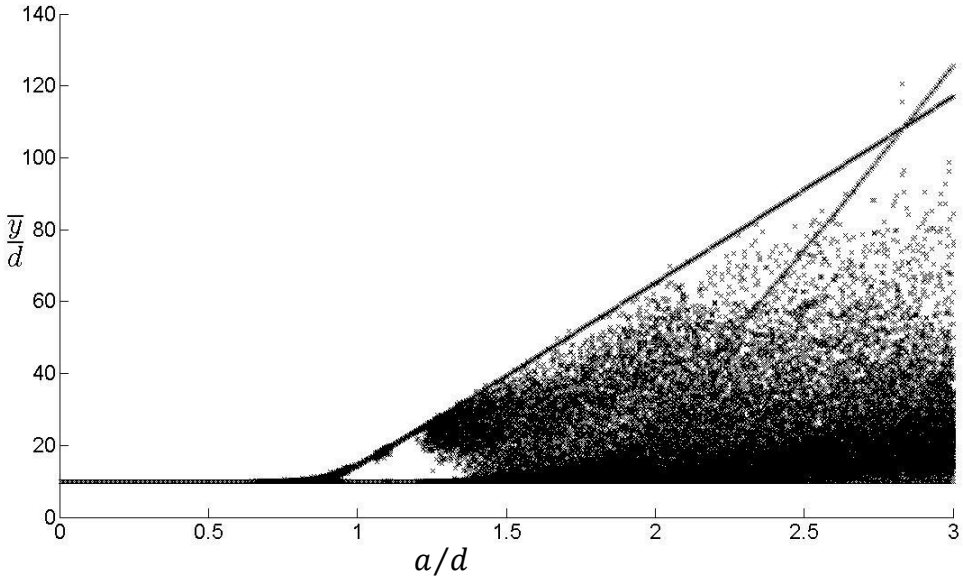

Figure 6.3 Poincaré map as a function of a/d sampled at $\{t_1\} = 0, T, 2T, \ldots, 99T$ for $f = 10\,Hz$ and $N = 20$.

from periodic solutions, period doubling and cascades to chaos. This section presents the results of an exploration of the motion of the mass center of the tapped column towards a goal of identifying similarities with the behavior of a single ball through the use of Poincaré maps. While it was not possible to identify a period-doubling cascade, findings reveal what appears to be chaotic dynamics. An initial series of studies was done with a fixed tap frequency ($f = 10\ Hz$) with a set of 600 amplitudes in ($0 < a/d \leq 3$). The bifurcation diagram (showing stable orbits) Poincaré map (Figure 6.3) sampled at $\{t_1\} = 0, T, 2T, \ldots, 99T$ of the normalized mass center at $\bar{y}/d$as a function of a/d reveals both periodic and period-doubling behavior that ultimately transitions into what appears to be chaotic dynamics. However, one also observes a maximum mass center height of $130d$, which is clearly physically unrealistic. The reason for this is a consequence of an overlap δ between colliding spheres that is much larger than would occur in reality (typically $\delta/d < 0.02$) so that the collisional impulse (as per the loading spring $K_1 \sim O(10^5)\ N/m$) effectively launches the particles. In order to check this carefully, the maximum overlap between particles was extracted by monitoring the evolution of the overlaps during a single tap for $0 < a/d \leq 3$. Figure 6.4 shows $(\delta/d)_{max}$ at $a/d = 1, 1.5, 2.\ 2.5, 3$ from which it can been seen that beyond $a/d \cong 1.5$, the normalized overlap exceeds the threshold. In particular, $(\delta/d)_{max} \cong 0.041$. Therefore, restricted tap amplitudes $0 < a/d \leq 1.5$ are used as shown in Figure 6.5. Within this range, the mass center exhibits periodic, period doubling and chaotic behaviors depending on the value of a/d.

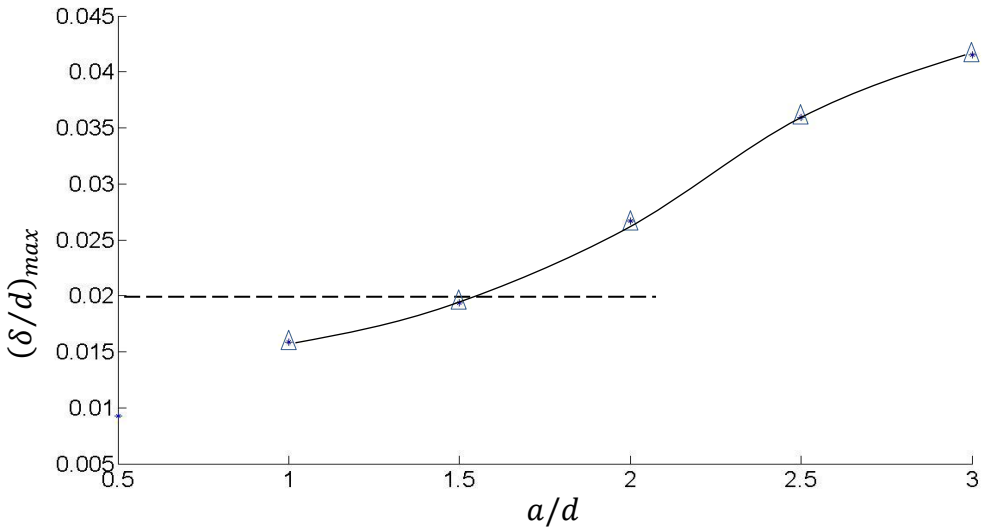

Figure 6.4 Maximum normalized overlap $(\delta/d)_{max}$ during a single tap of the column at $a/d = 1, 1.5, 2.\,2.5$ at $f = 10\ Hz$. The solid line is provided as a guide.

6.3.1 Behavioral Regimes

Studies of an inelastic ball on an oscillating plate have shown that, depending on the tap parameters (a/d and f) and e, various behaviors are possible, such as periodicity and period doubling cascades leading to chaos. While it is relatively straightforward to find at which amplitude period doubling takes place, locating other orbits (period 4, 8, etc.) is not a trivial matter. And the complexity is magnified when considering the mass center of a column as its dynamics is an average of the motion of all of the particles in the column. The difficulty is compounded by the sensitivity of the dynamics to initial conditions coupled with the need to resolve the time domain into sufficiently small intervals.

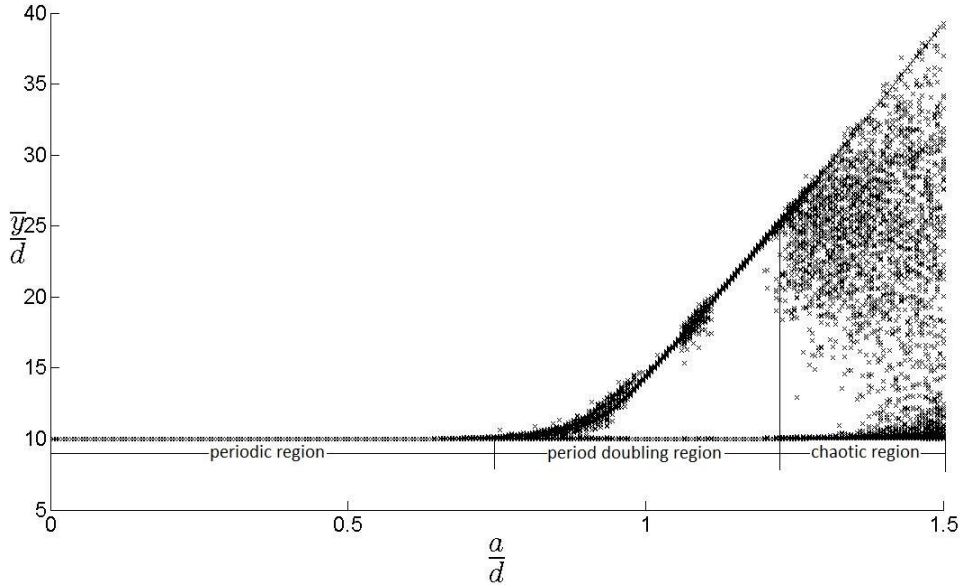

Figure 6.5 Bifurcation diagram of Poincaré map of $\bar{y}/d$ versus a/d sampled at $\{t_1\} = 0, T, 2T, \ldots, 99T$ ($N = 20$, $f = 10\,Hz$) reveals periodic, period doubling and chaotic regimes.

The map of Figure 6.5, which has been labeled to delineate these regions, shows what appears to be a single line for $0 < a/d \lesssim 0.85$, corresponding to the periodic region. (A discussion of the determination of transition values appears in Section 6.3.2). At each value of a/d in this region, there are 100 nearly identical values of $\bar{y}/d$ that correspond to the positions of the mass center at $\{t_1\} = 0, T, 2T, \ldots, 99T$. The evolution of $\bar{y}/d$ over 100 taps at $a/d = 0.5$is shown in the top half of Figure 6.6, in which the triangles on the t/T axis denote the instants of tap initiation. As the amplitude is increased, the mass center locations start to disperse until the onset of period doubling, while further increase in a/d ultimately produces what appears to be chaotic behavior. Mass center trajectories at $a/d = 1.0, 1.5$ are shown in Figures 6.7.

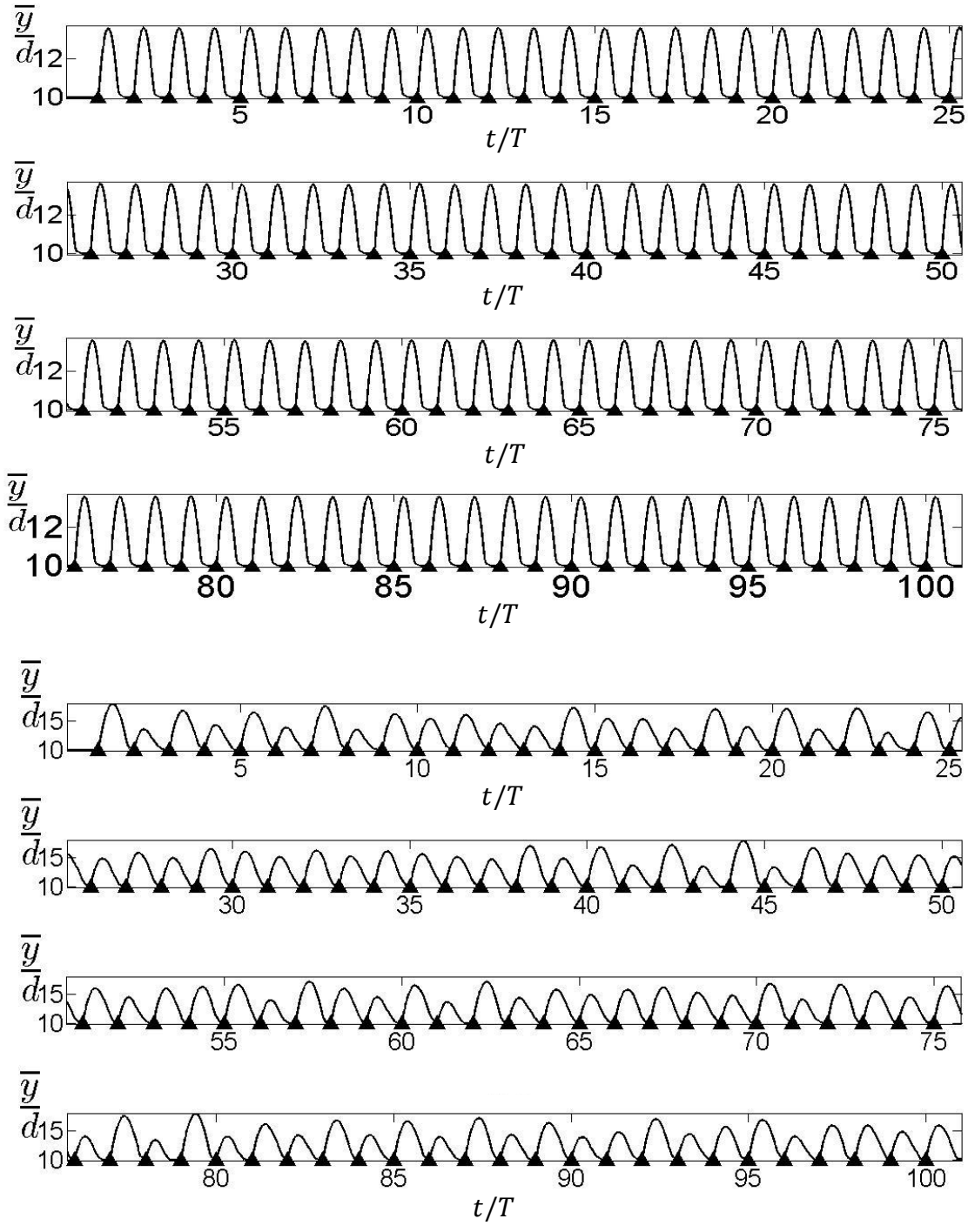

Figure 6.6 Evolution of mass center trajectory over 100 taps at $a/d = 0.5$ (top) and 0.75 (bottom). Triangles on the time axis denote the instants of tap initiation.

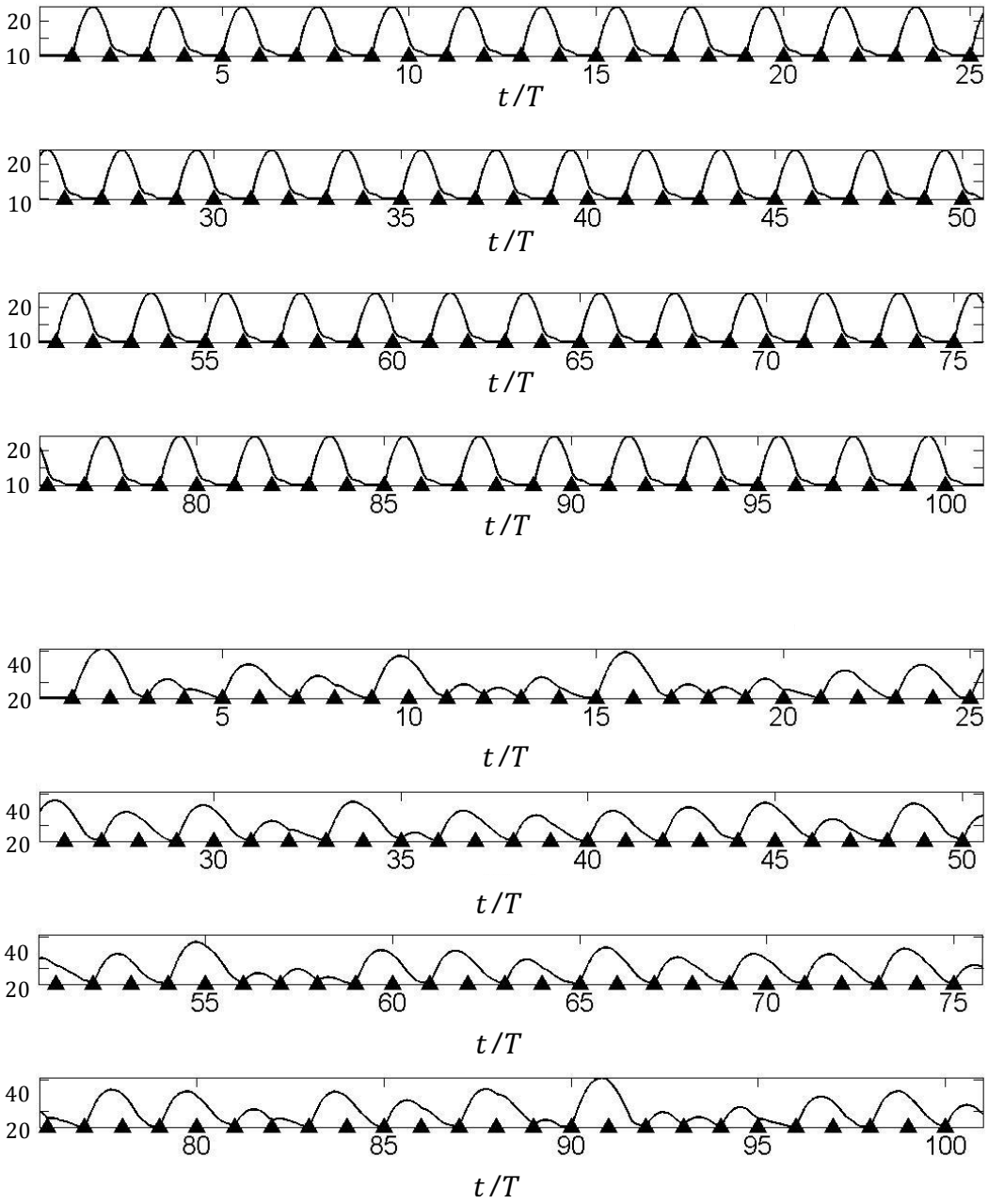

Figure 6.7 Evolution of mass center trajectory $\bar{y}/d$ over 100 taps at $a/d = 1.0$ (top) and 1.50 (bottom). Triangles on the time axis denote the instants of tap initiation.

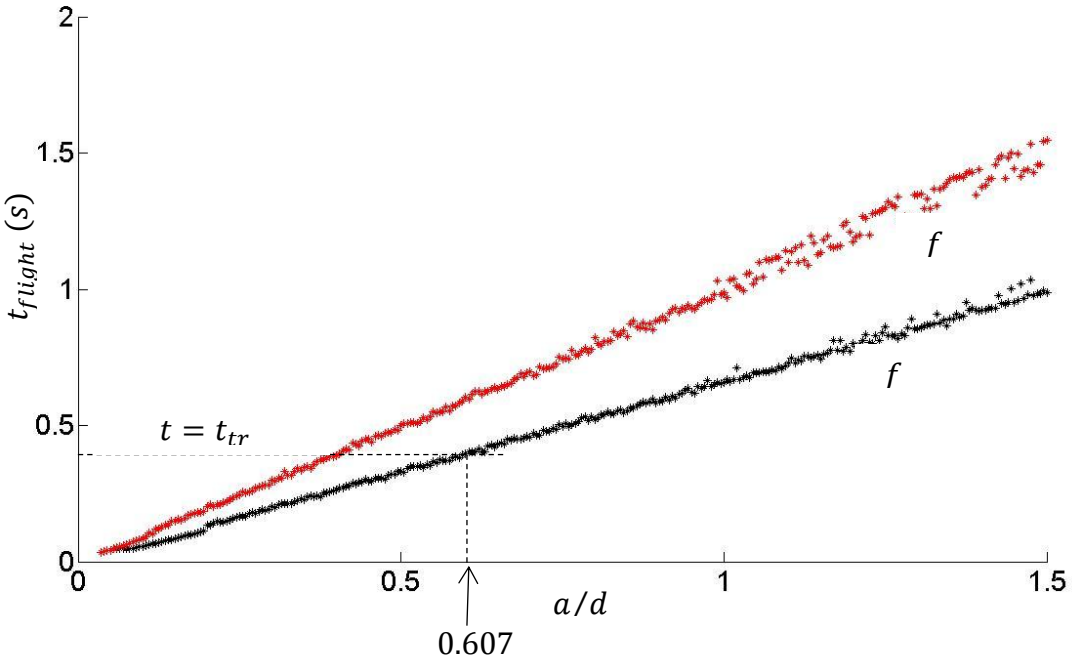

Figure 6.8 Flight time $t_{flight}\,(s)$versus a/d at $f = 10\,Hz$ (black) and $f = 15\,Hz$ (red), $N = 20$. The red line through the data points is the linear regression curve $(f = 10\,Hz) t_{flight} = c_1(a/d) + c_2$, with $c_1 = 0.6687 \pm 0.0031$ and $c_2 = -0.006105 \pm 0.002776$.

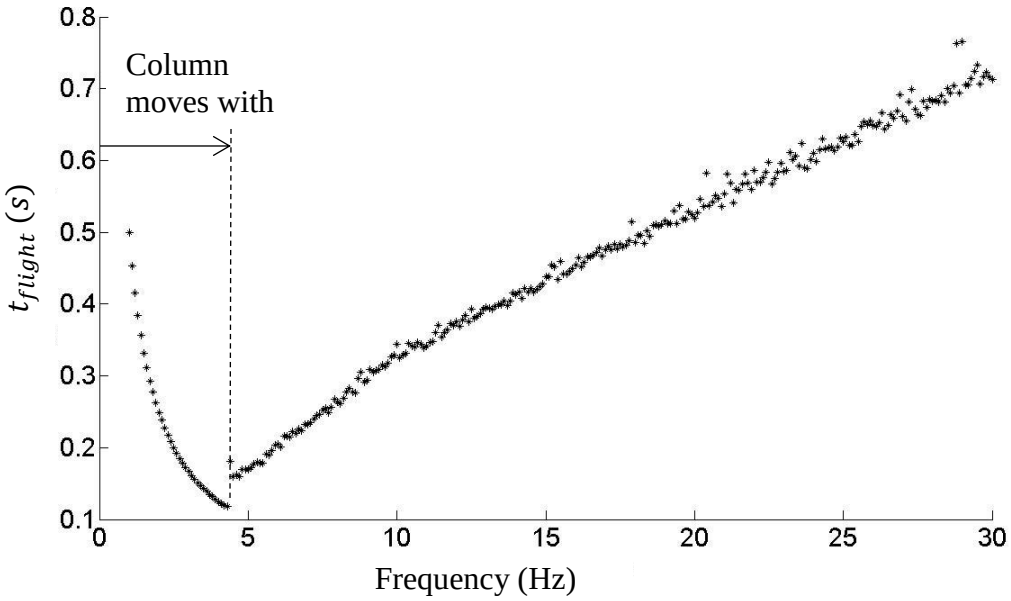

Figure 6.9 Flight time $t_{flight}\,(s)$versus frequency (Hz) at $a/d = 0.5$, $N = 20$ and $t_r = 0.4\,s$. The column moves in sync with the floor for $0 < f < 4.3\,Hz$.

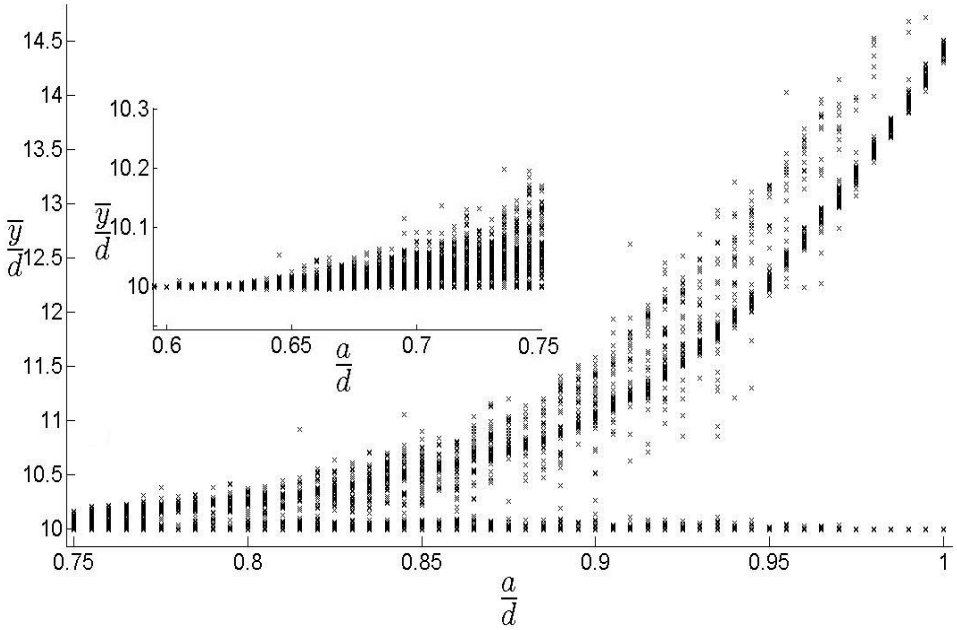

Figure 6.10 Mass center trajectory $\bar{y}/d$ as a function of a/d ($0.75 \leq a/d \leq 1.0$) at points $\{t_1\} = 0, T, 2T, \ldots, 99T$ for $t_r = 0.4\ s$ and $N = 20$. The inset shows $\bar{y}/d$ for $0.6 \leq a/d \leq 0.74$.

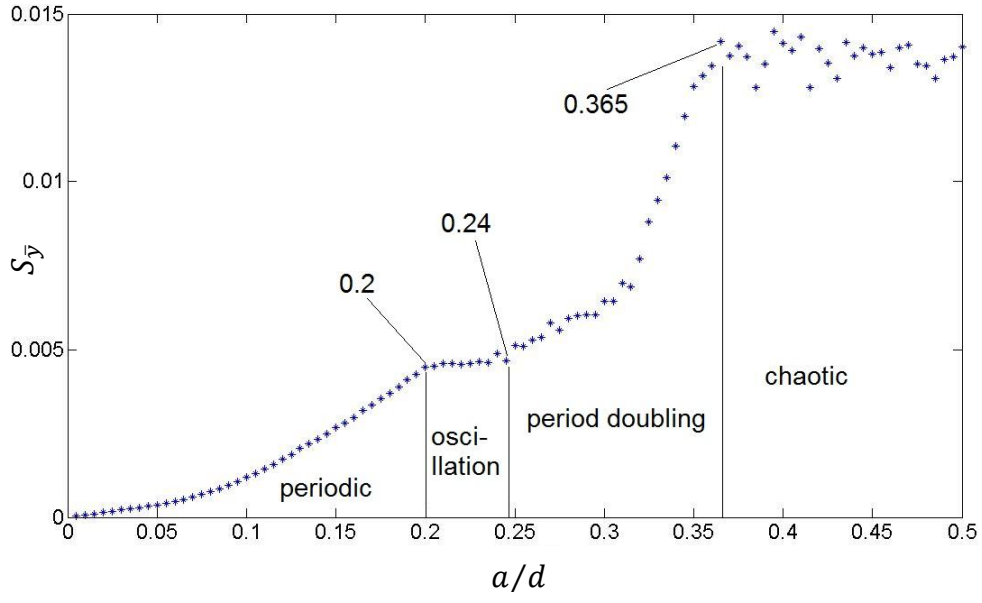

Figure 6.11 Standard deviation of the mass center $S_{\bar{y}}$trajectory (equation (6.1)) versus $a/d$for $t_r = 0.1\ s$, $f = 10\ Hz$ and $N = 20$.

The existence of the periodic, period doubling and chaotic phenomenon is understood as a 'competition' between the flight time of the mass center and the relaxation time t_r, relative to when a tap is applied. That is, for small tap amplitudes, the mass center's flight time is small compared to t_r so that it undergoes periodic motion, as is clearly visible in the trajectory at $a/d = 0.5$ of Figure 6.6.

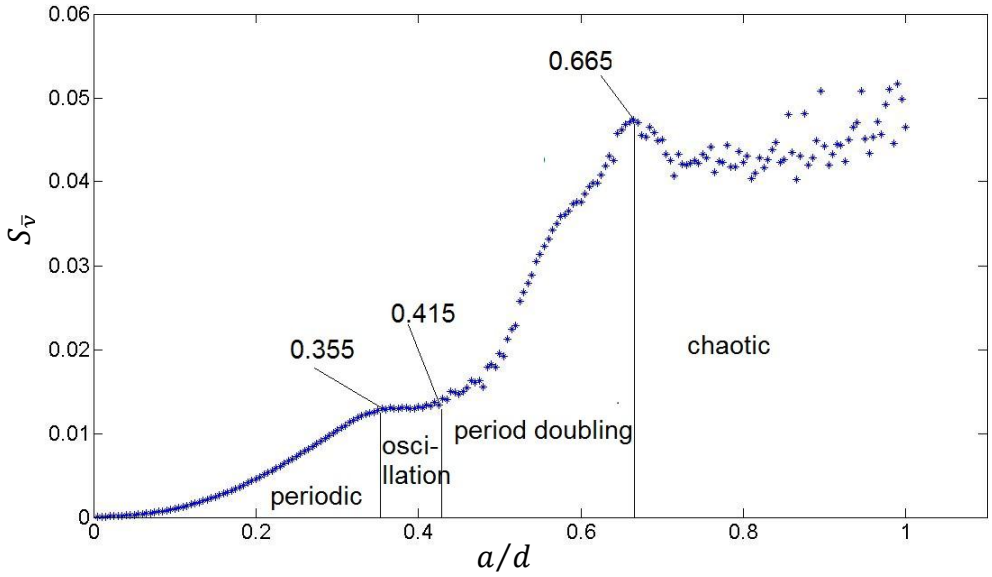

Figure 6.12 Standard deviation of the mass center $S_{\bar{y}}$trajectory (equation (6.1)) versus $a/d$for $t_r = 0.2\ s$, $f = 10\ Hz$ and $N = 20$.

A measure of the response of the column to the 'strength' of a tap (that it, the amplitude and frequency) is the *flight time* (denoted by t_{flight}). This is computed determining the time required for the mass center to return to its initial position[7] when a single tap is applied to the column of spheres. Figures 6.8 and 6.9 displays (respectively) t_{flight} versus tap amplitude a/d and frequency f for $t_r = 0.4\ s$. (i.e., for $N = 20$, $\bar{y}/d|_{t=0} \cong 10$). Note that for 'hard' spheres (i.e., no overlaps), the entire column would

7 This is mass center coordinate at the instant that the tap is applied.

move in synchronization with the floor when the tap acceleration is less than g, which corresponds to frequencies $f \leq \left(1/2\pi\sqrt{g/a}\right)$. In Figure 6.9 where $a/d = 0.5$, the flight time[8] decreases with frequency for $0 \leq f \leq 4.3$ Hz, for which the upper limit is slightly smaller than the theoretical 'hard sphere' value $f = 1/2\pi\sqrt{g/a}\big|_{a=0.5d} = 4.98$ Hz. The discrepancy between this value and the hard sphere limit is an artefact of the bilinear soft-sphere interaction model which allows energy to be stored in the system due to very small overlaps between contacting spheres as a result of gravitational forces, even when the floor is stationary.

A linear regression analysis of the data yields that $t_{flight} = c_1(a/d) + c_2$, for which $R^2 = 0.9985$, $c_1 = 0.6687 \pm 0.00$ and $c_2 = -0.006105 \pm 0.002776$. When $t_{flight} = t_r = 0.4\ s$, the regression line predicts a cut-off value $a/d = 0.607$ (illustrated

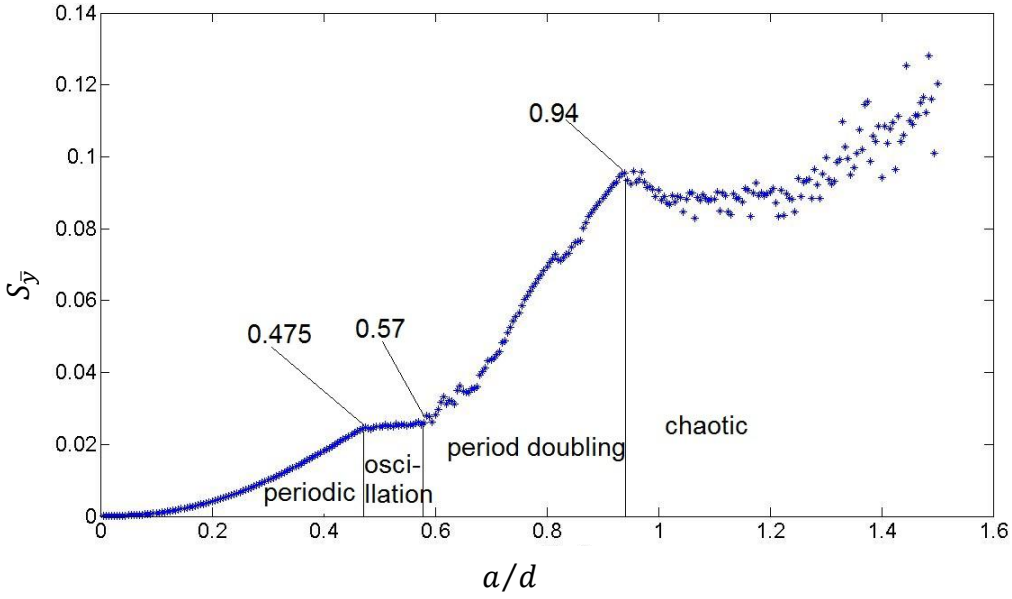

Figure 6.13 Standard deviation of the mass center $S_{\bar{y}}$trajectory (equation (6.1)) versus $a/d$for $t_r = 0.3\ s$, $f = 10\ Hz$ and $N = 20$.

8 The use of the term 'flight time' is not strictly correct here as the column moves in synchronization with the floor.

in Figure 6.8) after which $t_{flight} > t_r$. As the amplitude is increased beyond the cut-off a/d, one anticipates that at times $\{t_1\} = 0, T, 2T, \ldots, 99T$, the mass center's position will in due course begin to deviate (as t_{flight} becomes larger than t_r). This can be seen in Figure 6.10, which shows the mass center location over the range $0.60 \leq a/d \leq 1.0$. Further increases in the tap amplitude produce a flight time that is significantly longer than t_r so that taps are applied when the column is in an energetic state.

6.3.2 Identification of Behavioral Regimes

In this section, the mass center trajectory is further analyzed by determining the deviation

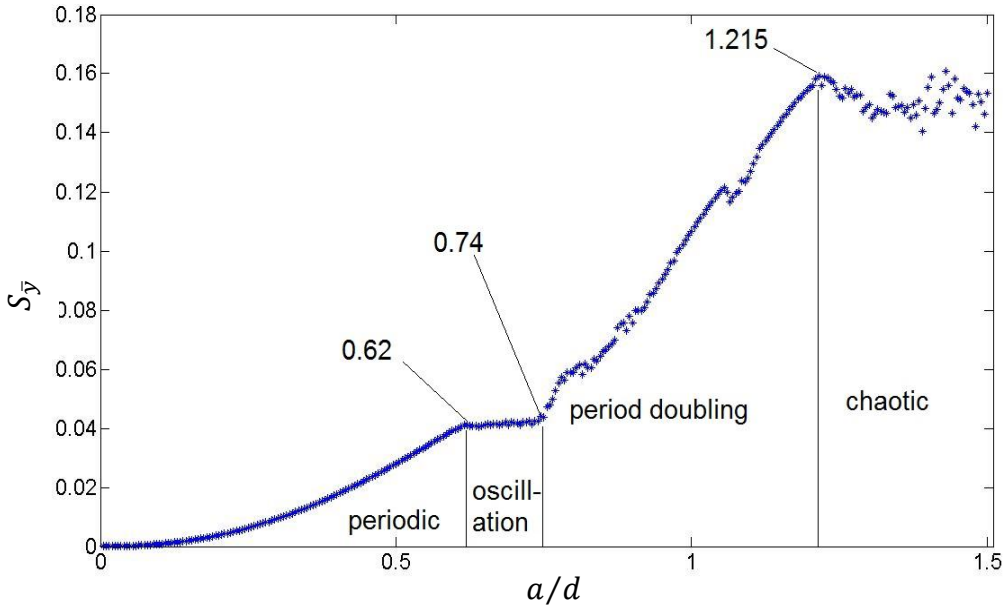

Figure 6.14 Standard deviation of the mass center $S_{\bar{y}}$trajectory (equation (6.1)) versus $a/d$for $t_r = 0.4\ s,\ f = 10\ Hz$ and $N = 20$.

from its mean value taken over the time span from when the taps begin. Calculation of the deviation, denoted by $S_{\bar{y}}$, proceeds as follows. The time duration for a tap-relaxation

cycle $[0, T]$ is partitioned into M intervals of size $\Delta t = 0.001\ s$ so that for n taps, there are Mn mass center positions $\mathcal{Y} := \{\bar{y}/d\ (k\Delta t) | \ k = 0,1,2,3, \ldots, nM\}$. Thus,

$$S_{\bar{y}} := \frac{1}{Mn}\sum_{i=1}^{nM}(\bar{y}/d\ (i\Delta t) - \langle \bar{y}/d \rangle)$$
$$\langle \bar{y}/d \rangle := \frac{1}{Mn}\sum_{i=1}^{nM}\bar{y}/d\ (i\Delta t) \tag{6.1}$$

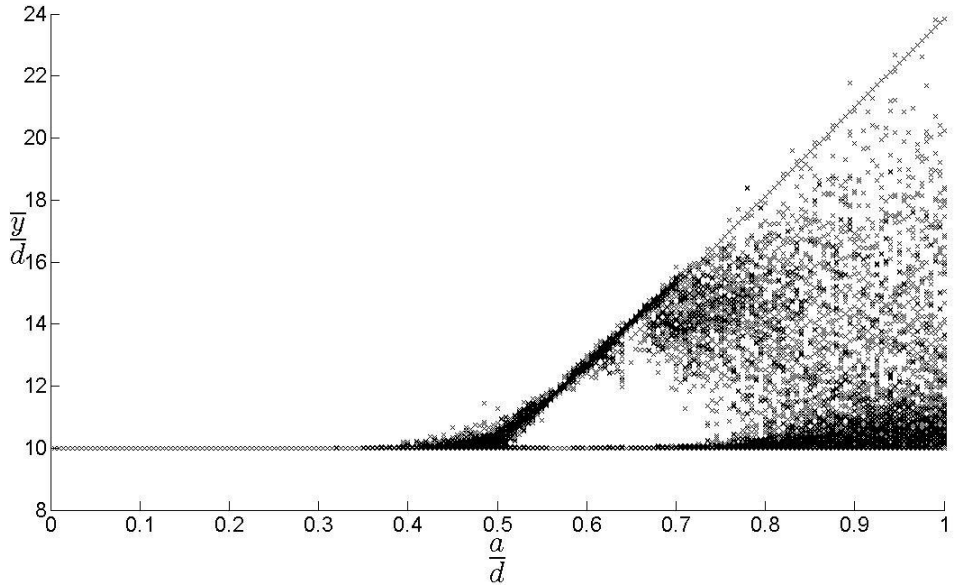

Figure 6.15 Bifurcation diagram for Poincaré map for $t_r = 0.2\ s$, $f = 10\ Hz$ at $\{t_1\} = 0, T, 2T, \ldots, 99T$, $N = 20$.

Figures 6.11 – 6.14 present (respectively) $S_{\bar{y}}$ versus a/d for $t_r = 0.1,\ 0.2,\ 0.3,\ 0.4\ s$ Each of the graphs have similar characteristics. There is a *periodic* region in which $S_{\bar{y}}$ increases with a/d due to the column experiencing greater dilation (reflected in the

graph of t_{flight} vs. a/d in Figure 6.8). A flat transition region entitled oscillation follows, which is viewed as a transition separating periodic dynamics from the ensuing *period doubling* behavior where $S_{\bar{y}}$ continues to rise with a/d. The last region where $S_{\bar{y}}$appears to undergo a very small decrease and slight upturn with oscillations corresponds to chaotic dynamics. The latter results suggest that one it possible to roughly delineate the regions of periodic, period-doubling and chaotic behavior from the graph of $S_{\bar{y}}$ versus a/d. This study leads to the matter of the next section – an examination of how a change in relaxation time t_r affects the Poincaré map. As was done previously, for each t_r, the tap amplitude was varied over a discrete set of values in $(0 < a/d \leq 1.0)$.

6.3.3 Influence of Relaxation Time on Poincaré Map

The Poincare map for the case when $t_r = 0.2\,s$ for $0 < a/d \leq 1$ and $f = 10\,Hz$ is shown in Figure 6.15 reveals periodic, period-doubling and chaotic regions as was seen in the case when $t_r = 0.4$, albeit the transitions occur at different values of a/d. The maps for $t_r = 0.4$ and $t_r = 0.2$ plotted together in Figure 6.16 suggests that the map

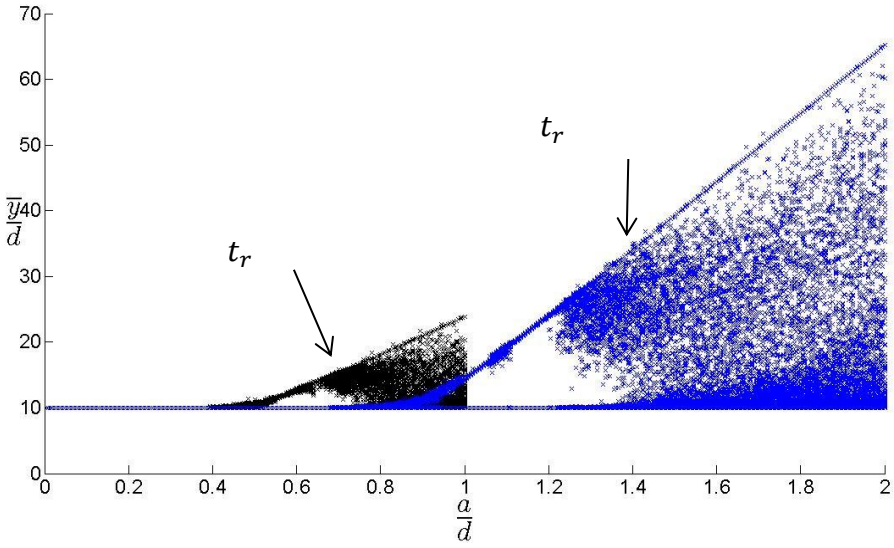

Figure 6.16 Bifurcation diagrams for Poincaré maps for $t_r = 0.2\,s, 0.4\,s$, at $\{t_1\} = 0, T, 2T, \ldots, 99T$, $N = 20$ and $f = 10\,Hz$.

corresponding to $t_r = 0.2$ is simply scaled down. This can be seen more clearly from the

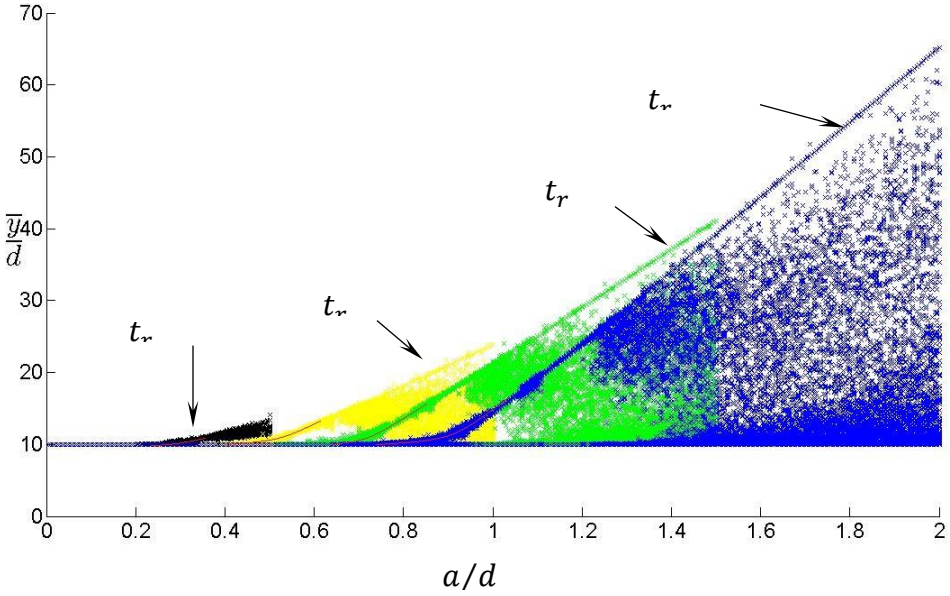

Figure 6.17 Poincaré maps for $t_r = 0.1, 0.2, 0.3, 0.4\ s$, $f = 10\ Hz$ sampled at $\{t_1\} = 0, T, 2T, \ldots, 99T$, $N = 20$.

Poincare maps for relaxation times $t_r = 0.1,\ 0.2,\ 0.3,\ 0.4\ s$ in Figure 6.17.

The Poincaré map of a single ball on an oscillating plate exhibits the full gamut of dynamical regimes – from periodicity to chaos. In particular, there is a period-doubling cascade that leads to chaotic dynamics. As was noted earlier in this chapter, because the the mass center dynamics is an average motion of all of the particle in the column, a determination of the parameters (a/d and f) triggering the onset of the period-doubling cascade is problematic at best. The difficulty is further compounded by the sensitivity of the dynamics to initial conditions coupled with the need to resolve the time domain into sufficiently small intervals. It was demonstrated in the previous section that the graph of the deviation of the mass center trajectory $S_{\bar{y}}$ versus a/d exhibited demarcations in behavior that roughly corresponded to the transition points for periodic, period-doubling

and chaotic dynamics. Table 6.1 presents the transition point results displayed on Figures 6.11 – 6.14.

Table 6.1 Poincaré Map Transition Points

	Periodic - Transition	Transition – Period Doubling	Period Doubling - Chaos
$t_r = 0.1$	0.20	0.24	0.365
$t_r = 0.2$	0.355	0.415	0.665
$t_r = 0.3$	0.475	0.570	0.940
$t_r = 0.4$	0.620	0.740	1.215

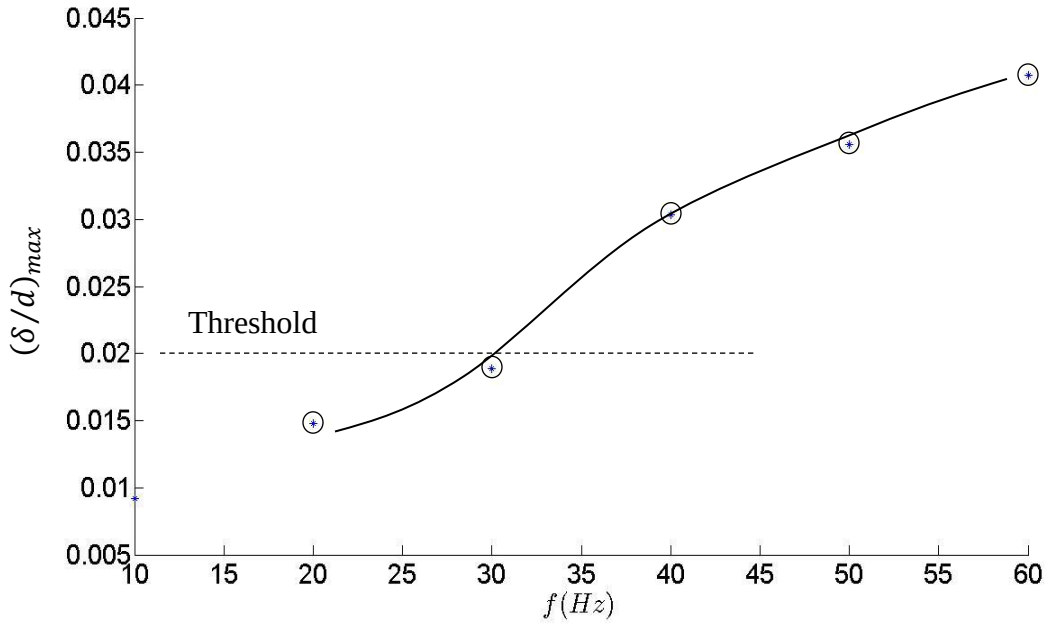

Figure 6.18 Maximum normalized overlap $(\delta/d)_{max}$ during a single tap of the column ($N = 20$) at $f = 20, 30, 40\ 50\ Hz$ and $a/d = 1.0$. The solid line is provided as a guide.

6.4 Poincaré Map Versus Tap Frequency

The behavior of the Poincaré map as a function of frequency for a fixed tap amplitude $a/d = 0.50$ is shown in Figure 6.18 for $0 < f \leq 30\ Hz$. It was found that at frequencies larger than the $30\ Hz$ upper bound, nonphysical overlaps between particles, resulting in very large repulsive forces and thus unrealistic displacements. As corroboration, the maximum overlap between particles $(\delta/d)_{max}$was extracted by monitoring the evolution of the overlaps during a single tap for $0 < f \leq 50\ Hz$. Figure 6.18 presents $(\delta/d)_{max}$ versus f at $a/d = 1.0$? from which it can been seen that for $f \gtrsim 30\ Hz$, $(\delta/d)_{max}$ exceeds the threshold. Within the frequency range $0 < f \leq 30\ Hz$, the mass center exhibits periodic, period doubling and chaotic behaviors depending on

the value of f as seen in Figure 6.19. As per equation (6.1), the deviation of the mass center's motion $S_{\bar{y}}$ is computed and plotted as a function of frequency for $a/d =$

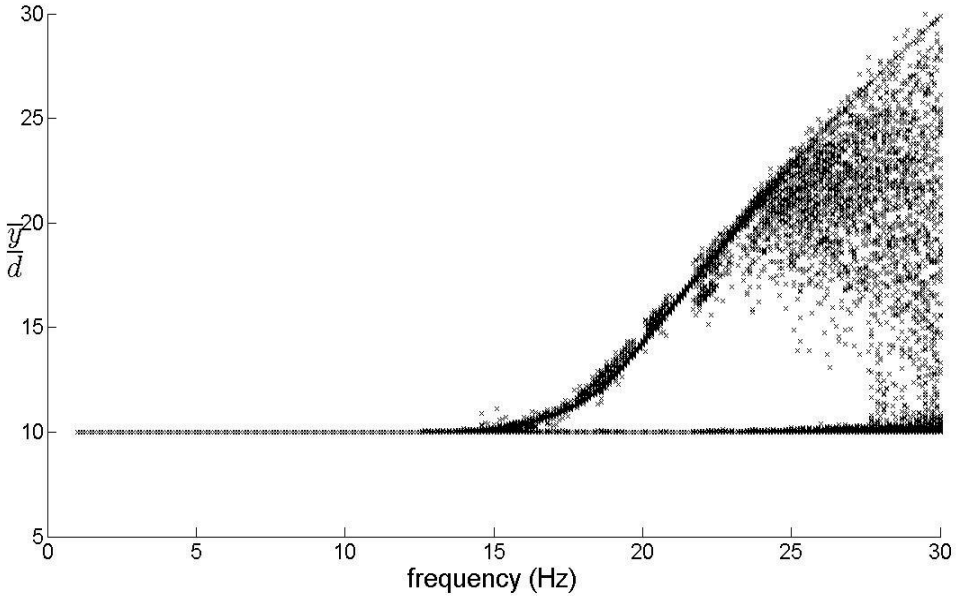

Figure 6.19 Bifurcation diagram of Poincaré map sampled at $\{t_1\}$ of the mass center trajectory at $a/d = 0.5$ versus frequency for $N = 20$.

1.0 and $N = 20$, the result of which is shown in Figure 6.20. One observes again (as in Figures 6.11 – 6.14) that the graph of $S_{\bar{y}}$ versus f exhibits distinct regions delineating periodic, transition, period doubling and chaotic dynamics.

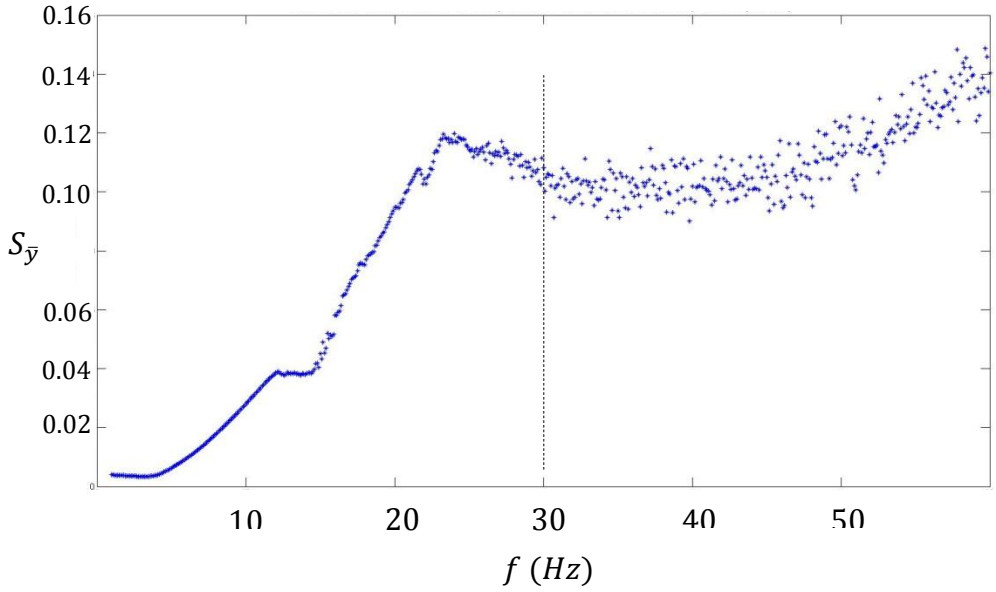

Figure 6.20 Standard deviation of the mass center $S_{\bar{y}}$trajectory (equation (6.1)) versus f for $t_r = 0.4\ s,\ 0 < f \leq 50\ Hz$ and $N = 20$.

6.5 Evolution of Poincaré Map – Shifting the Sampling Times

Up to this juncture, the discussion has been restricted to Poincaré maps constructed by extracting mass center positions sampled at $\{t_1\} = \{0, T, 2T, 3T, \dots, 99T\}$. In this section, inspection points $\{t_k\} := \{(j + 0.01(k-1))T \mid j = 0,1,2, \dots, 99\}, k = 1, 2, \dots, 100$are used so that 100 *incremental* Poincaré maps are generated (one map for each k). By sweeping through the tap-relaxation time interval in this manner, one is able to obtain a superficial portrait of the evolving dynamics of the system. The result of this procedure for $f = 10\ Hz,\ t_r = 0.4\ s$ and $T = 0.45\ s$ produces maps spaced at $0.0045\ s$intervals.

Figure 6.22 depicts a subset of the generated maps at sampling sets $\{t_1\}, \{t_{10}\}, \{t_{20}\}, \ldots, \{t_{90}\}$, from which several observations can be made. Each map of the figure features an amplitude interval (that varies with the inspection set $\{t_k\}, k = 1, 2, 3, \ldots, 100$) in which the mass center exhibits periodic motion. At sampling set $\{t_1\}$, the region of periodicity appears as a horizontal line. (A detailed discussion of this region was given in Sections 6.3.1, 6.3.2). As the mass center location is charted at later times in its trajectory, corresponding to sampling times $\{t_2\}, \{t_3\}, \{t_4\}$ ..., the horizontal line begins to acquire a constant positive slope over an interval of tap amplitudes a/d through which the dynamics remain periodic. This slope is in concert with the results of Figure 6.8, where the flight time was observed to increase in proportion to a/d. Another common feature of the maps is the emergence of period doubling dynamics as evidenced by a bifurcation of the mass center trajectory over a/d intervals that depend on the inspection times $\{t_k\}, k = 1, 2, 3, \ldots, 100$. One also sees evidence of periodic to period-doubling cascades that return to stabile period-2 orbits. For example, consider the map obtained at inspection points $\{t_{50}\}$, which is shown as an enlarged view in Figure 6.21. Here, one sees the periodic regime for $0 < a/d \lesssim 0.60$, followed by a thickening of the map that suggests a cascade with a return to a period-2 (bifurcation) orbit. Analogous dissections can be conjectured from the other maps depicted in Figure 6.22. Complete confirmation of the dynamics conjectured here will necessarily require a CPU-intensive scrutiny of the system that focuses on isolating the various dynamical regions to actually map the cascades and transitions.

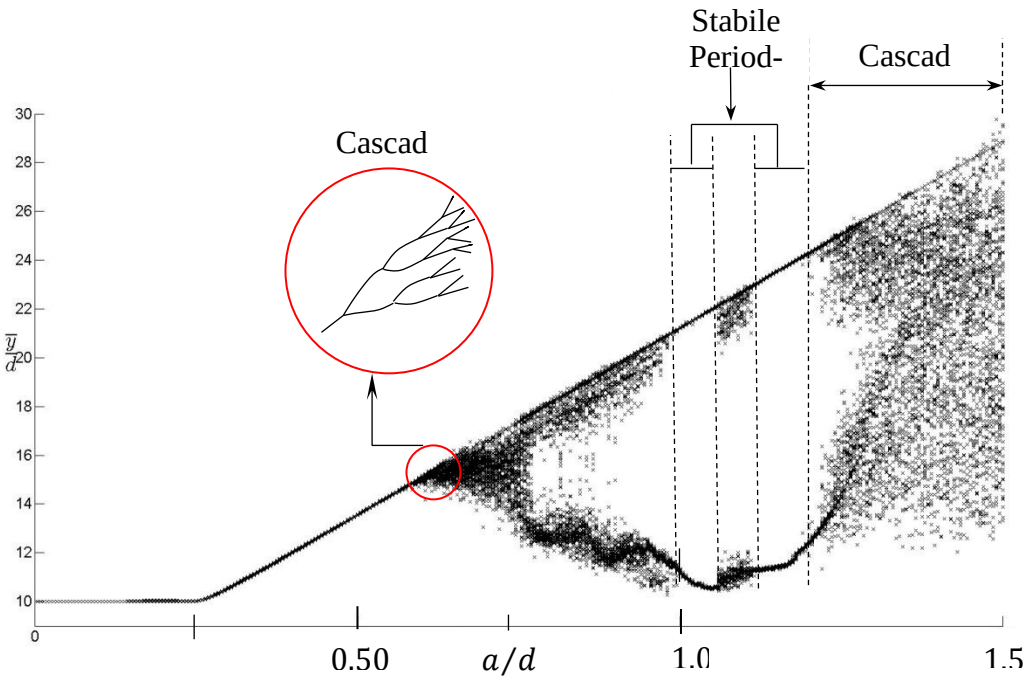

Figure 6.21 Bifurcation diagram of incremental Poincaré map of the mass center trajectory $\bar{y}/d$obtained from inspection points $\{t_{50}\}$ at $f = 10\ Hz$ as a function of tap amplitude a/d.

6.6 Dilation Map

Another signature of the column's dynamics can be acquired by the evolution of the column's dilation, i.e., $\Delta(t; a/d) := \big(y_{20}(t) - y_1(t)\big)/d$, where a/d is regarded as a parameter. Here, y_{20} and y_1 are the locations of the centers of the first and top particles in the column. A Poincaré map of Δ can be constructed in the same manner as was done

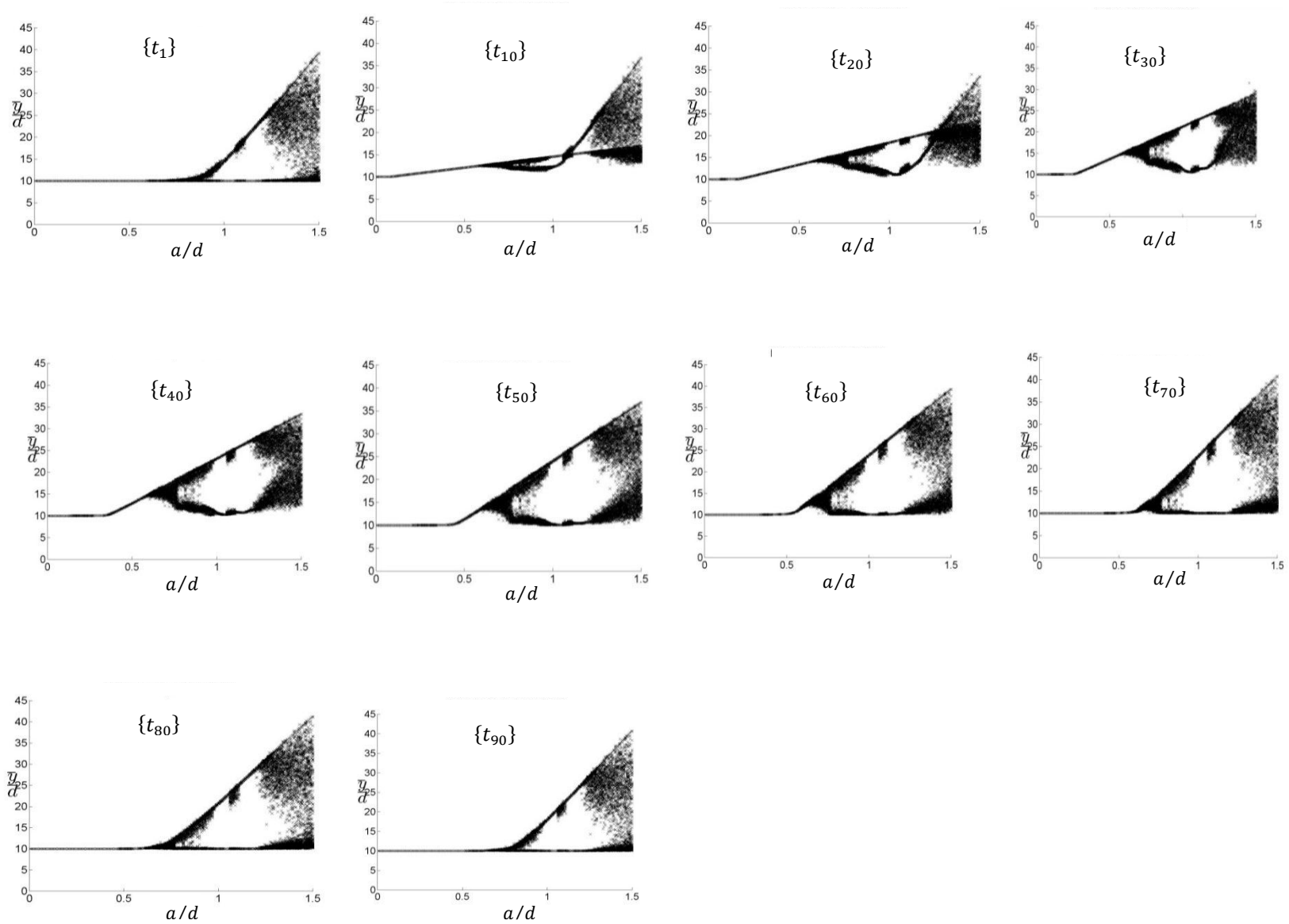

Figure 6.22 Poincaré maps of the mass center trajectory $\bar{y}/d$at $\{t_1\}, \{t_{10}\}, \{t_{20}\}, \{t_{30}\}, \dots, \{t_{90}\}$ for $f = 10\ Hz$, $t_r = 0.4\ s$, $N = 20$.

for the mass center. Intuitively, one expects that Δ increases with a/d (for a fixed frequency), and that there is a threshold value of a/d below which the column experiences no dilation. (Here the column simply moves in unison with the floor). Figure 6.23 shows a Poincaré map (sampled at $\{t_1\}$) of the dilation as a function of a/d at $f = 10\ Hz$. The dynamic behavior of the column that is portrayed in the dilation map is not understood (in the same manner as those of the mass center) so that further study is required.

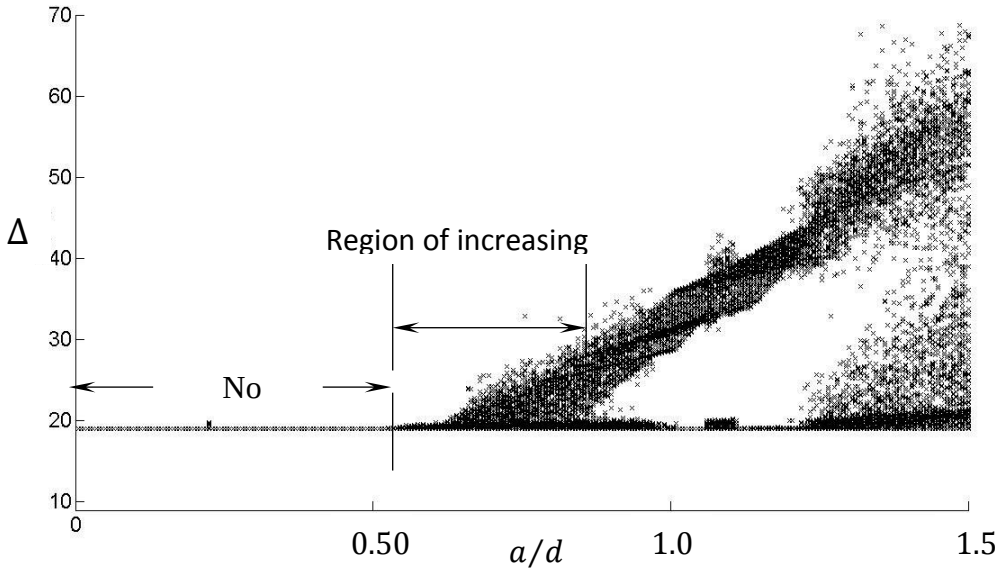

Figure 6.23 Dilation (Δ) map sampled at $\{t_1\}$ and $f = 10\ Hz$.

6.7 Reduced Relaxation Map

As suggested earlier in this chapter, the features of the Poincaré map revealing periodic, period doubling, cascades and chaotic dynamics are deemed to be a consequence of the

difference between the relaxation time t_r (i.e., interval between taps) and the flight time t_{flight} of the column mass center. For fixed t_r, the flight time will increase with amplitude or frequency as shown in Figures 6.8 and 6.9, and when $t_r > t_{flight}$, the mass center trajectory will shift away from periodicity to period-doubling cascade, ultimately leading to chaos. In order to demonstrate this phenomenon in a rough manner, the Poincare map is constructed at $a/d = 0.5, f = 10\ Hz$ for $0 \leq t_r \leq 0.4\ s$, with the lower limit corresponding to continuous half-sine pulses. Thus, a fixed flight time is (by Figure 6.8) found to be $t_{flight} = c_1(a/d) + c_2 = 0.6687(0.5) - 0.00615 = 0.3282\ s$. The result is shown in Figure 6.24 for 100 taps at inspection times $\{t_1\}$. What is significant is that as $t_r \to 0$, one observes that the dynamics evolves, starting with periodic behavior and transitioning to chaos.

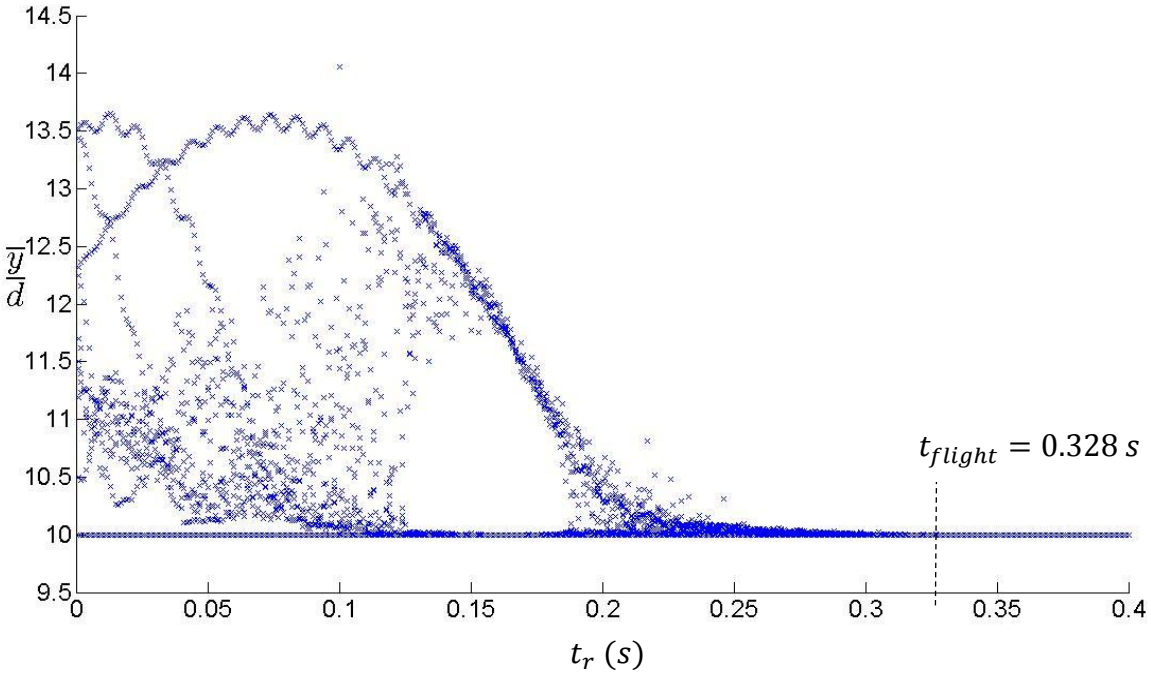

Figure 6.24 Bifurcation diagram of incremental Poincaré map at inspection points $\{t_1\}$generated from 100 taps as a function of relaxation time t_r at $a/d = 0.5$, $f = 10\ Hz$.

CHAPTER 7

SUMMARY AND SOME IDEAS FOR CONTINUED RESEARCH

This chapter presents a summary of the dissertation and some ideas for continued research on related granular flow problems.

For the most part, this dissertation has been divided into two parts, one is the analysis of short time scale motion and the other is that of long time scale dynamics.

7.1 Brief Summary and Conclusions

In the short time scale part, the main focus is on understanding how various perturbation and deformation waves propagate through the column using the DEM model. The speed of these waves is measured and the results are compared with the predictions of related linear wave theory. It is found that the simulations compare quite well with the theory. Then the affects of varying tap and material parameters on the wave propagation dynamics and properties are studied in considerable detail and comparisons with theory are made where possible and insightful.

In the long time scale part, the research is focused on the whole process of the column motion, and in particular, how it behaves as a pulse is exerted on one end (usually the bottom) of the column in the presence of a gravity force field. The response to the applied force (pulse) starts with an expansion with the particles flying upward and apart and ends with a cooling process of the column settling down to a nearly equilibrium state. Chapter 4 and Chapter 5 discussed the expansion process and cooling processes in considerable detail, respectively, and various conclusions and conjectures were made

about how the dynamics, density and energy of the configuration depend on the material properties, initial position of the stacked spheres, and the tap parameters. Some conclusions reached are listed below:

- Increasing amplitude and frequency will increase the energy and column expansion
- Smaller restitution coefficients and larger numbers of particles will dissipate the expansion faster and increasing the cooling effect

Then in Chapter 6, the column is represented as a dynamical system, and the dynamical behavior is investigated in great detail. A useful tool called a Poincaré map is employed to describe this dynamical system and some important features of the motion are identified using this approach. If the controlling relaxation time is held fixed, the column motion typically follows a periodic to period doubling to period doubling cascade to chaotic progression as the tap energy increases. If the tap amplitude and frequency are fixed constants, then reducing the relaxation time will result in the same period doubling cascade to chaos sequence of dynamics.

7.2 Some Ideas for Continuous Research

There are still some elements that will affect the dynamics of the column that have not yet been completely investigated. For instance, the overall dependence of the dynamical behavior of the stacked spheres on particle size, sphere density and material stiffness is still largely unknown. These parameters are included in the DEM code and have certainly been observed to change the dynamics of the system. There is some work that needs to be done to determine just how these parameters affect the dynamics. Also, the Poincaré map needs to be investigated more thoroughly to determine precisely how such parameters as the number of particles and restitution coefficients influence the discrete dynamics of the

iterates. There is also much that remains to be learned about the dynamics in parameter regions associated with the end of period doubling cascades and the initiation of chaos. For the short time scale part, it is important to study how the dynamics is affected by the nature of the particle-particle and particle-boundary interaction force model is used in the simulations and mathematical treatments. In particular, it is quite possible that if one uses the Hertz model or FEM model (ABAQUS), it might be easier to analyze the wave propagation and the results might compare better with results from other theoretical approaches and some available experimental studies. Also, it remains to extend the analysis to 2D or 3D particle configuration by modifying the tangential force model and applying the rolling effect into the system.

APPENDIX A

MATLAB CODE TO GENEARATE INPUT FILES

This appendix gives the MATLAB code to generating initial input files i3ds.

```
% for i = 1:5
    for i = 1:30
%         for j = 1:3
    disp(['starting',num2str(i),' Hz']);
% fid = fopen(['J:\matlab
environment\Aw\A',num2str(0.01*i),'f',num2str(10*j),'\i3ds'],'wt');
% fid = fopen(['J:\matlab
environment\Falcon\exp2\',num2str(i),'\i3ds'],'wt');
fid = fopen(['E:\matlab
environment\generate_i3ds\freq\',num2str(i),'\i3ds'],'wt');
%fid=fopen(['I:\matlab
environment\freq\longrelax\1tapfreq\',num2str(i),'\',num2str(i),'.txt']
,'wt')
fprintf(fid,'\n s3dsNEwb i3ds343b particles  30.00deg  n=47
n/mm=.55294 drag=0.0 z=6.7mm\n');
fprintf(fid,'fmub=0.25  fmu=0.1\n\n');

fprintf(fid,[' &var  np =          ',num2str(20+5),'      /Total number
of particles in cell\n']);
fprintf(fid,' &var  bdry =         1      /flag for boundry type
(1;cubic, 2;tringular)\n');
fprintf(fid,' &var  nxby0 =        1      /No of boundary particles in
x-dir. at y = 0\n');
fprintf(fid,' &var  nzby0 =        1      /No of boundary particles in
z-dir. at y = 0\n');
fprintf(fid,' &var  nxby1 =        0      /No of boundary particles in
x-dir. at ycell\n');
fprintf(fid,' &var  nzby1 =        0      /No of boundary particles in
z-dir. at ycell\n');
% fprintf(fid,'\n');
% fprintf(fid,'\n');
% fprintf(fid,'\n');
fprintf(fid,' &var  nxbz0 =        1      /No of boundary particles in
x-dir. at z = 0\n');
fprintf(fid,' &var  nybz0 =        1      /No of boundary particles in
y-dir. at z = 0\n');
fprintf(fid,' &var  nxbz1 =        1      /No of boundary particles in
x-dir. at zcell\n');
fprintf(fid,' &var  nybz1 =        1      /No of boundary particles in
y-dir. at zcell\n');
fprintf(fid,' &var  nybx0 =        1      /No of boundary particles in
y-dir. at x = 0\n');
fprintf(fid,' &var  nzbx0 =        1      /No of boundary particles in
z-dir. at x = 0\n');
```

```
fprintf(fid,' &var  nybx1 =        1      /No of boundary particles in
y-dir. at xcell\n');
fprintf(fid,' &var  nzbx1 =        1      /No of boundary particles in
z-dir. at xcell\n');
fprintf(fid,' &var  nfix =         0      / number of fixed
particles\n');
fprintf(fid,' &var  nzcyl =        0      / number of fixed cylinders
parallel to z-axis\n');
fprintf(fid,' &var  nycyl =        0      / number of fixed cylinders
parallel to y-axis\n');
fprintf(fid,' &var  ncmax =        0      /number of collisions during
entire run\n');
fprintf(fid,' &var  nout =         0      /No. of time to print out
results\n');
fprintf(fid,' &var  nczero =       0      /number of collisions before
start cum. ave.\n');
fprintf(fid,' &var  ntcol =       69      /number of time steps during
a collision\n');
fprintf(fid,' &var  nvel =        20      /number of intervals for vel.
distrib.\n');
fprintf(fid,' &var  nyzone =      48      /number of y zones\n');
fprintf(fid,' &var  mzcell =      4       /\n');
fprintf(fid,' &var  nycell =      10      /\n');
fprintf(fid,' &var  itervm =       1      /max iterations per time
step\n');
fprintf(fid,' &var  icoord =       0      /flag for coordinates print
out\n');
fprintf(fid,' &var  itty =         0      /flag for tty
interaction\n');
fprintf(fid,' &var  ixyz =         0      /flag to read init coords of
fxd & bnd particles\n');
fprintf(fid,' &var  istart =       0      /to restart the code rename
d3ds to d3ds1000 and set istart=1000\n');
fprintf(fid,' &var  tmax =       750      /max time for
calculation\n');
fprintf(fid,[' &var  tpour =  ',num2str(2),'         /time for
pouring\n']);
fprintf(fid,' &var  dt =         0.       /time step\n');
fprintf(fid,' &var  dtout =      0.001    /time interval for printing
out results\n');
fprintf(fid,' &var  dtdump =     0.1      /time interval for
dumping\n');
fprintf(fid,' &var  tzero =      0.25     /restart long-term cum.
ave.\n');
fprintf(fid,' &var  search =   0.001      /search distance for near
neighbors\n');
fprintf(fid,' &var  ycell =    1          /cell height (m) \n');
fprintf(fid,' &var  xyrat =    0.019999   /ratio used to compute xcell
\n');
fprintf(fid,' &var  zyrat =    0.019999   /ratio used to compute zcell
\n');
fprintf(fid,' &var  vave =     0.0        /average deviatoric transl.
velocity\n');
fprintf(fid,' &var  vseed =    0.9        /seed for random initial
particle velocities\n');
fprintf(fid,' &var  vxzero =   0.0        /initial velocity in the x-
direction (ave)\n');
```

```
fprintf(fid,' &var  vyzero =  0.0         /initial velocity in y-
direction (ave)\n');
fprintf(fid,' &var  vzzero =  0.0         /loading stiffness K1\n');
fprintf(fid,' &var  skn1 =     2.8e+05     /normal force
coefficient\n');
fprintf(fid,' &var  elast =   0.92        /coefficient of
restitution\n');
fprintf(fid,' &var  slope =   1.0e+05     /alternative parameter for
unloading\n');
fprintf(fid,' &var  ratk =    0.8         /ratio of tangential/normal
stiffness\n');
fprintf(fid,' &var  fmu =     0.1         /coefficient of friction\n');
fprintf(fid,' &var  fmub =    0           /friction for boundary and
fixed particles\n');
fprintf(fid,' &var  power =   0.3333333   /tangential force
exponent\n');
fprintf(fid,[' &var  rmassz =  ',num2str(5026),'        /mass of unit
sphere\n']);
fprintf(fid,' &var  tstart=   0.0         /\n');
fprintf(fid,' &var  gravx =   0.0         /acceleration of gravity in x
direction\n');
fprintf(fid,' &var  gravy =   -9.81       /acceleration of gravity in y
direction\n');
fprintf(fid,' &var  gravz =   0.0         /acceleration of gravity in z
direction\n');
fprintf(fid,' &var  vxby0 =   0.0         /x velocity of real boundary
at y = zero\n');
fprintf(fid,' &var  vxby1 =   0.0         /x velocity of real boundary
at y = ycell\n');
fprintf(fid,' &var  vyby0 =   0.0         /\n');
fprintf(fid,' &var  vyby1 =   0.0         /\n');
fprintf(fid,' &var  t2move =  30.0        /time when the floor starts
to move\n');
fprintf(fid,' &var  vyfloor = 0.0         /velocity of the floor when
moving\n');
fprintf(fid,' &var  draddt =  50.         /rate of increase of particle
radii\n');
fprintf(fid,[' &var  number(1) = ',num2str(20),'        /number of
particles in group 1\n']);
fprintf(fid,' &var  radius(1) = 0.01     /particle radii for group
1\n');
fprintf(fid,' &var  number(2) = 5         /number of particles in group
2\n');
fprintf(fid,' &var  radius(2) = 0.01      /radius of cylindrical
boundry\n');
fprintf(fid,' &var  skn1b = 2.8e+05       /\n');
fprintf(fid,' &var  elastb= 0.92           /\n');
fprintf(fid,' &var  slopeb= 1.0e+05       /\n');
% fprintf(fid,[' &var  vamp =    ',num2str(2*pi*9*i*0.001),'
/velocity amplitude of boundary\n']);
% fprintf(fid,[' &var  frq =     ',num2str(i),'           /frequency of
bump\n']);
fprintf(fid,[' &var  vamp =    ',num2str(i*0.001*2*pi*10),'
/velocity amplitude of boundary\n']);
fprintf(fid,[' &var  frq =     ',num2str(i),'           /frequency of
bump\n']);
fprintf(fid,' &var  tbump =   0.0667      /duration of one bump\n');
```

```
% fprintf(fid,[' &var  nrcg  =
',num2str(round((0.4+(0.4+1/2/10)*10)/(i+1/2/10))-1),'          /number
of bumps to be processed\n']);
fprintf(fid,[' &var  nrcg  =   ',num2str(1),'          /number of bumps
to be processed\n']);
fprintf(fid,' &var  finis =   1.          /end\n');
fprintf(fid,'\n\n\n\n');
% type i3ds
%saveas(fig,['J:\matlab
%environment\RC\tpour2\',num2str(0.02*i),'\each_paricle.jpg'])
save%as(fid,['J:\matlab
environment\ampl\ampl\1par\',num2str(0.001*i),'\i3ds.txt']);
 % saveas(fid, ['M:\matlab
environment\freq\longrelax\1tapfreq\',num2str(i),'\',num2str(i),'.txt']
)
fclose(fid);
%         end
    End
```

APPENDIX B

MATLAB CODE TO GENERATE MASS CENTER TRAJECTORIES

This appendix gives the MATLAB code to generating mass center trajectories.

```
clear;
N = 20;
d = 0.02;
cc = hsv(N);
for i = 0.03

% C = load(['e:\matlab
environment\chaos\SMALL\100taps\dt6\freq\',num2str(i),'\coord.txt']);
% MC = load(['e:\matlab
environment\chaos\SMALL\100taps\dt6\freq\',num2str(i),'\zmasscen']);
C = load(['e:\matlab
environment\chaos\SMALL\100taps\dt6\ampl\testBif1\',num2str(i),'\coord.
txt']);
MC = load(['e:\matlab
environment\chaos\SMALL\100taps\dt6\ampl\testBif1\',num2str(i),'\zmassc
en']);
% C = load(['E:\matlab
environment\chaos\SMALL\ampl\',num2str(i),'\coord.txt']);
% MC = load(['E:\matlab
environment\chaos\SMALL\ampl\',num2str(i),'\zmasscen']);
% MC = load('C:\Users\LUO ZUO\Desktop\temp\zmasscen');

% MC = load(['zmasscen',num2str(i)]);

% % %  j = 1:length(C)/N;


% % %  for k = 1:N
% % %      hold on
% % % % plot(C((j-1)*N+k,2),C((j-1)*N+k,1),'color',cc(k,:))
% % % plot((C((j-1)*N+k,2)+0.05)./0.45,C((j-1)*N+k,1)/d,'k')
% % % plot((MC(:,1)+0.05)./0.45,MC(:,2)/d,'k','LineWidth',5)
% % %
% % % for ii = 1:10
% % % yy(ii) = 0.495;
% % % end
% % %
plot(t(1:10),yy(1:10),'^k','MarkerEdgeColor','k','MarkerFaceColor','k',
'MarkerSize',13);
% % %
% % % xlim([0,11])
% % % set(gca,'FontSize',20);
% % % xlabel('t/T','FontSize', 34,'Rotation',360)
% % % ylabel('$ \frac{y}{d}$','Interpreter','latex','FontSize',
44,'Rotation',360)
% % %  end
```

```
t = zeros(100,1);
 y = zeros(100,1);


%  t(1) = 0.4;
t(1) = 1;
 period = 1/2/10+0.4;
%  period = 1/2/(i*5)+0.4;
 y(1) = (min(MC(:,2))-0.001)/d;


% y(1) = min(C(:,1))-0.001;
for jj = 2:100
% t(jj) = t(jj-1)+1/2/(i*5)+0.4;%pay attention , there is a frequency
parameter will affect the result
% t(jj) = t(jj-1)+1/2/(10)+0.4;%pay attention , there is a frequency
parameter will affect the result
t(jj) = t(jj-1)+1;
y(jj) = y(1);


end
% % %
plot(t,y,'^k','MarkerEdgeColor','k','MarkerFaceColor','k','MarkerSize',
13);
% % % xlim([0,11])
% % % set(gca,'fontsize',30)
% % % xlabel('t/T','FontSize', 40,'Rotation',360)
% % % ylabel('$ \frac{y}{d}$','Interpreter','latex','FontSize',
50,'Rotation',360)

Np = 4;
    for L = 1:Np
% %     j = length(C)/N/Np*(L-1)+1:L*length(C)/N/Np;
% %     for k = 1:N

        subplot(Np,1,L)
% %         plot(C((j-1)*N+k,2),C((j-1)*N+k,1),'color',cc(k,:))
%
% % plot(C((j-1)*N+k,2),C((j-1)*N+k,1)/d);
% % plot(MC(:,1),MC(:,2)/d,'r')
% plot(MC((length(MC)/Np*(L-
1)+1:L*length(MC)/Np),1),MC((length(MC)/Np*(L-
1)+1:L*length(MC)/Np),2)/d,'r');
% %

% plot((MC((round(length(MC)/Np*(L-
1)+1):round(length(MC)/Np*L)),1)+1/2/5/i)./period,MC((round(length(MC)/
Np*(L-1)+1):round(length(MC)/Np*L)),2)/d,'k','LineWidth',2);
plot((MC((round(length(MC)/Np*(L-
1)+1):round(length(MC)/Np*L)),1)+1/2/10)./period,MC((round(length(MC)/N
p*(L-1)+1):round(length(MC)/Np*L)),2)/d,'k','LineWidth',2);

hold on
```

```
plot(t(round(length(t)/Np*(L-
1)+1):round(L*length(t)/Np)),y(round(length(y)/Np*(L-
1)+1):round(L*length(y)/Np)),'^k','MarkerEdgeColor','k','MarkerFaceColo
r','k','MarkerSize',13);
% for iii = (L-1)*25+1:L*25
%     hold on
%     plot(t(iii),MC((round(MC(:,1)*1000)/1000==0.4+(t(iii)-
1)*period)),2)
% end
% plot(t,y/d,'k^')
xlim([(MC(round(length(MC)/Np*(L-
1)+1),1)+1/2/10)./period,(MC(round(length(MC)/Np*L),1)+1/2/10)./period]
)

% % xlim([0,0.4+1/10/2*10+0.4*10])
ylim([(min(MC(:,2))-0.001)/d,(max(MC(:,2))+0.002)/d])
% % ylim([min(C(:,1))/d-0.001/d,max(C(:,1))/d+0.002/d])
xlabel('t/T','FontSize', 34,'Rotation',360)
ylabel('$ \frac{\overline{y}}{d}$','Interpreter','latex','FontSize',
44,'Rotation',360)
    if L ==1
        title(['mass center trajectory at a/d = ',num2str(i/0.02),'
with 100 taps'],'FontSize', 20)
    end

    set(gca,'fontsize',20)
    end

% subplot(Np,1,L)
% plot(MC((length(MC)/5*(L-1)+1:L*length(MC)/5),1),MC((length(MC)/5*(L-
1)+1:L*length(MC)/5),2));
% xlim([MC(round(length(MC)/5*(L-1)+1),1),MC(round(length(MC)/5*L),1)])
% ylim([min(MC(:,2))-0.001,max(MC(:,2))+0.002])
% xlabel('time(secs)')
% ylabel('position(m)');
% end
% title(['A/d = ',num2str(i*0.005/0.02),' '],'FontSize',18)

% title(['100 taps of mass center position of 20-particle column with
amplitude A/d ',num2str(i*0.005/0.02),' particle diameters'])

%  end
% saveas(gca,'asf','jpg')
%     close()
end
```

APPENDIX C

MATLAB CODE TO GENERATE POINCARE MAPS

This appendix gives the MATLAB code to generating Poincare map.

```
clear
f = 10;
tpour = 0.4;
T = tpour+1/f/2;
N = 1000;
NP = 20;
NT = N*T;
tin = 100;

for k = 51%1:10:tin



    disp(k)
for i = 0.0001:0.0001:0.03
% for i = 0.5*0.02:0.0001:0.02
disp(i)

    MC = load(['e:\matlab
environment\chaos\SMALL\100taps\dt6\ampl\testBif1\',num2str(i),'\zmassc
en']);
    t = 0;
for j = 1:100

    t = tpour+T*(j-1)+T/tin*(k-1);
    tn = fix(t*1000);
    y = (t-tn/1000)*(MC(tn+2,2)-MC(tn+1,2))/0.001+MC(tn+1,2);
    hold on
plot(i/0.02,y/0.02,'kx')
end
end
set(gca,'fontsize',18)
xlabel('$ \frac{a}{d} $','interpreter','latex', 'FontSize',
35,'Rotation',360)
    ylabel('$
\frac{\overline{y}}{d}$','Interpreter','latex','FontSize',
35,'Rotation',360)
% title(['$ Poincare Map $',num2str(k),'interpreter','latex',
'FontSize', 22,'Rotation',360])
title(['Poincare Map at t=T+',num2str((k-1)/100),'T'])
xlim([0,1.5])
ylim([9,30])
% print(gca,'-djpeg','-r600',['F:\matlab
environment\chaos\SMALL\100taps\dt6\ampl\testBif1\t',num2str(k-1),])
end
```

REFERENCES

1. A. Levy, and H. Kalman, eds. *Handbook of conveying and handling of particulate solids*. Handbook of Powder Technology, ed. J.C. Williams and T. Allen. **10**. 2001. Elsevier, Amsterdam, Netherlands.
2. M.J. Rhodes, *Introduction to particle technology.* 1998. John Wiley & Sons. 320. Chichester, UK.
3. G. Klinzing, F. Rizk, R.D. Marcus, and L.S. Leung, *Pneumatic conveying of solids - atheoretical and practical approach*. 3rd ed, 2010. Springer, Dordrecht, Netherlands.
4. E.R. Merrow, *Linking R&D to problems experienced in solids processing*, 1984. Rand Corporation. p. 1-21.
5. X.Z. An, C.X. Li, R.Y. Yang, R.P. Zou, and A.B. Yu, *Experimental study of the packing of mono-sized spheres subjected to one-dimensional vibration.* Powder Technology, 2009. **196**(1): p. 50-55.
6. J. Duffy, and R. Mindlin, *Stress-strain relations and vibrations of granular medium.* J. Appl. Mech. Trans. ASME, 1957. **7**: p. 585-593.
7. R. Linemann, J. Runge, M. Sommerfeld, and U. Weifguttel, *Compaction of powders due to vibrations and shocks.* Particle and Particle System Characterization, 2004. **21**(4): p. 261-267.
8. A.W. Roberts, and O.J. Scott, *An investigation into the effects of sinusoidal and random vibrations on the strength and flow properties of bulk solids.* Powder Technology, 1978. **21**(1): p. 45-53.
9. C.R. Wassgren, M.L. Hunt, P.J. Freese, J. Palamra, and C.E. Brennen, *Effects of vertical vibration on hopper flows of granular material.* Physics of Fluids, 2002. **14**(10): p. 3439-3448.
10. F.J. Rademacher and L. ter Borg, *On the theoretical and experimental conveying speed of granular bulk solids on vibratory conveyors.* Forschung im Ingenieurwesen, 1994. **60**(10): p. 261-283.
11. K. Erdész, and A. Szalay, *Experimental study on the vibrational transport of bulk solids.* Powder Technology, 1988. **55**(2): p. 87-96.
12. R.A. Bagnold, *Experiments on a gravity-free dispersion of large solid spheres in a newtonian fluid under shear*. Proc. Roy. Soc. 1954. **A 225**: p. 49, London,UK.
13. R.A. Bagnold, *The physics of blown sand and desert Dunes*. 4th ed 1973. Chapman and Hall. p. 264, London,UK.
14. M.D. Mantle, A.J. Sederman, L.F. Gladden, J.M. Huntley, T.W. Martin, R.D. Wildman, and M.D. Shattuck, *MRI investigations of particle motion within a three-dimensional vibro-fluidized granular bed.* Powder Technology, 2008. **179**(3): p. 164-169.

15. M. Nakagawa, , A. Waggoner, and E. Fukushima, *Non-invasive measurements of fabric of particle packing by MRI*, Introduction to Mechanics of Granular Materials, M. Oda, Editor 1999. A, Balkema, Netherlands.

16. T.-T. Ng, C. Wang, and S. Altobell, *3-D MRI experiment of granular materia*, in *mechanics of deformation and flow of particulate materials*, C.S. Chang, et al., 1997, ASCE, p. 189-198, Evanston, IL.

17. R.A. Waggoner, M. Nakagawa, S.J. Glass, and E. Fukushima, *Particle compaction as observed by MRI*, Spatially Resolved Magnetic ResonanceP. Blumer, B. Blumich, and R. Botta, Editors. 1998, Wiley-VCH, Weinheim, Germany.

18. S.A. Altobelli, A. Caprihan, E. Fukushima, and J.D. Seymour. *Nuclear magnetic resonance studies of granular flows - current status*. Materials Research Society Symposium - Proceedings. 2000, San Francisco, CA.

19. L. Farber, G.I. Tardos, and J.N. Michaels, *Use of x-ray tomography to study the porosity and morphology of granules.* Powder Technology, 2003. **132**(1): p. 57-63.

20. E.J. Garboczi, *Three-dimensional mathematical analysis of particle shape using X-ray tomography and spherical harmonics: Application to aggregates used in concrete.* Cement and Concrete Research, 2002. **32**(10): p. 1621-1638.

21. C. Wu, Y.D. Cheng, Y., F. Wei, and Y. Jin, *A novel x-ray computed tomography method for fast measurement of multiphase flow.* Chemical Engineering Science, 2007. **62**(16): p. 4235-4335.

22. D.J. Parker, A.E. Dikjstra, T.W. Martin, and J.P.K. Seville, *Positron emission particle tracking studies of spherical particle motion in rotating drums.* Chemical Engineering Science, 1997. **52**(13): p. 2011-2022.

23. D.J. Parker, and X. Fan, *Positron emission particle tracking,in Application and labelling techniques.* Particuology, 2008. **6**(1): p. 16-23.

24. S. Linz, and A. Dohle, *Minimal relaxation law for compaction of tapped granular matter.* Phys. Rev. E, 1999. **60**(5): p. 5737-5741.

25. A.D. Rosato, , D. Blackmore, K. Urban, L. Zuo, and X. Tricoche, *Dynamical systems model and discrete element simulations of a tapped granular column*, Powders & Grains *2013 (under review)*, American Institute of Physics, Sydney, AU.

26. P. Evesque, *Modelling the micro-macro passage in the quasi-statics regime of granular matter*. Powders & Grains *2001*. Balkema, Netherlands.

27. S. Kitsunezaki, *Quasi-static deformation of a granular system with a regular arrangement of particles.* Granular Matter, 2004. **6**(4): p. 221-228.

28. C. Thornton, *Quasi-static simulations of compact polydisperse particle systems.* Particuology, 2010. **8**(2): p. 119-126.

29. C. Thornton, and S.J. Antony, *Quasi-static deformation of particulate media.* Phil. Trans. Roy. Soc. A, 1998. **356**(2763-2782), London,UK.

30. C. Campbell, *Rapid granular flows.* Ann. Rev. Fluid Mech., 1990. **22**: p. 57-92.

31. C. Chou, *Kinetic theories of rapid granular flows of highly inelastic particles*. *ASME-ASCE-SES* Joint Summer Meeting. 1997.

32. J.T. Jenkins, *Rapid flows of granular materials*, in *non-classical continuum mechanics*, R. Knops and A. Lacey, Editors. 1987, Cambrige University Press, p. 213-225. Cambridge, UK.

33. M.Y. Louge, *Computer simulations of rapid granular flows of spheres interacting with a flat, frictional boundary.* Phys. Fluids 1994. **6**(7): p. 2253-2269.

34. S.B. Savage, R.M. Nedderman, U. Tuzun, and G.T. Houlsby, *Flow of granular materials - 3. Rapid shear flows* Chem. Eng. Sci., 1983. **38**(2): p. 189-195.

35. R.D. Wildman, T.W. Martin, J.M. Huntley, J.T. Jenkins, H. Viswanathan, X. Fen, and D.J. Parker, *Experimental investigation and kinetic-theory-based model of a rapid granular shear flow.* J. Fluid. Mech., 2008. **602**: p. 63-79.

36. T. Akiyama, Y. Miyamoto, N. Yamanaka, and J.Q. Zhang, *Densification of powders by means of air, vibratory and mechanical compactions.* Powder Technology, 1986. **46**(2-3): p. 173-180.

37. O. Dybenko, A.D. Rosato, and D. Horntrop, *Three-dimensional Monte Carlo simulations of density relaxation.* KONA Powder and Particle, 2007. **25**: p. 133-144.

38. J.B. Knight, C.G. Fandrich, C.N. Lau, H.M. Jaeger, and S.R. Nagel, *Density relaxation in a vibrated granular material.* Phys. Rev. E, 1995. **51**: p. 3957-3963.

39. P. Ribière, P. Richard, P. Philippe, D. Bideau, and R. Delannay, *On the existence of stationary states during granular compaction.* European Physical Journal E, 2007. **22**(3): p. 249-253.

40. P. Richard, P. Philippe, F. Barbe, S. Bourle?s, X. Thibault, and D. Bideau, *Analysis by x-ray microtomography of a granular packing undergoing compaction.* Physical Review E - Statistical, Nonlinear, and Soft Matter Physics, 2003. **68**(2).

41. P. Richard, P. Philippe, F. Barbe, S. Bourlès, X. Thibault, and D. Bideau, *Analysis by x-ray microtomography of a granular packing undergoing compaction.* Physical Review E - Statistical, Nonlinear, and Soft Matter Physics, 2003. **68**(2): p. 020301/1-020301/4.

42. A.D. Rosato, O. Dybenko, V. Ratnaswamy, D. Horntrop, and L. Kondic, *Microstructure evolution in density relaxation by tapping.* Phys. Rev. E, 2010. **81**(061301).

43. A.D. Rosato, V. Ratnaswamy, D.J. Horntrop, O. Dybenko, and L. Kondic. *Temporal dynamics in density relaxation*. 2010. Reggio Calabria, Italy.

44. N. Zhang, and A.D. Rosato, *Experiments and simulations on vibration induced densification of bulk solids.*KONA Powder and Particle, 2006. **24**: p. 93-103.

45. M.W. Richman, and R.E. Martin. *Unconfined granular materials thermalized by fluctuating horizontal surfaces*. Proceedings of the 9th Conference on Engineering Mechanics. 1992. ASCE.

46. M. Faraday, *On a peculiar class of acoustical figures and on certain forms assumed by groups of particles upon vibrating elastic surfaces.* Philos. Trans. R. Soc. 1831. **52**: p. 299, London,UK.

47. G. Metcalfe, T. Shinbrot, J.J. McCarthy, and J.M. Ottino, *Mising patterns for surface dominated granular flows.* Phys. Fluids A, 1995. **7**: p. cover article.

48. S.L. Conway, D.J. Goldfarb, T. Shinbrot, and B.J. Glasser, *Free surface instabilities in rapid granular chute flows.* Phys. Rev. Lett., 2003. **90**: p. 074301.

49. S. Luding, *Clustering insabilities, arching, and anomalous interacion probabiliies as examples for cooperative phenomena in dry granular media.* T.A.S.K. Quarterly (Scientific Bulletin of Academic Computer Centre of the Technical University of Gdansk), 1998. **2**(3): p. 417-443.

50. S. Luding, *Surface waves and pattern formation in vibrated granular media,*Powders and Grains 1997, R. Behringer and J.T. Jenkins, Editors. 1997, A. Balkema,Netherlands.

51. S.S. Hsiau, M.H. Wu, and C.H. Chen, *Arching phenomena in a vibrated granular bed.* Powder Technology, 1998. **99**(2): p. 185-193.

52. A. Saez, F. Vivanco, and F. Melo, *Size segregation, convection, and arching effect.* Physical Review E - Statistical, Nonlinear, and Soft Matter Physics, 2005. **72**(2): p. 1-7.

53. T. Akiyama, K. Shinmura, S. Murakawa, and K.M. Aoki, *A surface instability of granules under vibration in partitioned containers.* Granular Matter, 2001. **3**(3): p. 177-183.

54. L.A. Pugnaloni, M.G. Valluzzi, and L.G. Valluzzi, *Arching in tapped deposits of hard disks.* Physical Review E - Statistical, Nonlinear, and Soft Matter Physics, 2006. **73**(5).

55. N. Mujica, and F. Melo, *Experimental study of solid-liquid-type transitions in vibrated granular layers and the relation with surface waves.* Physical Review E - Statistical, Nonlinear, and Soft Matter Physics, 2001. **63**(1): p. 1-14.

56. L. Bonneau, B. Andreotti, and E. Clement, *Evidence of Rayleigh-Hertz surface waves and shear stiffness anomaly in granular media.* Physical Review Letters, 2008. **101**(11).

57. E. Clement, L. Bonneau, and B. Andreotti. *Surface wave acoustics of granular packing under gravity*. 2009, Golden, CO.

58. O.R. Walton, and R.L. Braun, *Viscosity and temperature calculations for assemblies of inelastic, frictional disks.* J. Rheol., 1986. **30**(5): p. 949-980.

59. O.R. Walton, *Numerical simulation of inclined chute flows of monodisperse, inelastic, frictional spheres.* Mechanics of Materials, 1993. **16**: p. 239-247.

60. V.F. Nesterenko, *Propagation of nonlinear compression pulses in granular media.* J. Appl. Mech. Tech. Phys., 1984. **24**: p. 733-743.

61. E. Falcon, C. Laroche, S. Fauve, and C. Coste, *Collision of a 1-D column of beads with a wall.* Eur. Phys. J. B, 1998. **5**(1): p. 111-131.

62. S. Job, F. Melo, A. Sokolow, and S. Sen, *How hertzian solitary waves interact with boundaries in a 1D granular medium.* Phys. Rev. Lett., 2005. **94**(17): p. 1-4.

63. S. Job, F. Melo, A. Sokolow, and S. Sen, *Solitary wave trains in granular chains: experiments, theory and simulations.* Granular Matter, 2007. **10**(1): p. 13-20.

64. S. Job, F. Santibanez, F. Tapia, and F. Melo, *Wave localization in strongly nonlinear Hertzian chains with mass defect.* Phys. Rev. E, 2009. **80**(2).

65. F. Santibanez, R. Munoz, A. Caussarieu, S. Job, and F. Melo, *Experimental evidence of solitary wave interaction in Hertzian chains.* Physical Review E - Statistical, Nonlinear, and Soft Matter Physics, 2011. **84**(2).

66. D. Blackmore, R. Samulyak, and A. Rosato, *New mathematical model for particle flow dynamics.* J. Nonlin. Math. Phys, 1999. **6**: p. 198-221.

67. D. Blackmore, K. Urban, and A. Rosato, *Integrability analysis of regular and fractional BSR fields.* Condensed Matter. Phys., 2010. **13**(43403): p. 1-7.

68. B. Bernu, and R. Mazighi, *One-dimensional bounce of inelastically colliding marbles on a wall.* Journal of Physics A, Mathematical and General 1990. **23**(24): p. 5745.

69. E. Clement, S. Luding, A. Blumen, J. Rajchenbach, and J. Duran, *Fluidization, condensation and clusterization of a vibrating column of beads.* Int. J. Mod. Phys. B, 1993. **7**: p. 1807.

70. S. Luding, E. Clement, A. Blumen, J. Rajchenbach, and J. Duran, *Studies of columns of beads under external vibrations.* Physical Review E, 1994. **49**(2): p. 1634-1646.

71. A. Goldshtein, A. Alexeev, and M. Shapiro, *Hydrodynamics of resonance oscillations of columns of inelastic particles.* Physical Review E., 1999. **59**(6): p. 6967-6976.

72. A. Goldshtein, A. Alexeev, and M. Shapiro, *Resonance oscillations in granular gases.* Lecture Notes in Physics, 2001. **564**: p. 266-277.

73. A. Alexeev, A. Goldshtein, and M. Shapiro, *The liquid and solid states of highly dissipative vibrated granular columns: One-dimensional computer simulations.* Powder Technology, 2002. **123**(1): p. 83-104.

74. S. Sen, J. Hong, J. Bang, E. Avalos, and R. Doney, *Solitary waves in the granular chain.* Physics Reports, 2008. **462**(2): p. 21-66.

75. S. Sen, and M. Manciu, *Discrete hertzian chains and solitons.* Physica A, Statistical Mechanics and its Applications, 1999. **268**(3-4): p. 644-649.

76. S. Sen, and M. Manciu, *Solitary wave dynamics in generalized Hertz chains: An improved solution of the equation of motion.* Physical Review E - Statistical, Nonlinear, and Soft Matter Physics, 2001. **64**(5).

77. S. Sen, and T.R.K. Mohan, *Dynamics of metastable breathers in nonlinear chains in acoustic vacuum.* Physical Review E - Statistical, Nonlinear, and Soft Matter Physics, 2009. **79**(3).

78. C. Coste, C. Falcon, and S. Fauve, *Solitary waves in a chain of beads under Hertz contact.* Phys. Rev. E, 1997. **56**(5): p. 6104-6117.

79. C.A. Arancibia-Bulnes, and J.C. Ruiz-Suárez, *Broad solitons in homogeneous Hertzian granular chains.* Physica D, Nonlinear Phenomena, 2002. **168-169**: p. 159-164.

80. N. Boechler and C. Daraio. *An experimental investigation of acoustic band gaps and localization in granular elastic chains*. Proceedings of the 22nd Biennial Conference on Mechanical Vibration and Noise. 2009, San Diego, CA.

81. E. Hascoet, and H.J. Herrmann, *Shocks in non-loaded bead chains with impurities.* European Physical Journal B, 2000. **14**(1): p. 183-190.

82. E.B. Herbold, and V.F. Nesterenko. *The role of dissipation on wave shape and attenuation in granular chains*. 2010. Santiago, Chile.

83. G. James, *Periodic travelling waves and compactons in granular chains.* J. Nonlin. Sci., 2012. **22**(5): p. 813-848.

84. D. Khatri, D. Ngo, and C. Daraio, *Highly nonlinear solitary waves in chains of cylindrical particles.* Granul. Matter, 2012. **14**(1): p. 63-69.

85. T.R. Krishna Mohan, and S. Sen, *The quasi-equilibrium phase of nonlinear chains.* Pramana - Journal of Physics, 2005. **64**(3 SPEC. ISS.): p. 423-431.

86. M. Manjunath, A.P. Awasthi, and P.H. Geubelle, *Wave propagation in random granular chains.* Physical Review E - Statistical, Nonlinear, and Soft Matter Physics, 2012. **85**(3).

87. A. Molinari, and C. Daraio, *Stationary shocks in periodic highly nonlinear granular chains.* Phys. Rev. E, 2009. **80**(5).

88. N.S. Nguyen, and B. Brogliato, *Shock dynamics in granular chains: Numerical simulations and comparison with experimental tests.* Granular Matter, 2012. **14**(3): p. 341-362.

89. V.F. Nesterenko, and A.N. Lazaridi, *Observation of a new type of solitary waves in a one-dimensional granular medium.* J. Appl. Mech. Technol. Phys., 1985. **26**: p. 405-408.

90. V.F. Nesterenko, *Solitary waves in discrete media with anomalous compressibility and similar to "sonic vacuum".* Journal de Physique IV, 1994. **04**(C8): p. C8-729 - C8-734.

91. J. Hong, and A. Xu, *Effects of gravity and nonlinearity on the waves in the granular chain.* Physical Review E - Statistical, Nonlinear, and Soft Matter Physics, 2001. **63**(6).

92. E. Ávalos, J.M.M. Pfannes, T.R. Krishna Mohan, and S. Sen, *A numerical study of the dynamics of the surface grain in a granular chain and the role of gravity.* Physica D, Nonlinear Phenomena, 2007. **225**(2): p. 211-218.

93. E. Avalos, and S. Sen, *How solitary waves collide in discrete granular alignments.* Physical Review E - Statistical, Nonlinear, and Soft Matter Physics, 2009. **79**(4).

94. C. Daraio, V.F. Nesterenko, E.B. Herbold, and S. Jin, *Strongly nonlinear waves in a chain of Teflon beads.* Phys. Rev. E, 2005. **72**(1): p. 1-9.

95. M. De Billy, *Experimental study of sound propagation in a chain of spherical beads.* Journal of the Acoustical Society of America, 2000. **108**(4): p. 1486-1495.

96. J. Hong, *Slow dynamical behaviors of the propagating signal in granular chain under gravity.* Physica A, Statistical Mechanics and its Applications, 2002. **315**(1-2): p. 187-193.

97. J. Hong, J.Y. Ji, and H. Kim, *Power laws in nonlinear granular chain under gravity.* Physical Review Letters, 1999. **82**(15): p. 3058-3061.

98. K.R. Jayaprakash, Y. Starosvetsky, A.F. Vakakis, M. Peeters, and G. Kerschen, *Nonlinear normal modes and band zones in granular chains with no pre-compression.* Nonlinear Dynamics, 2011. **63**(3): p. 359-385.

99. J.Y. Ji, and J. Hong, *Existence criterion of solitary waves in a chain of grains.* Physics Letters, Section A: General, Atomic and Solid State Physics, 1999. **260**(1-2): p. 60-61.

100. S. Job, F. Santibanez, F. Tapia, and F. Melo, *Nonlinear waves in dry and wet Hertzian granular chains.* Ultrasonics, 2008. **48**(6-7): p. 506-514.

101. P.N. Panagopoulos, A.F. Vakakis, and S. Tsakirtzis, *Transient resonant interactions of finite linear chains with essentially nonlinear end attachments leading to passive energy pumping.* International Journal of Solids and Structures, 2004. **41**(22-23): p. 6505-6528.

102. N. Boechler, J. Yang, G. Theocharis, P.G. Kevrekidis, and C. Daraio, *Tunable vibrational band gaps in one-dimensional diatomic granular crystals with three-particle unit cells.* Journal of Applied Physics, 2011. **109**(7).

103. A.C. Hladky-Hennion, and M. de Billy, *Experimental validation of band gaps and localization in a one-dimensional diatomic phononic crystal.* J. Acoust. Soc. Am., 2007. **122**(5): p. 2594-2600.

104. K.R. Jayaprakash, A.F. Vakakis, and Y. Starosvetsky, *Strongly nonlinear traveling waves in granular dimer chains.* Mechanical Systems and Signal Processing, 2012.

105. F. Fraternali, M.A. Porter, and C. Daraio, *Optimal design of composite granular protectors.* Mechanics of Advanced Materials and Structures, 2010. **17**(1): p. 1-19.

106. U. Harbola, A. Rosas, A.H. Romero, M. Esposito, and K. Lindenberg, *Pulse propagation in decorated granular chains: An analytical approach.* Phys. Rev. E, 2009. **80**(5).

107. U. Harbola, A. Rosas, A.H. Romero, and K. Lindenberg, *Pulse propagation in randomly decorated chains.* Phys Rev. E 2010. **82**(1).

108. F. Melo, S. Job, F. Santibanez, and F. Tapia, *Experimental evidence of shock mitigation in a Hertzian tapered chain.* Physical Review E - Statistical, Nonlinear, and Soft Matter Physics, 2006. **73**(4).

109. R.L. Doney, and S. Sen, *Impulse absorption by tapered horizontal alignments of elastic spheres.* Phys. Rev. E, 2005. **72**(4): p. 1-11.

110. R.S. Sinkovits, and S. Sen, *Nonlinear dynamics in granular columns.* Physical Review Letters, 1995. **74**(14): p. 2686-2689.

111. S. Sen, and R.S. Sinkovits, *Sound propagation in impure granular columns.* Physical Review E - Statistical Physics, Plasmas, Fluids, and Related Interdisciplinary Topics, 1996. **54**(6): p. 6857-6865.

112. M. Manciu, S. Sen, and A.J. Hurd, *Crossing of identical solitary waves in a chain of elastic beads.* Physical Review E - Statistical, Nonlinear, and Soft Matter Physics, 2001. **63**(1 II): p. 1-6.

113. A. Rosas, A.H. Romero, V.F. Nesterenko, and K. Lindenberg, *Observation of two-wave structures in strongly nonlinear dissipative granular chains.* Phys. Rev. Lett., 2007. **98**: p. 164301.

114. C. Liu, Z. Zhao, and B. Brogliato, *Energy dissipation and dispersion effects in a granular media.* Phys. Rev. E, 2008. **78**: p. 031307.

115. C. Liu, Z. Z., and B. B., *Frictionless multiple impacts in multibody systems: Part I. Theoretical framework.* Proc. R. Soc. A 2008. **464(2100),** p. 3193–3211.

116. C. Liu, Z. Z., and B. B., *Frictionless multiple impacts in multibody systems: Part II. Numerical algorithm and simulation results.* Proc. R. Soc. A, 2009. **465(2101)**, p. 1-23.

117. H. Zhang, and B. Brogliato, *The planar rocking block: analysis of kinematic restitution laws, and a new rigid-body impact model with friction*, 2011.

118. Z. Zhao, C. Liu, and B. Brogliato, *Planar dynamics of a rigid body system with frictional impacts. II. Qualitative analysis and numerical simulations.* Proc. R. Soc. A, 2009. **465(2107)**: p. 2267–2292.

119. P.A. Cundall, *Rational design of tunnel supports: A computer model for rock-mass behavior using interactive graphics for input and output of geometrical data*, U. S. Army Corp. of Engineers. 1974, p. 2074.

120. B.J. Alder, and T.E. Wainwright. *Statistical mechanical theory of transport properties*. Proceedings of the International Union of Pure and Applied Physics, 1956. Brussels, Belgium.

121. B.J. Alder, and T.E.WainWright, *Studies in molecular dynamics. II. Behavior of a small number of elastic spheres.* The Journal of Chemical Physics, 1960. **33**(5): p. 1439-1451.

122. O.R. Walton, *Numerical simulation of inelastic, frictional particle-particle interactions*, in *Particulate Two-Phase Flow*, M.C. Roco, Editor 1992, Butterworths, p. 884-911, Boston, MA.

123. O.R. Walton, and R.L. Braun, *Stress calculations for assemblies of inelastic spheres in uniform shear.* Acta Mech., 1986. **63**(1-4): p. 73-86.

124. S.F. Foerster, M.Y. Louge, H. Chang, and K. Allia, *Measurements of the collision properties of small spheres.* Phys. FLuids 1994. **6**(3): p. 1108-1115.

125. L. Labous, A.D. Rosato, and R. Dave, *Measurement of sphere collision Properties.* Phys. Rev. E., 1997. **56**: p. 5717.

126. Y. Lan, PhD Dissertation, *Particle dynamics modeling of vibrating granular beds*, 1994, New Jersey Institute of Technology, Newark,NJ.

127. W. Goldsmith, *Impact: the theory and physical behavior of colliding solids* 1960, Edward Arnold, London,UK.

128. M.A. Cuendet, and W.F. van Gunsteren, *On the calculation of velocity-dependent properties in molecular dynamics simulations using the leapfrog integration algorithm.* The Journal of Chemical Physics, 2007. **127**(18).

129. M. Sweetman, master thesis, *Addition of a chain-cell search method and a Van Der Waals force model to a particle dynamics code*, 2003, New Jersey Institute of Technology: Newark, NJ.

130. H.J. Kim, PhD Dissertation, *Particle dynamics modeling of boundary effects in granular couette flow*, 1992, New Jersey Institute of Technology: Newark, NJ.

131. D. Blackmore, A. Rosato, X. Tricoche, K. Urban, and V. Ratnaswamy, *Tapping dynamics for a column of particles and beyond.* Journal of Mechanics of Materials and Structures, 2011. **6**(1-4): p. 71-86.

132. D. Blackmore, A. Rosato, X. Tricoche, K. Urban, and L. Zuo, D. *Analysis, simulation and visualization of 1D tapping via reduced dynamical systems models.* Physica D, 2013, under revision.